

CHEMICALLY MODIFIED ELECTRODES: A SUPRAMOLECULAR  
ASSEMBLY APPROACH

Except where reference is made to the work of others, the work described in this dissertation is my own or was done in collaboration with my advisory committee. This dissertation does not include proprietary, restricted or classified information.

---

Junhua Xin

Certificate of Approval

---

Vince Cammarata  
Associate Professor  
Chemistry and Biochemistry

---

Curtis Shannon, Chair  
Professor  
Chemistry and Biochemistry

---

Wei Zhan  
Assistant Professor  
Chemistry and Biochemistry

---

Thomas Albrecht-Schmitt  
Professor  
Chemistry and Biochemistry

---

George T. Flowers  
Dean  
Graduate Schools

CHEMICALLY MODIFIED ELECTRODES: A SUPRAMOLECULAR  
ASSEMBLY APPROACH

Junhua Xin

A Dissertation

Submitted to

the Graduate Faculty of

Auburn University

in Partial Fulfillment of the

Requirements for the

Degree of

Doctor of Philosophy

Auburn, Alabama  
December 19, 2008

CHEMICALLY MODIFIED ELECTRODES: A SUPRAMOLECULAR  
ASSEMBLY APPROACH

Junhua Xin

Permission is granted to Auburn University to make copies of this dissertation at its discretion, upon request of individuals or institutions and at their expense. The author reserves all publication rights.

---

Signature of Author

---

Date of Graduation

## VITA

Junhua Xin, daughter of Zuoqiang Xin and Jixiang Yu was born on April 24, 1977 in Benxi, Liaoning, People's Republic of China. She is the eldest in the family with one younger sister, Junhong Xin. She obtained her high school diploma from Benxi NO. 1 high school, then she studied in Liaoning Normal University (LNNU) and completed her Bachelor of Science degree in Chemistry in July 2000 and Master of Science degree in Physical Chemistry in July 2003. Starting from Jan. 2003, she worked as an instructor in Missouri State University branch campus at LNNU for a year. In Jan. 2004, she entered the Department of Chemistry and Biochemistry at Auburn University to pursue a Doctoral degree in Analytical Chemistry. She married Dr. Zengqiang Deng on October 18, 2003.

CHEMICALLY MODIFIED ELECTRODES: A SUPRAMOLECULAR  
ASSEMBLY APPROACH

Junhua Xin

Doctor of Philosophy, December 19, 2008  
(B.S. Liaoning Normal University, 2000)

188 Typed Pages

Directed by Curtis Shannon

The main objective of this dissertation is to design and study new superamolecular assemblies for membrane separation, sensing and catalysis applications. Three types of supramolecular assemblies will be addressed including ruthenium directed molecular assembly, polythioxometalate encapsulated hydroquinone assembly and layer by layer assembly of gold nanoparticle and cobalt monosubstituted wells-dowson compound. The synthesis, characterization and related applications of these systems will be discussed in detail.

Chapter 1 presents the comprehensive literature review on Supramolecular Assembly. Detailed information will be provided in terms of the fundamentals and recent advances in transition metal-directed tetrameric assembly and polyoxometalate based

superamolecular assemblies. The latter is further addressed as wheel/sphere shaped polyoxometalate assembly and layer by layer (LbL) assembly.

Chapter 2 provides a detailed discussion of Ruthenium based metallocycles linked by bipyridine spacers (pyrazine(PZ), 4,4'-bipyridine(BP), 4,4'-Azodipyridine(AZP), 4,4'-(1,3-butadiyne-1,4-diyl)bis-Pyridine(DPB) and 3,6-di-4-pyridinyl-1,2,4,5-Tetrazine(dipyTz). These metallocycles will be fully characterized using UV-Vis, Raman, NMR and electrochemistry. The equilibrium of square species and triangle species for DPB and dipyTz linked metallocycles will be studied using  $^1\text{H}$  NMR at different concentrations. Diffusion NMR and potential step experiment will also be employed to study the size of these metallocycles based on the measured diffusion coefficients. The use of BP tetramer as building unit for extended three dimensional frameworks will also be discussed.

Chapter 3 presents the application of ruthenium molecular squares for membrane separation. Permeation tests will be discussed in both solution phase and gas phase. For solution phase permeation test, glassy carbon electrode covered with molecular square film will be examined in redox probes ( $\text{Ru}(\text{NH}_3)_6^{3+}$ ,  $\text{Co}(\text{bpy})_3^{3+}$ ) containing solution. Based on the amount of each probe that can permeate through the membrane, the separation capability of the film will be evaluated. For gas phase permeation test, the assessment will be performed with a home built glass cell connected to Gas Chromatography analyzer. The factors that constitute for the separation such as size and affinity effect will also be discussed.

Chapter 4 presents the study of host-guest chemistry of polythiooxometalate encapsulated hydroquinone complex. The complex is designed in the way that weak

interactions are expected between the POM backbone and encapsulated hydroquinone. Such a system can be used for sensor development. The complex will be fully characterized using single crystal x-ray diffraction, elemental analysis and Raman spectroscopy. The host guest interactions in solution will be studied by NMR and electrochemistry.

Chapter 5 provides a detailed study of LbL assembly formed on glassy carbon substrate using PDDA stabilized Au nanoparticles and polyoxometalates (Cobalt monosubstituted Wells Dawson) for oxygen reduction catalysis. The LbL assembly will be characterized using UV-Vis and electrochemistry. The influence of film thickness (number of layers) and polyoxometalate (transition metal substitution) on the kinetics of the ORR will be discussed. Also the specific activity towards oxygen reduction of this system will be calculated. The value will be compared to the published values to address the catalysis efficiency of the system.

Chapter 6 is a brief summary of this research.

## ACKNOWLEDGEMENTS

I wish to thank my advisor, Dr. Curtis Shannon, for his constant guidance, invaluable inspiration and endless encouragement during the entire course of this research. I also wish to thank the committee members Dr. Cammarata, Dr. Albrecht-Schmitt, and Dr. Zhan and my outside reader Dr. Fergus for their numerous insightful suggestions during the preparation of this manuscript.

I would like to acknowledge all the members that I work with in Dr Shannon's group, Ugur Tamer, Lunsheng Zhang, Anand Sankarraj, Joseph Wu, Chaokang Gu, Sridevi Ramakrishnan, Rajakumari Ramaswamy, Weiping Li, Hongxia Zhang, Tanyu Wang, and Yajiao Yu for their supports and collaborations. I would also like to thank all the friends and colleagues at Auburn for the supports and encouragement, both at work and out of it.

I would like to thank my parents, sister for their support and encouragement during my graduate studies. Last but not least, I want to thank my husband, Zengqiang Deng for his constant encouragement, love and support throughout years together.



Style manual or journal used: Journal of the American Chemical Society

Computer software used: Microsoft Word 2003, Microsoft PowerPoint 2003, Microsoft Excel 2003, Origin Pro 7.5 and Endnote 9

## TABLE OF CONTENTS

LIST OF TABLES .....	xv
LIST OF SCHEMES .....	xvi
LIST OF FIGURES .....	xvii
1. SUPRAMOLECULAR ASSEMBLIES: BASIC CONCEPTS AND RECENT ADVANCES.....	1
1.1 Introduction.....	1
1.2 Transition metal directed supramolecular assembly.....	3
1.2.1 Introduction.....	3
1.2.2 Rhenium (I) based molecular squares.....	4
1.2.3 Pd (II) and Pt (II) based molecular squares .....	6
1.2.4 Chiral molecular squares.....	10
1.2.5 Porphyrin based molecular squares .....	11
1.3 Polyoxometalate based supramolecular assembly .....	14
1.3.1 Introduction of polyoxometalate.....	14
1.3.1.1 Polyoxometalate structure.....	15
1.3.1.2 Common structures of Iso- and Heteropolyoxometalates.....	16
1.3.1.3 Features of polyoxometalate.....	17
1.3.2 Polyoxometalate encapsulation assembly.....	19
1.3.2.1 Introduction.....	19

1.3.2.2 $K_{28}Li_5H_7P_8W_{48}O_{184}$ encapsulation complex .....	20
1.3.2.3 Mo based “giant-wheel/sphere” clusters and its encapsulation complex .....	22
1.3.2.4 Polythiooxometalate and its encapsulation complex .....	27
1.3.3 Polyoxometalate based LbL assembly .....	29
1.3.3.1 Introduction of LbL assembly.....	30
1.3.3.2 LbL assembly with Keggin type polyoxometalate .....	32
1.3.3.3 LbL assembly with Wells Dawson type polyoxometalate.....	34
1.3.3.4 LbL assembly with wheel/sphere shaped polyoxometalate.....	35
1.3.3.5 LbL assembly with Preyssler type polyoxometalate .....	36
1.3.3.6 LbL assembly using POM stabilized nanostructures.....	37
1.3.3.7 LbL assembly with other type polyoxometalate.....	38
1.4 Conclusions.....	39
1.5 References.....	39
<b>2. SYNTHESIS AND CHARACTERIZATION OF RUTHENIUM (II) MOLECULAR SQUARES, AND TRIANGLE-SQUARE EQUILIBRIUM STUDIES .....</b>	<b>45</b>
2.1 Introduction.....	45
2.2 Experimental .....	48
2.2.1 Chemicals and reagents.....	48
2.2.2 Apparatus .....	48
2.2.3 Synthesis procedures.....	50
2.3 Results and discussion .....	51
2.3.1 Synthesis .....	51

2.3.2 UV-Vis spectra.....	51
2.3.3 Raman spectra.....	55
2.3.4 NMR spectra.....	60
2.3.5 Electrochemistry.....	69
2.3.6 Other characterization techniques.....	73
2.3.7 Extended framework.....	74
2.4 Conclusions.....	76
2.5 References.....	77
3. PERMEATION STUDY OF RUTHENIUM (II) MOLECULAR SQUARE BASED MEMBRANES IN SOLUTION PHASE AND GAS PHASE.....	80
3.1 Introduction.....	80
3.2 Experimental.....	81
3.2.1 Materials.....	81
3.2.2 Membrane preparation.....	81
3.2.3 Measurements.....	82
3.3 Results and discussion.....	83
3.3.1 Membrane characterization.....	83
3.3.2 Solution phase sieving.....	85
3.3.3 Gas phase separation.....	90
3.4 Conclusion.....	92
3.5 References.....	92
4. POLYTHIOOXOMETALATE-ENCAPSULATED HYDROQUINONES: SYNTHESIS, CHARACTERIZATION AND ELECTROCHEMISTRY.....	94

4.1 Introduction.....	94
4.2 Experimental.....	103
4.2.1 Chemicals.....	103
4.2.2 Synthesis.....	103
4.2.3 Instrumentation.....	104
4.3 Results and discussion.....	108
4.3.1 Synthesis.....	108
4.3.2 Structure.....	109
4.3.3 Raman spectra.....	111
4.3.4 NMR spectra.....	112
4.3.5 Electrochemistry study.....	115
4.3.6 Extended structure.....	122
4.4 Future work.....	122
4.5 Conclusions.....	123
4.6 References.....	123
<b>5. LBL ASSEMBLY OF GOLD NANOPARTICLE AND POLYOXOMETALATES</b>	
<b>FOR OXYGEN REDUCTION.....</b>	<b>128</b>
5.1 Introduction.....	128
5.2 Experimental.....	131
5.2.1 Chemicals and Reagents.....	131
5.2.2 Apparatus.....	132
5.2.3 Procedures.....	132
5.3 Results and discussion.....	134

5.3.1 Gold nanoparticle preparation and characterization .....	134
5.3.2 Characterization of LbL by cyclic voltammetry .....	137
5.3.3 Characterization of LbL by UV-Vis absorption .....	140
5.3.4 Quantification of gold nanoparticles.....	143
5.3.5 Electroactive probe measurement .....	146
5.3.6 Oxygen reduction of GC modified LbL assembly.....	150
5.4 Conclusion .....	160
5.5 References.....	160
6. SUMMARY AND CONCLUSIONS .....	166

## LIST OF TABLES

Table 1.1 Triangle and square distribution with different Metal corner and bridging Ligand.....	9
Table 2.1 UV-Vis absorption of $\{[\text{RuCl}_2(\text{dppb})](\mu\text{-N-N})\}_n$ .....	52
Table 2.2 Raman assignment of bridging ligands and their Complex .....	57
Table 2.3 $^1\text{H}$ NMR data in $\text{CDCl}_3$ .....	63
Table 2.4 Molecular diffusion coefficients measure from PFG-NMR .....	68
Table 2.5 Summary of half wave potential and peak separation $\{[\text{RuCl}_2(\text{dppb})](\mu\text{-N-N})\}_n$ , $\mu\text{-N-N}=\text{AZP}$ , $\text{DPB}$ and $\text{dipyTz}$ .....	70
Table 2.6 Diffusion coefficient measured from potential step experiment .....	72
Table 3.1 Summary of Sieving results of $\{[\text{RuCl}_2(\text{dppb})](\mu\text{-N-N})\}_4$ based membrane ( $\mu\text{-N-N} = \text{pz}$ , $\text{bipy}$ and $\text{AZP}$ ).....	90
Table 3.2 Separation of benzene and toluene .....	91
Table 3.3 Separation of benzene and cyclohexane .....	91
Table 3.4 Comparison of permeation data of $\{[\text{RuCl}_2(\text{dppb})](\mu\text{-pz})\}_4$ based membrane with previous study .....	92
Table 4.1 Crystallographic data and structure refinement details .....	106
Table 4.2 Selected bond distances ( $\text{\AA}$ ) and angles (deg) .....	107
Table 5.1 Summary of Pom surface coverage .....	140
Table 5.2 Diffusion coefficients of $\text{Ru}(\text{NH}_3)_6\text{Cl}_3$ at bare GC and LbL modified GC .....	148
Table 5.3 Summary of kinetic currents ( $i_k$ ) and specific activities (SAs) for bulk Au and $(\text{PDDA-AuNP/CoDawson})_{13}$ /GC at $-0.1\text{V}$ .....	159

## LIST OF SCHEMES

Scheme 1.1 Synthetic strategies of molecular square.....	4
Scheme 1.2 Illustration of the formation process of Polyoxometalates and polythioxometalate.....	29
Scheme 2.1 The pulse diagram of ledbpgp2s1d .....	50
Scheme 2.2 Molecular structure of cyano-bridged compound .....	76
Scheme 3.1 Gas separation setup .....	83
Scheme 4.1 Reaction pathways for the oxidation of hydroquinone .....	98
Scheme 4.2 Redox dependant receptor-substrate binding equilibrium scheme .....	101
Scheme 4.3 P-Q binding equilibrium scheme.....	119
Scheme 5.1 Reaction scheme for oxygen electroreduction according to Wroblowa .....	154



## LIST OF FIGURES

Fig 1.1 Rhenium based molecular squares .....	6
Fig 1.2 Pt (II) or Pd (II) based molecular squares.....	8
Fig 1.3 Structure of some chiral molecular squares.....	11
Fig 1.4 Structure of porphyrin molecular squares reported by Drain and Lehn .....	13
Fig 1.5 Molecular Structures of (L) <sub>4</sub> , L= L <sub>1</sub> and L <sub>2</sub> respectively .....	14
Fig 1.6 Common Structures of Iso- and Heteropolyoxometalates 9a) [M <sub>6</sub> O <sub>19</sub> ] <sup>n-</sup> (Lindqvist-structure); 9b) [Mo <sub>7</sub> O <sub>24</sub> ] <sup>6-</sup> ; 9c) [XM <sub>6</sub> O <sub>24</sub> ] <sup>n-</sup> (Anderson-structure); 9d) [XM <sub>12</sub> O <sub>40</sub> ] <sup>n-</sup> (Keggin-structure); 9e) [X <sub>2</sub> M <sub>18</sub> O <sub>62</sub> ] <sup>n-</sup> (Dawson-structure). .....	17
Fig 1.7 Molecular structure of [P <sub>8</sub> W <sub>48</sub> O <sub>184</sub> ] <sup>40-</sup> and its encapsulation complex [Cu <sub>20</sub> Cl(OH) <sub>24</sub> (H <sub>2</sub> O) <sub>12</sub> (P <sub>8</sub> W <sub>48</sub> O <sub>184</sub> )] <sup>25-</sup> .....	22
Fig 1.8 Structure of {Mo <sub>132</sub> } {Mo <sub>72</sub> Fe <sub>30</sub> } and {Mo <sub>75</sub> V <sub>20</sub> } clusters .....	24
Fig 1.9 Molecular structure of {Mo <sub>154</sub> } and {Mo <sub>176</sub> } clusters showing the basic {Mo <sub>8</sub> } and {Mo <sub>2</sub> } units (the equatorial {Mo <sub>1</sub> } units are not visible in this representation), and the expanded view of Mo-O-Eu groups linking the two cluster rings .....	26
Fig 1.10 Molecular structure of {Mo <sub>368</sub> } .....	27
Fig 1.11 Primary building unit [Mo <sub>2</sub> S <sub>2</sub> O <sub>2</sub> (H <sub>2</sub> O) <sub>6</sub> ] <sup>2+</sup> .....	28
Fig 1.12 Molecular structure of [Mo <sub>12</sub> S <sub>12</sub> O <sub>12</sub> (OH) <sub>12</sub> (H <sub>2</sub> O) <sub>6</sub> ] and [Mo <sub>12</sub> -pim] .....	29
Fig 1.13 Illustration of LbL assembly fabrication .....	31
Fig 2.1 Molecular structures of bridging ligands of this study .....	47
Fig 2.2 Synthetic route for {[RuCl <sub>2</sub> (dppb)](μ-N-N)} <sub>n</sub> .....	53
Fig 2.3 UV – Vis Spectra of DPB ligand and DPB complex in CH <sub>2</sub> Cl <sub>2</sub> ; AZP and AZP complex in CH <sub>2</sub> Cl <sub>2</sub> ; dipyTz and dipyTz complex in CHCl <sub>3</sub> .....	54

Fig 2.4 Raman spectra of DPB and $\{[\text{RuCl}_2(\text{dppb})](\mu\text{-DPB})\}_n$ .....	58
Fig 2.5 Raman spectra of dipyTz and $\{[\text{RuCl}_2(\text{dppb})](\mu\text{-dipyTz})\}_n$ .....	58
Fig 2.6 Raman spectra of $\{[\text{RuCl}_2(\text{dppb})](\mu\text{-AZP})\}_n$ .....	59
Fig 2.7 Raman spectra of $\{[\text{RuCl}_2(\text{dppb})](\mu\text{-pz})\}_n$ .....	59
Fig 2.8 Raman spectra of BP and $\{[\text{RuCl}_2(\text{dppb})](\mu\text{-BP})\}_n$ .....	60
Fig 2.9 Comparison of Raman spectra of $\{[\text{RuCl}_2(\text{dppb})](\mu\text{-N-N})\}_n$ (50~500 $\text{cm}^{-1}$ ) .....	56
Fig 2.10 $^1\text{H}$ NMR Spectra changes with increasing AZP complex concentration, the concentration of the bottom one is 16mM .....	64
Fig 2.11 $^1\text{H}$ NMR Spectra changes with increasing DPB complex concentration. The concentrations from top to bottom are 1mM, 5mM and 18mM respectively .....	65
Fig 2.12 $^1\text{H}$ NMR Spectra changes with increasing dipyTz complex concentration .....	66
Fig 2.13 Cyclic voltammetry of AZP complex at different scan rate in $\text{CH}_2\text{Cl}_2$ , electrolyte is 0.1M TBAP .....	70
Fig 2.14 Cyclic voltammetry of Pz complex in $\text{CH}_2\text{Cl}_2$ , electrolyte is 0.1M TBAP .....	71
Fig 2.15 SERS of $\{[\text{RuCl}_2(\text{dppb})](\mu\text{-BP})\}_4$ after removing chloroatoms and adding AZP as intersquare linker .....	76
Fig 3.1 AFM image of central part of drop-coated-square membrane using gold sputter coated mica as substrate .....	84
Fig 3.2 AFM images of drop-coated-square membrane on top of alumina .....	85
Fig 3.3 Molecular sieving test with $\{[\text{RuCl}_2(\text{dppb})](\mu\text{-pz})\}_4$ film. ....	87
Fig 3.4 Molecular sieving test with $\{[\text{RuCl}_2(\text{dppb})](\mu\text{-4,4'-bipy})\}_4$ film .....	88
Fig 3.5 Molecular Sieving Test with $\{[\text{RuCl}_2(\text{dppb})](\mu\text{-AZP})\}_4$ Film .....	89
Fig 4.1 Molecular structure of 2,5-Dihydroxy-1,4-benzenediacetic acid .....	97
Fig 4.2 Ball and Stick representations of $\text{Cs}_4[\text{W}_{16}\text{S}_{16}\text{O}_{16}(\text{OH})_{16}(\text{H}_2\text{O})_4(\text{C}_{10}\text{H}_8\text{O}_6)_2] \cdot 14\text{H}_2\text{O}$ .....	111

Fig 4.3 Raman spectrum of (a) 2,5-dihydroxy-1,4-benzenediacetic acid crystal (b) Cs <sub>4</sub> [W <sub>16</sub> S <sub>16</sub> O <sub>16</sub> (OH) <sub>16</sub> (H <sub>2</sub> O) <sub>4</sub> (C <sub>10</sub> H <sub>8</sub> O <sub>6</sub> ) <sub>2</sub> ]·14H <sub>2</sub> O crystal and SERS of (c)Cs <sub>4</sub> [W <sub>16</sub> S <sub>16</sub> O <sub>16</sub> (OH) <sub>16</sub> (H <sub>2</sub> O) <sub>4</sub> (C <sub>10</sub> H <sub>8</sub> O <sub>6</sub> ) <sub>2</sub> ]·14H <sub>2</sub> O aqueous solution with silver nanoparticles .....	113
Fig 4.4 <sup>1</sup> H NMR of Cs <sub>4</sub> [W <sub>16</sub> S <sub>16</sub> O <sub>16</sub> (OH) <sub>16</sub> (H <sub>2</sub> O) <sub>4</sub> (C <sub>10</sub> H <sub>8</sub> O <sub>6</sub> ) <sub>2</sub> ]·14H <sub>2</sub> O in D <sub>2</sub> O .....	114
Fig 4.5 Cyclic Voltammetry of 2,5-dihydroxy-1,4-benzenediacetic acid in PH 5 acetic buffer solution .....	116
Fig 4.6 Voltammetry of 2,5-dihydroxy-1,4-benzenediacetic acid in NaClO <sub>4</sub> at different PH, PH was adjusted by titrating HClO <sub>4</sub> or NaOH to the solution.....	116
Fig 4.7 Cyclic voltammetry of Cs <sub>4</sub> [W <sub>16</sub> S <sub>16</sub> O <sub>16</sub> (OH) <sub>16</sub> (H <sub>2</sub> O) <sub>4</sub> (C <sub>10</sub> H <sub>8</sub> O <sub>6</sub> ) <sub>2</sub> ]·14H <sub>2</sub> O in 0.1M NaClO <sub>4</sub> .....	120
Fig 4.8 Cyclic voltammetry of 2,5-dihydroxy-1,4-benzenediacetic acid in 0.1 M NaClO <sub>4</sub> .....	120
Fig 4.9 Extended structure of Cs <sub>4</sub> [W <sub>16</sub> S <sub>16</sub> O <sub>16</sub> (OH) <sub>16</sub> (H <sub>2</sub> O) <sub>4</sub> (C <sub>10</sub> H <sub>8</sub> O <sub>6</sub> ) <sub>2</sub> ]·14H <sub>2</sub> O, (a) view along with a axis (b) view along a axis with Cesium counter ions (c) zigzag diagram along an alternative axis (d) zigzag diagram with Cesium counter ions .....	121
Fig 5.1 Principles of hydrogen fuel cell operation.....	129
Fig 5.2 LbL formation of GC/(PDDA-AuNP/POM) <sub>n</sub> .....	134
Fig 5.3 The molecular structure of PDDA.....	135
Fig 5.4 UV–vis absorption spectrum of an aqueous solution of PDDA-protected AuNPs .....	135
Fig 5.5 TEM images of PDDA-Au <sub>NP</sub> and its size distribution diagram .....	136
Fig 5.6 CV of cobalt (II)-monosubstituted Dawson-type tungstodiphosphate anion in 0.1 M HClO <sub>4</sub> .....	138
Fig 5.7 The CVs of GC modified with (PDDA-AuNP/Co-Dawson) <sub>n</sub> , from inner to outer n= 2, 5,7,10,13, and 17.The POM layer is the outmost layer .....	138
Fig 5.8 The calibration curve of the first reduction peak current vs. the number of layers .....	139
Fig 5.9 The UV absorption of glass slide modified with (PDDA-AuNP/Co-Dawson) <sub>n</sub> , from bottom to top n= 3,4,5,6,7,8,9,10and 11. PDDA-AuNP is the outermost layer .....	142

Fig 5.10 Calibration curve of the absorption at 542nm vs. the number of layers .....	142
Fig 5.11 CVs of bulk gold electrode (dashed line) and GC modified with 13 bilayers (solid line) in 0.1 M HClO <sub>4</sub> solution.....	145
Fig 5.12 Calibration curve of gold nanoparticle area with increasing number of gold nanoparticle layers .....	145
Fig 5.13 Cyclic Voltammetry of GC/(PDDA-AuNP/Co-Dawson) <sub>13</sub> electrode in 1mM Ru(NH <sub>3</sub> ) <sub>6</sub> <sup>3+</sup> solution and 0.1M NaClO <sub>4</sub> .....	149
Fig 5.14 Cathodic peak current of GC/(PDDA-AuNP/Co-Dawson electrode in 1mM Ru(NH <sub>3</sub> ) <sub>6</sub> <sup>3+</sup> solution and 0.1 M NaClO <sub>4</sub> at different <i>n</i> .....	149
Fig 5.15 Oxygen reduction in 0.1M HClO <sub>4</sub> at electrode modified with different number of bilayer film, the outermost layer is POM.....	151
Fig 5.16 Oxygen reduction in 0.1M HClO <sub>4</sub> at electrode modified with different POM LbL assembly, the outermost layer is POM.....	151
Fig 5.17 Reduction of O <sub>2</sub> at a rotating GC disk electrode coated with 13 bilayers current- potential curves in O <sub>2</sub> -saturated 0.1 M HClO <sub>4</sub> .....	155
Fig 5.18 Levich plot of RDE measurement with (PDDA-Au <sub>NP</sub> /Co- Dawson) <sub>n</sub> , n=3 and 13 .....	155
Fig 5.19 Koutecky-Levich plot of RDE measurements with (PDDA- Au/Co-Dawson) <sub>n</sub> , n=3 and 13 .....	156
Fig 5.20 Tafel plot of RDE measurements with (PDDA-Au <sub>NP</sub> /CoDawson) <sub>13</sub> .....	157

**CHAPTER ONE**  
**SUPRAMOLECULAR ASSEMBLIES:**  
**BASIC CONCEPTS AND RECENT ADVANCES**

**1.1 Introduction**

Supramolecular assemblies are defined as complexes of molecules held together through noncovalent interactions such as hydrogen bonding, metal coordination, hydrophobic forces, van der Waals forces, pi-pi interactions and electrostatic effects. Supramolecular assemblies can refer to complexes composed of as simple as two units, for example, a DNA double helix or an inclusion compound, or large complexes that form sphere-, rod-, or sheet-like species whose dimension can range from nanometers to micrometers. Supramolecular assemblies are different from individual molecules (1–100 Å length scale) studied in traditional chemistry that require strong forces such as covalent or ionic bond to assemble atoms into discrete molecules and hold them together.

The initial motivation to build supramolecular assembly is the desire to synthesize new functional materials that can mimic biological systems in nature. In nature, the correct function of an organism is not solely dependent on individual components but the whole organization — the unique spatial arrangement of the components. Although biomaterial can be obtained and modified, the fragility and availability limit their potential applications. Therefore it is important to imitate nature's supramolecular design

motifs and generate robust nanostructured materials. Some applications using these synthesized supramolecular assemblies have been proven to be very successful.

Secondly, the desire to design new synthetic materials with even more powerful functions that benefit directly from nanoscale and microscale arrangement. This idea has been successfully developed by several researchers and will be addressed in detail later in this chapter.

Finally, supramolecular assemblies provide a more flexible and easier way to fabricate functional materials using a bottom-up approach. This perfectly solves the size limitation problems that exist in currently used “top-down” methods such as photolithography and can be used to develop ultra small electronic devices with improved performance. This should lead in the direction of hybrid devices in the future. Such devices will combine nonmolecular hard materials such as silicon that show outstanding electronic and photonic properties with soft molecular materials that display excellent bio-recognition, chemical sensing, and other designed properties to generate structures capable of diverse functionalities such as disease diagnosis, environmental monitoring, and so on.

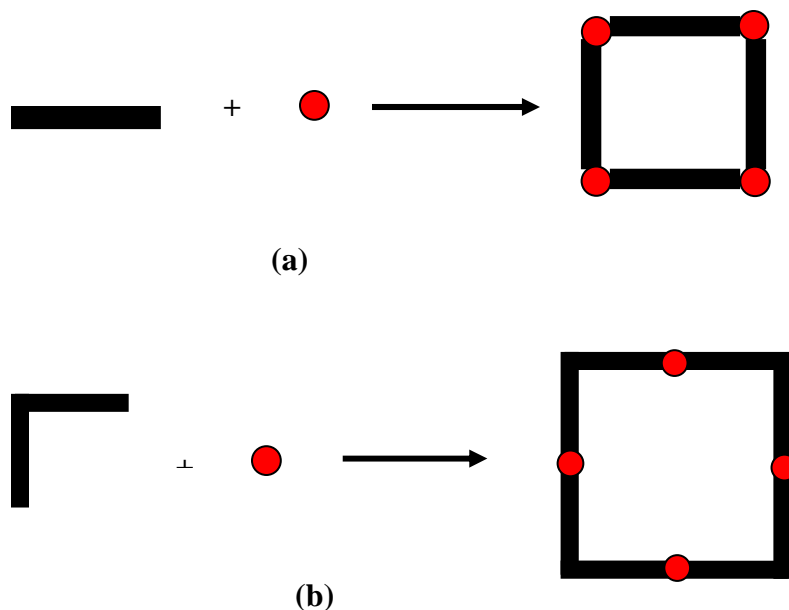
There are many strategies that can be used in building supramolecular assemblies such as dynamic covalent chemistry, molecular recognition and complexation, template-directed synthesis, mechanically-interlocked molecular architectures, biomimetics, imprinting, molecular machinery and building blocks of supramolecular chemistry. Among these, we have focused on transition metal directed self-assembly and polyoxometalate based supramolecular assemblies including cyclic polyoxometalate

encapsulated complex and polyoxometalate LBL assembly. In the following part, basic concepts and recent advances in these fields will be addressed.

## **1.2 Transition Metal Directed Supramolecular Assembly**

### **1.2.1 Introduction**

Transition metal directed self assembly offers an efficient way to build well defined architectures such as helices, grids, boxes and macrocycles with high yields compared to conventional organic synthesis. During the past two decades, this area has attracted tremendous attention due to the fact that it is simple to make, flexible in design and has many potential applications in various fields such as material chemistry, membrane separation and molecular recognition. Metal ligand assemblies with diverse shape, size and functionality have been developed. The general synthesis involves mixing the component ligands and metals at certain stoichiometry in solution. Among these assemblies, a type of assembly with square geometry (molecular square) is particularly interesting. Scheme 1.1 shows two general synthetic protocols for molecular squares. In method A, the corner of the transition metal is capped, so the ligand is forced to coordinate to the other two vacant sites with bond angle around  $90^\circ$ . The polydentate ligand then connects the metal moieties into a square with large void space in the middle. In method B, the ligand has a right angle and is coordinated to the transition metal in a linear orientation. By proper design of the transition metal group and bridging ligand, molecular squares with different properties can be achieved.



**Scheme 1.1** Synthetic Strategies of Molecular Square

### 1.2.2 Rhenium (I) Based Molecular Squares, *fac*-Re(CO)<sub>3</sub> X (X=Cl or Br) Corners

Hupp's group reported a series of tricarbonyl rhenium chloro corners based molecular squares. The squares are generally prepared by refluxing Re(CO)<sub>5</sub>Cl and pyridyl ligand in THF-Toluene solvent for 36 to 48 h. The strong trans labilizing effect of CO serves to activate two (and only two) carbonyls of Re(CO)<sub>5</sub>Cl for substitution—presumably first by solvent molecules (THF) and then by pyridyl ligands. The big advantage of rhenium over platinum- and palladium- containing assemblies is the octahedral coordination center which provides opportunities to build more complicated structures by replacing the chloride ions with functional ligands. However, to date this idea has not been demonstrated.



The ligands employed in such a system are listed in Fig. 1.1. They include pyrazine (PZ)<sup>1</sup>, 4,4'-bipyridine(BP)<sup>1</sup>, trans-1,2-bis(4-pyridyl)ethylene (BPE)<sup>1</sup>, 1,2-bis(4-pyridyl)acetylene (BPAC)<sup>2</sup>, 1,4-bis(pyridyl)butadiyne (DPB)<sup>3</sup>, 4,4'-Azodipyridine (AZP)<sup>3</sup>, and porphyrin derivatives<sup>4</sup>.

There are many special features of Re based molecular squares, the first being their photo property. Squares 1a, 1b, 1d and 1e exhibit luminescence at room temperature although their emissive excited state lifetimes ( $\tau$ ) are significantly shorter than the corresponding monomeric “corner” complexes  $(\text{CO})_3(\text{L})_2\text{Cl}$  indicating some intramolecular quenching effects in such a square arrangement. Squares 1c and 1f are not detectably luminescent at room temperature which was attributed to an enhanced nonradiative decay. Despite the shorter lifetimes of squares in solution phase, the luminescence quenching effects of 1d towards certain quenchers in solid film are more significant than that of its corner. This is due to the porosity that exists in the film providing cavities for binding quencher molecules. Studies have been shown that quenchers with high vapor pressures and more nitro groups result in greater quenching effects.<sup>3</sup>

The second significant feature as shown by X-ray structural studies is the squares have tendency for an extended, one-dimensional channel formation. In addition, the charge neutrality of these materials avoids the channel-blocking effect by counter ions. These two factors make Re based molecular squares good candidates for molecular sieving. The prepared membrane with 1a, 1b, and 1f are exceptionally porous indicated by electrochemical transport experiment. If the size of the electroactive permeants is smaller than the porosity of the square, the permeant will be able to diffuse onto the

electrode substrate and the current can then be detected; otherwise, permeant will be blocked and no electric signal or trace amount of current can be measured. In contrast, the membrane made solely from monometallic “corner” materials blocked all the permeants investigated.<sup>5</sup>

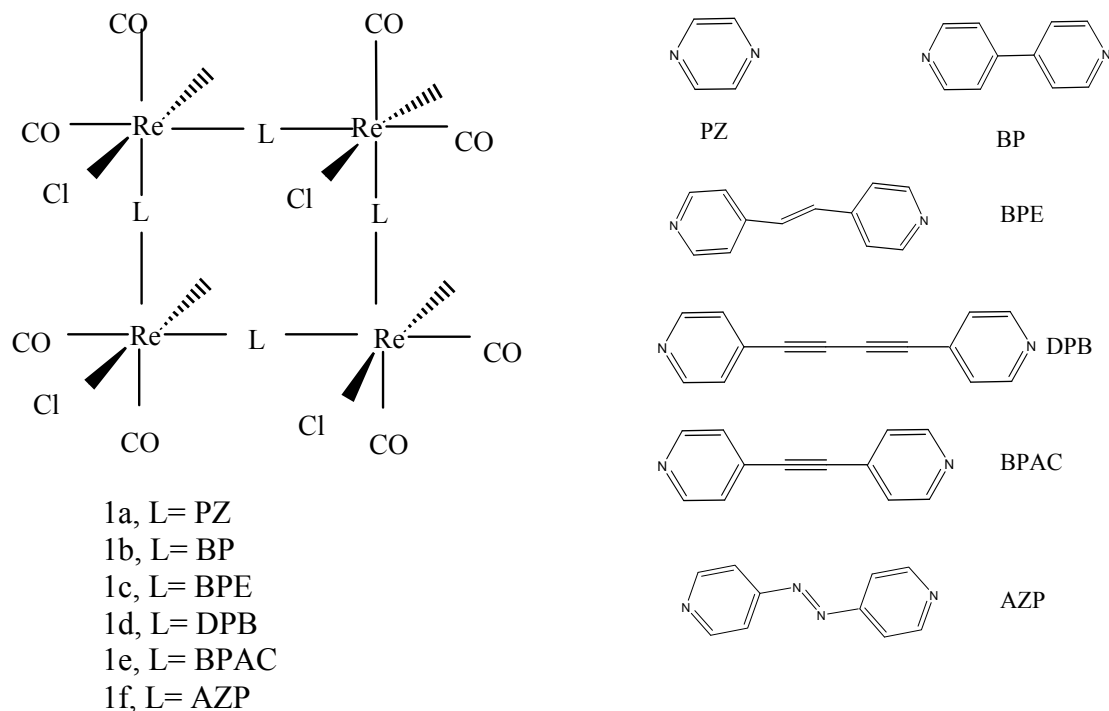
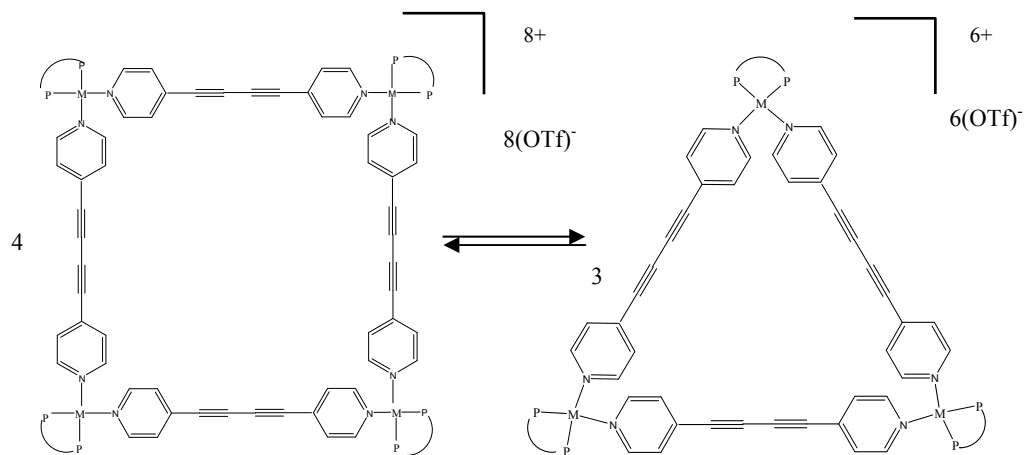


**Fig 1.1** Rhenium based molecular squares

### 1.2.3 Pd(II) and Pt(II) Based Molecular Squares

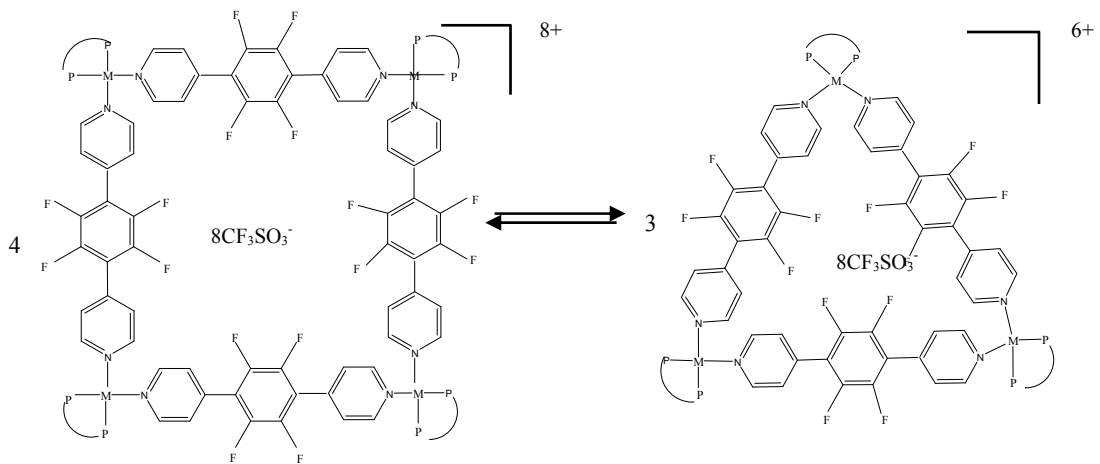
Although molecular squares are expected from the combination of right-angular components and linear ditopic units, the simultaneous self-assembly of molecular triangles have been reported. These two species are in equilibrium with each other and the process is under thermodynamic control in which the molecular square is favored in terms of enthalpy and the molecular triangle is favored in terms of entropy. Most Pd and

Pt based complexes end up with mixtures of triangles and squares, few can be isolated as pure squares or pure triangles. To study the factors that govern the equilibrium process, Ferrer designed a series of complexes containing cis-M(II)(di-phosphine) corners where M = Pd or Pt; diphosphine = dppp (1,3-bis(diphenylphosphino)propane), dppf (1,1'-bis(diphenylphosphino)ferrocene), depe (1,2-bis(diethylphosphino) ethane) and dppbz(1,2-bis(diphenylphosphino)-benzene) and bidentate ligand 1,4-bis(4-pyridyl)tetrafluorobenzene (BPTFB) and DPB.<sup>6, 7</sup> Their structures are shown in Fig 1.2. The complexes were synthesized by mixing and stirring bridging ligands and metal corners [cis-M(II)(di-phosphine)(H<sub>2</sub>O)<sub>2</sub>](OTf)<sub>2</sub> in either CH<sub>3</sub>NO<sub>2</sub> or CH<sub>2</sub>Cl<sub>2</sub> for about 2-3 hours and were characterized using <sup>1</sup>H, <sup>31</sup>P{<sup>1</sup>H}, <sup>19</sup>F, <sup>195</sup>Pt{<sup>1</sup>H} NMR, ES-MS, FAB(+) and computer modeling. The resulted products are listed in Table 1.1 Most of the complexes formed mixtures which showed concentration dependence except for complex 2c and 2e. Despite the bite angle of depe is smaller than dppp, triangles were the abundant product at low concentrations in most cases. The study showed that many factors such as the rigidity of the building blocks, the value of the angle of the adjacent coordination sites, and the lability of the metal-pyridine bond would all affect the completion of the self-assembly process. Thus it is very difficult to predict the composition of the equilibrium (squares or triangles) in a straightforward way. In a more recent study, they used cis-M(II)(N-N) where M = Pd, Pt; N-N = Ethylenediamine, 4,4'-substituted 2,2'-bipyridine as corners and 1,4-bis (4-pyridyl) tetrafluorobenzene as edges and they could isolate the ethylenediamine (en) protected metal complex as pure squares.<sup>8</sup>



**2a**, M=Pd; PP=dppp  
**2b**, M=Pt; PP=dppp  
**2c**, M=Pd; PP=dppf  
**2d**, M=Pt; PP=dppf  
**2e**, M=Pd; PP=depe  
**2f**, M=Pt; PP=depe  
**2g**, M=Pd; PP=dnhbz

**2a'**, M=Pd; PP=dppp  
**2b'**, M=Pt; PP=dppp  
**2d'**, M=Pt; PP=dppf  
**2f'**, M=Pt; PP=depe  
**2g'**, M=Pd; PP=dppbz



**3a**, M=Pd; PP=dppp  
**3b**, M=Pt; PP=dppp  
**3c**, M=Pd; PP=dppf  
**3d**, M=Pt; PP=dppf  
**3e**, M=Pd; PP=depe  
**3f**, M=Pt; PP=depe

**3a'**, M=Pd; PP=dppp  
**3b'**, M=Pt; PP=dppp  
**3c'**, M=Pd; PP=dppf  
**3d'**, M=Pt; PP=dppf  
**3e'**, M=Pd; PP=depe  
**3f'**, M=Pt; PP=depe

**Fig 1.2** Pt (II) or Pd (II) based molecular squares

**Table 1.1** Triangle and Square Distribution with Different Metal Corner and Bridging Ligand

diphospine	Metal	triangle and square distribution			
		1,4-bis(4-pyridyl)tetrafluorobenzene		1,4-bis(pyridyl)butadiyne(DPB)	
		low concentration	high concentration	low concentration	high concentration
dppp (bite angle=91.56)	Pt	square dominate	square dominate	triangle dominate	square dominate
	Pd	square dominate	square dominate	triangle only (1mM)	square only (100mM)
dppf (bite angle=98.74)	Pt	triangle dominate	triangle decrease, still dominate	triangle dominate	triangle decrease, still dominate
	Pd	triangle dominate	triangle decrease, still dominate	square only, no concentration dependence	
depe (bite angle < 91.56)	Pt	triangle dominate	square dominate	triangle dominate	triangle decrease, still dominate
	Pd	triangle dominate	square dominate	square only, no concentration dependence	
dppbz	Pd			mixture, triangle dominate	square only

### 1.2.4 Chiral Molecular Squares

Chiral molecular squares are of interest due to their potential applications in enantioselective events such as asymmetric catalysis and chiral sensing. The chirality of molecular square comes from three sources: (1) metallocorners with chiral capping groups, (2) metal-based chirality due to specific coordination arrangements, and (3) chiral bridging ligands. Lin's group has done a lot of work in this area.<sup>9</sup> They developed a series of enantiopure linear 1,1'-binaphthyl-derived bipyridyl bridging ligands and they used these ligands to build molecular squares (Fig 1.3). Applications using these chiral squares have also been demonstrated. For example, molecular square 4 with Pt(diimine) metallocorners showed high electroluminescent properties and was used to build light-emitting devices. The self-aggregation quenching of molecular square 4 thin film was alleviated by doping the squares into a well-known hole-transport polymer, poly (N-vinylcarbazole) (PVK). In the EL measurement, the maximum brightness of prepared blends with 5wt% of square 4 can reach 5470 cd/ m<sup>2</sup> with a maximum luminous efficiency of 0.93 cd A<sup>-1</sup>, which is much superior than the reported bis(acetylide)Pt(II) complexes.<sup>10</sup>

Another chiral molecular square (5) containing 1,1'-binaphthyl-derived bipyridyl bridging ligands and fac-Re(CO)<sub>3</sub>Cl corners exhibited enantioselective luminescence quenching for 2-amino-1-propanol analyte. The Stern-Völmer quenching constants  $K_{sv}$  were determined to be 7.35 M<sup>-1</sup> and 6.02 M<sup>-1</sup> in the presence of (S)-2-amino-1-propanol and (R)-2-amino-1-propanol respectively, leading to an enantioselectivity factor ( $k_{sv}(R-S)/k_{sv}(R-R)$ ) of 1.22 in favor of (S)-2-amino-1-propanol. The opposite trend in enantioselectivity was observed for the luminescence quenching of (S)-4 by the same

analyte. Therefore, the square and analyte with opposite configurations comprise a good match for better luminescence quenching. In addition, the enantioselectivity of squares is better than that of free ligands indicating the square can form better chiral environment.<sup>11</sup>

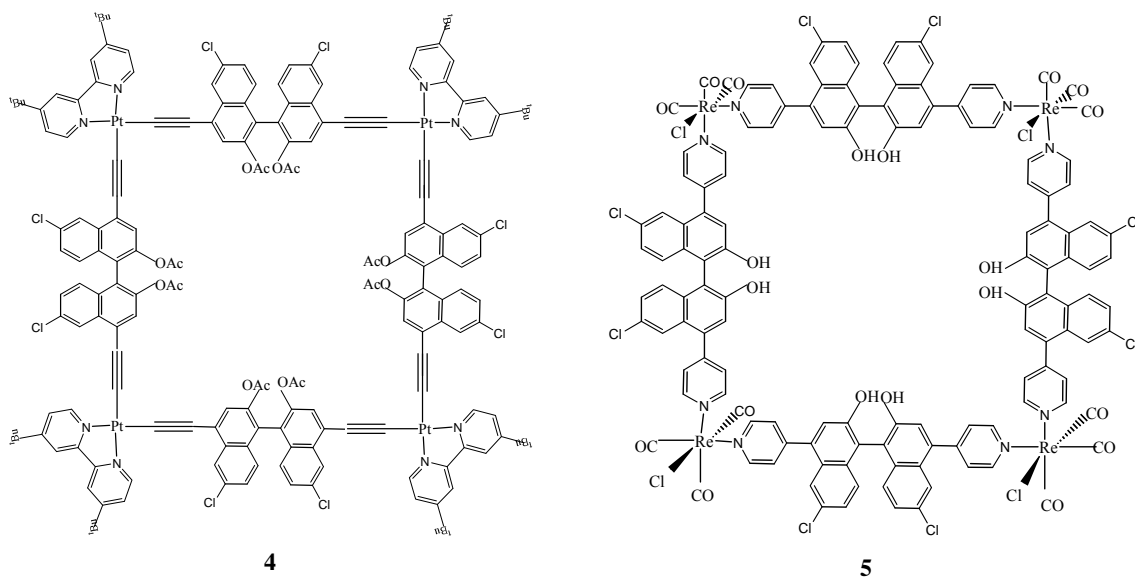


**Fig 1.3** Structure of some chiral molecular squares

### 1.2.5 Porphyrin Based Molecular Squares

Porphyrin based molecular squares are another important subclass in the family of metal directed self-assembly. The special attention to porphyrin or porphyrin-like molecules comes from their resembling many biological compounds such as hemes and chlorophylls. They have been widely used as catalysts, light collectors and energy movers. The incorporation of porphyrin into molecular squares offers a unique environment thus more interesting properties. The first porphyrin squares (6 and 7) were reported by Drain and Lehn in 1994.<sup>12</sup> They also showed the flexible design using porphyrin ligands which can serve as either linear or angular components depending on where the donor

functional groups are located. Since then, porphyrin based molecular squares with different architectures have been developed and widely studied. Hupp and Osuka systematically reviewed the advances in this area.<sup>13, 14</sup> Among various functionalities, using porphyrin squares as photoelectrochemical energy conversion material is particularly interesting in terms of the solar cell development as an alternative energy source. In a solar cell device, the energy is converted by the following sequence: (1) The dyes are photo irradiated and the energy is transferred from the outermost layer to the innermost layer of the dye molecules. (2) The electrons are transferred from the inner layer of the dye molecules to the transparent indium tin-oxide electrode which will result in the oxidation of the dye molecules. (3) The oxidized dye molecules are then reduced back into their original state using a redox shuttle, usually iodide anion. (4) The oxidized redox shuttles finally diffuse onto a dark electrode to get reduced and complete the circuit. In the first step, multilayered dyes are more favorable for the collection of more photons. However the movement of the charge-compensating ions within or through the multilayer is a big problem. This can be solved by infusing a nanoporous electrode assembly with an electrolyte solution. A similar idea is to infuse the porous porphyrin multilayer dye with an electrolyte solution. This idea was tested in a conventional dye-sensitized solar cells (DSSCs) platform by Splan.<sup>15</sup> Unexpectedly the sensitized electrode produced cathodic photocurrents. This behavior was explained as the quenching of a porphyrin square's excited state to its ground state by  $I_3^-$  and the generating of an oxidized dye. Then the ground state redox was delivered to the ITO electrode through hopping. As a consequence, several phenomena were observed: (1) The photocurrent increased with the



increasing number of dye layers and light collecting time. (2) Only small photovoltage was generated. (3) The substitution of TiO<sub>2</sub> with ITO caused the operation failure.

The current research in the area of photoelectrochemical energy conversion focuses on the development of new porphyrin based molecules with fast energy transfer (EnT) so that it can function as light-harvesting antennae in the same way as nature photosynthetic systems. These squares are formed via axial ligation shown in Fig 1.5. From the first reported meso-pyridyl Zn(II)-porphyrin tetramer<sup>16, 17</sup> (Fig 1.5, 8b) to the recently reported Chlorophyll tetramers<sup>18</sup> (Fig 1.5 8a), the rate of the energy transfer has been increased about 20 times. This improvement was attributed to the larger transition dipole moment that existed in square 8a. Although much progress has been made, the fastest rate we have gotten so far using synthetic strategy is still 10 times slower than that observed in photosynthetic proteins. The focus of future work is to design and synthesize complexes with improved conjugation within the tetramer or optimal transition dipole moment orientation to further enhance the rate of EnT.

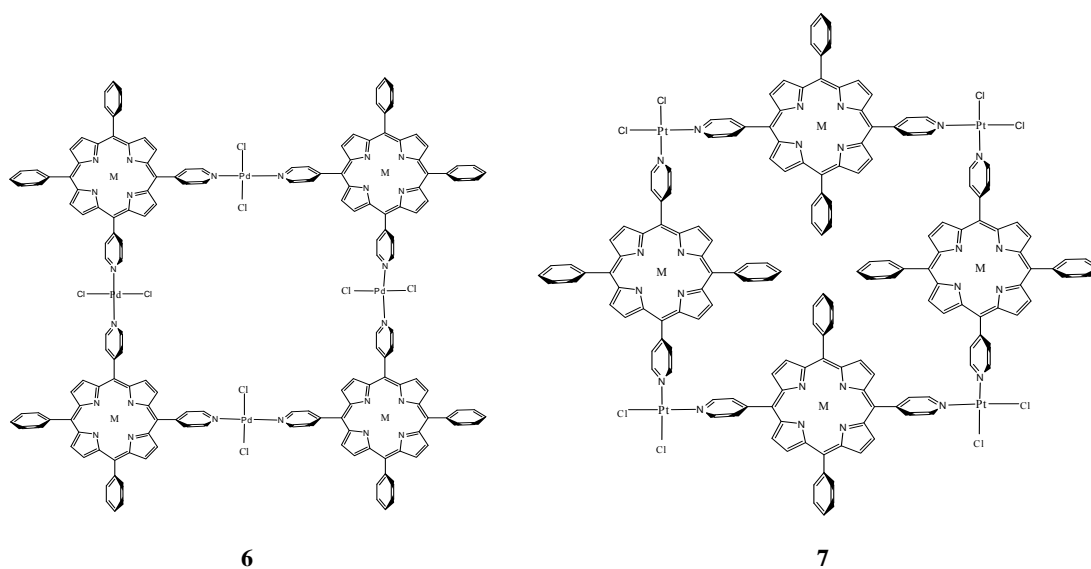


**Fig 1.4** Structure of porphyrin molecular squares reported by Drain and Lehn

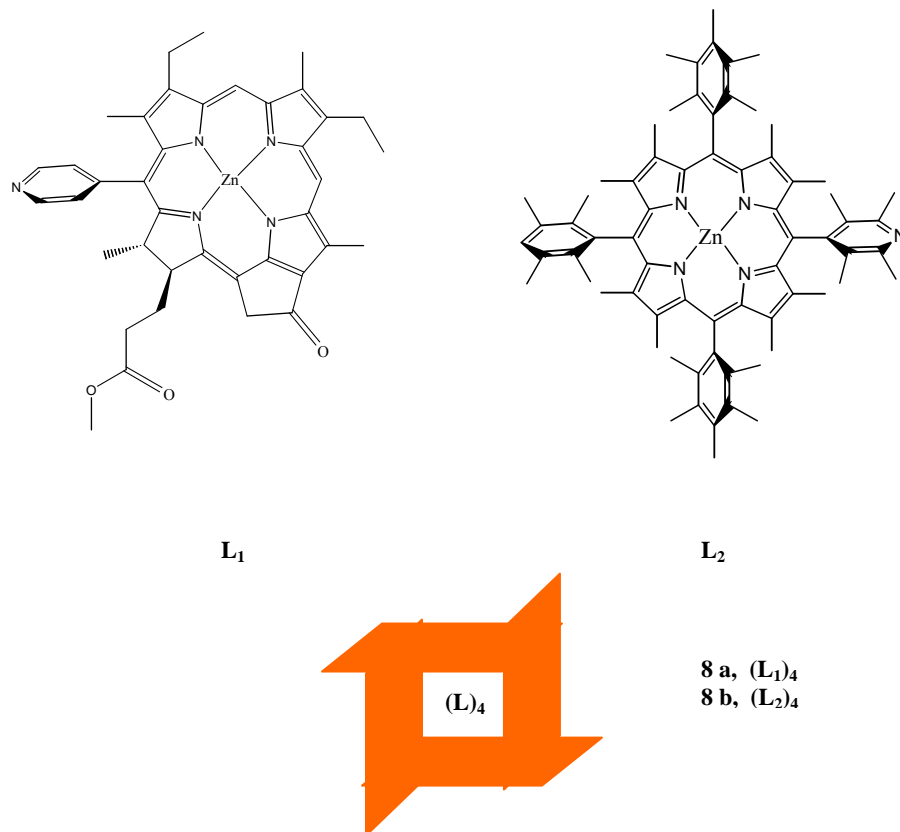


**Fig 1.5** Molecular Structures of  $(L)_4$ ,  $L = L_1$  and  $L_2$  respectively

### 1.3 Polyoxometalate based Supramolecular Assembly

#### 1.3.1 Introduction of Polyoxometalate

Polyoxometalates (POMs) are a large and distinctive class of inorganic compounds which have been applied in many fields such as chemistry, catalysis, materials science, and biomedicine for the last two centuries. The first POM "molybdenum blues" was reported by Berzelius in 1826; since then countless POMs with variable structures and properties have been synthesized and characterized. Polyoxometalates are usually formed by transition metals (mainly Vanadium, Molybdenum and Tungsten) and oxygen. Typically, the transition metals are on their

highest oxidation state and linked by oxo ligands ( $O^{2-}$ ). In the meanwhile other elements can be incorporated into the POM creating diversity within this type of material.

### ***1.3.1.1 Polyoxometalate Structure***

Polyoxometalates are generally classified as a type of coordination compound. The basic building block of POMs is the  $MO_n$  unit, where M is the metallic centre; O is the ligand although some POM derivatives may contain S, F, Br and other p-block elements as ligand; and n denotes the coordination number. 6 is the most common coordination number but it is not limited to 6; other numbers such as 4, 5 or 7 can also be seen. In addition to M and O, other elements labeled as X can be incorporated. A POM is usually classified by dividing it into two subgroups according to whether X is present in the POM or not. If X is not present, then POMs are called Isopolyanions (IPAs) or isopolyoxometalates and denoted as  $[M_nO_y]^{p-}$ ; If X is present, then POMs are called heteropolyanions (HPAs) or heteral polyoxometalate and denoted as  $[X_zM_nO_y]^{q-}$ , with  $z \leq n$ . In nomenclature, X is defined as primary, central or heteral atoms and M is defined as secondary, peripheral or addenda atoms. Occasionally, there are more than one type of addenda atoms in the POM framework, and such a molecule is called a mixed-addenda cluster. The POM building blocks can be presented using either ball and stick drawings or polyhedral drawings. The latter is more informative and is used for complicated structure representations. These building blocks can further form frameworks by sharing vertices, edges and even faces. Among these frameworks, the most well-known structure is the clathrate-like structure in which an internal unit is encapsulated by an external core denoted as  $I@E$  (I and E are the internal and external fragments). It includes Keggin, Wells-Dawson and Lindqvist anions.

The corresponding denotation using I@E form will be as follows:

$[\text{XO}_4]^{n-} @ \text{M}_{12}\text{O}_{36}$	Keggin
$[\text{XO}_4]_2^{n-} @ \text{M}_{18}\text{O}_{54}$	Wells-Dawson
$\text{O}^{2-} @ \text{M}_6\text{O}_{18}$	Lindqvist

### 1.3.1.2 Common Structures of Iso- and Heteropolyoxometalates<sup>19</sup>

Fig 1.6 (9a) shows Lindqvist structure which has a general formula of  $[\text{M}_6\text{O}_{19}]^{n-}$ . Six octahedral ( $\text{MO}_n$  building block) were arranged into an octahedral by sharing four edges with four neighboring octahedrals. This compact arrangement can be viewed as a fragment of a cubic close-packed metal oxide.

Figure 1.6 (9b) and (9c) represent the structure of compounds with the same general formula  $[\text{M}_7\text{O}_{24}]^{n-}$ . The bent structure in Figure 1.6 (9b) is adopted by the isopolymolybdate  $[\text{Mo}_7\text{O}_{24}]^{6-}$ , the so called paramolybdate. An Anderson structure with a general formula of  $[\text{XM}_6\text{O}_{24}]^{n-}$  is presented in Figure 1.6 (9c). The central heteroatom is surrounded by a planar hexagon formed by six edge-sharing octahedrals. In the Anderson structure, X takes an octahedral coordination; while in the Keggin structure (Fig 1.6 9d) the heteroatoms are tetrahedrally coordinated. The Keggin structure has a general formula of  $[\text{XM}_{12}\text{O}_{40}]^{n-}$  with four trimetallic groups arranged around central  $\text{XO}_4$ . Finally, the Dawson structure of  $[\text{X}_2\text{M}_{18}\text{O}_{62}]^{n-}$  (Fig 1.6 9e) was formed by symmetrically combine the fragments of two Keggin ions with a trimetallic group removed from each. The top and bottom regions are normally called caps and the middle region is called the belt. Lacunary structures form when one or more metal ions are selectively removed from the saturated polyoxometalate. This can be achieved by adding base. The removed part will have vacancies and can be occupied by other metal or non-metal atoms. This is a

common strategy for modifying the structures and properties of POM. For the wells Dawson compound, if the substitution happens in the cap region, it is called  $\alpha$ -substitution; if the substitution happens in the belt region, then it is called  $\beta$  substitution.

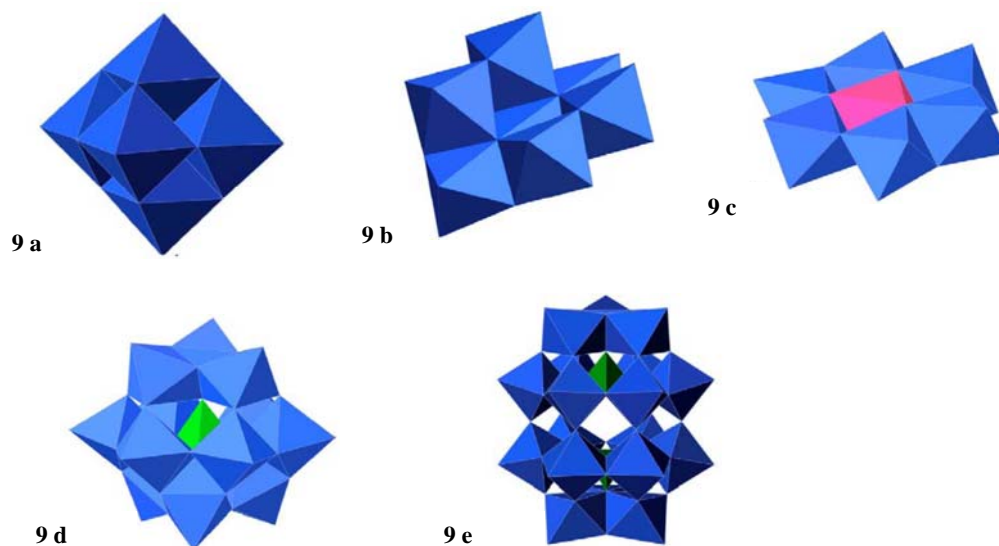


**Fig 1.6** Common Structures of Iso- and Heteropolyoxometalates 9a)  $[M_6O_{19}]^{n-}$  (Lindqvist-structure); 9b)  $[Mo_7O_{24}]^{6-}$ ; 9c)  $[XM_6O_{24}]^{n-}$  (Anderson-structure); 9d)  $[XM_{12}O_{40}]^{n-}$  (Keggin-structure); 9e)  $[X_2M_{18}O_{62}]^{n-}$  (Dawson-structure). Structures 9a~9e are reproduced with permission from citation <sup>19</sup> Copyright (2005) Frontiers in Bioscience

### 1.3.1.3 Features of Polyoxometalates

#### 1.3.1.3.1 Synthesis

In an aqueous solution, the highly positively charged transition metals (e.g. vanadium (V), molybdenum (VI), tungsten (VI)) tend to form stable complexes with oxo( $O^{2-}$ ) ligands ( $VO_4^{3-}$ ,  $MoO_4^{2-}$ ,  $WO_4^{2-}$ ). These building blocks can be further condensed into a packed molecular array of  $MO_6$  units by acidification. Precipitation will form after adding counter ions into the solution such as alkali metals or organic cations

like TBA. In order to fully characterize these clusters, crystals are usually grown. The synthetic process is repeatable. Depending on the boundary conditions such as stoichiometry, solvent, pH, temperature, concentration and counterions, variable compounds can be made by systematic control of these factors. Also, the condensation process is reversible. By adding base to the solution, the oxo bridges in POMs can be cleaved. The degradation can be easily controlled by the amount of base added. The therefore formed lacunary structure is very useful in terms of introducing another transition metal into the system. Polyoxometalates are very stable in the presence of air and water as well as modestly high temperatures.

#### ***1.3.1.3.2 Redox Properties***

As indicated above, the addenda atoms, M, are in their highest oxidation states in the POMs with electronic configurations of  $d^0$  or  $d^1$ . They are bonded to  $O^{2-}$  and form  $W^{6+}-O^{2-}$  or  $V^{5+}-O^{2-}$  pairs. These pairs generate infinite surfaces similar to that of metal oxide crystals. This provides POM clusters with good solubility in the liquid even though some POMs can reach nanometer scale. Depending on the heteroatom X (formally  $P^{5+}$ ,  $Al^{3+}$ ,  $I^{7+}$ ) and addenda metal M, the overall charge of polyoxometalate anions varies. Normally, the formal charge of M is between 4+ and 6+ and it changes with the reduction state. The reduction of POM is an important feature and the process is commonly accompanied by protonation. The strong oxidizing ability comes from the low-lying empty d-type orbitals of addenda atoms which can accept numerous electrons with no major geometry changes. The extra electrons filled in d-metal orbitals are named blue electrons. The name “blue electrons” originates from the intense blue color observed during the reduction of POMs. Later the term was extended to refer to the extra electrons

added to d-type orbitals no matter whether blue color is present or not. Certain M atoms have a strong ability to trap electrons and they are vividly called electron reservoirs. Although POMs are strong oxidizing agent, they are stable in solution and in the solid state with countercations balancing the negative charge.

#### ***1.3.1.3.3 Basicity:***

POMs are generally classified as polyacids. In most cases, they are strong acids with  $\text{PK}_a$  less than 0. However they are protonated in very acidic media. In a POM framework, not all the oxygen sites are identically acidic or basic. It varies with the environment such as the covalency/ionicity of the M-O bond, the number of surrounding M atoms and the intrinsic property of M. POMs are important catalysts for certain reactions, and the catalysis process is usually accompanied with proton transfer. Also as introduced in the synthesis section, the addition of POMs to acidic media will initiate polymerization reaction.

Some general trends of polyoxometalate are listed below:

Brønsted acidity:  $\text{H}_3\text{PW}_{12}\text{O}_{40} > \text{H}_4\text{PVW}_{11}\text{O}_{40} > \text{H}_4\text{SiW}_{12}\text{O}_{40} > \text{H}_3\text{PMo}_{12}\text{O}_{40} > \text{H}_4\text{SiMo}_{12}\text{O}_{40}$

Polyoxoanion basicity:

$[\text{SiW}_{12}\text{O}_{40}]^{4-} > [\text{GeW}_{12}\text{O}_{40}]^{4-} > [\text{PW}_{12}\text{O}_{40}]^{3-} > [\text{PMo}_{12}\text{O}_{40}]^{3-} > [\text{SiMo}_{12}\text{O}_{40}]^{4-}$

### **1.3.2 Polyoxometalate Encapsulation Assembly**

#### ***1.3.2.1 Introduction***

Inorganic host-guest system is an important branch of supramolecular chemistry. Among these, large polyoxometalate clusters with a wheel or ball shape constitute a significant part of inorganic hosts. Today various POM clusters have been prepared due to the improvement of instrumentation for crystal diffraction data collection as well as the

advent of structure solution and refinement. The largest POM  $\{\text{Mo}_{368}\}$  has a size similar to protein. This provides a synthetic way to build an artificial biological system. Most interestingly, these giant POM clusters can incorporate various guest molecules into their cavity sites. The following will introduce several types of POM host systems and their interaction with the guest molecules.

### **1.3.2.2 $\text{K}_{28}\text{Li}_5\text{H}_7\text{P}_8\text{W}_{48}\text{O}_{184}$ Encapsulation Complex**

A large crown shape discrete polyanion  $[\text{P}_8\text{W}_{48}\text{O}_{184}]^{40-}$  with a central cavity (10 Å in diameter) can be isolated by the condensation of four  $[\text{H}_2\text{P}_2\text{W}_{12}\text{O}_{48}]^{12-}$  lacunary polyanions.<sup>20</sup> The structure is shown in Fig 1.7 (10). The sub building block of  $[\text{H}_2\text{P}_2\text{W}_{12}\text{O}_{48}]^{12-}$  is derived from the Wells Dawson structure of  $[\text{P}_2\text{W}_{18}\text{O}_{62}]^{6-}$  by removing six adjacent  $\text{WO}_6$  octahedrals. Two  $\text{WO}_6$  are from the cap region and four  $\text{WO}_6$  are from the belt region. The study done by Roland and Contant suggested that  $\text{P}_8\text{W}_{48}$  did not form a complex with divalent or trivalent-metal ions. In basic solution, the precipitate formed and in acidic solution, the successive addition of cobalt (II) did not constitute any significant absorption break indicating no stable compound formed during the process. Their study also showed that the polyanions tended to form ion aggregates or outer-sphere complexes rather than inner sphere complexes. These observations prevented the exploration of using  $\text{P}_8\text{W}_{48}$  as a precursor until 20 years later. Mal and Kortz reported its first encapsulation complex  $[\text{Cu}_{20}\text{Cl}(\text{OH})_{24}(\text{H}_2\text{O})_{12}(\text{P}_8\text{W}_{48}\text{O}_{184})]^{25-}$  (11 in Fig 1.7).<sup>21</sup> The complex was formed by mixing  $\text{CuCl}_2 \cdot 2\text{H}_2\text{O}$  and  $\text{K}_{28}\text{Li}_5[\text{H}_7\text{P}_8\text{W}_{48}\text{O}_{184}] \cdot 92\text{H}_2\text{O}$  in  $\text{CH}_3\text{COOLi}$  PH 6 buffer solution and heating at 80° for 1 hour. The electrochemistry of the Cu encapsulated complex has also been studied.<sup>22</sup> The cyclic voltammetry of the complex shows dominant peaks due to the reduction of copper in both pH 0 and pH 5



media. Since the tungsten centers are very sensitive to pH change, the tungsten reduction peaks can be better defined at pH 5. The cyclic voltammetry from the complex is different from that obtained by mixing copper salt and  $P_8W_{48}$  anion at proper ratio at room temperature indicating the complex are very stable in the solution. The copper encapsulated complex also shows good catalytic activity towards nitrate and nitrite reduction. The improved catalytic activity can be attributed to the accumulation of more copper atoms inside  $P_8W_{48}$  as well as the more positive potential locations of catalytically active Cu- and W-waves.

More interestingly, a study done by Liu showed that  $[Cu_{20}Cl(OH)_{24}(H_2O)_{12}(P_8W_{48}O_{184})]^{25-}$  could self-assemble into single-layer, hollow spheres which are usually referred to as “blackberry” structures in solution.<sup>23</sup> The dynamic light scattering (DLS) and static light scattering (SLS) confirm the continuous growth of copper complex until they reach equilibrium with the formation of spheres (76 nm in diameter). There is an initial delay with no obvious change in scattered light intensity which is attributed to the kinetic process, the period of which varies depending on the microionic structure, temperature, solution PH, ionic strength and solvent composition. Also structure analysis based on SLS suggests the possibility of a large number of discrete macroions present in the solution in equilibrium with blackberries. Once the equilibrium is reached, the solution is very stable: the size of blackberries continues unchanged and no further growth or aggregate has been observed. The size and shape of the backberry structure are independent with the macroionic concentration and temperature. The SEM measurements showing a radius of 40 nm is consistent with the DLS and SLS studies. The zeta-potential analysis revealed that the alkali conterions

are associated or incorporated into the blackberry structure and facilitate the blackberry formation by balancing the charges of  $\{\text{Cu}_{20}\text{P}_8\text{W}_{48}\}$  macroanions and thus reducing the repulsion between  $\{\text{Cu}_{20}\text{P}_8\text{W}_{48}\}$ . This is the first reported non-molybdenum containing blackberry structure and are the smallest size macroions so far that can form blackberry structure. This provides useful information towards identifying the transition point from simple ions to macroions in dilute solutions.

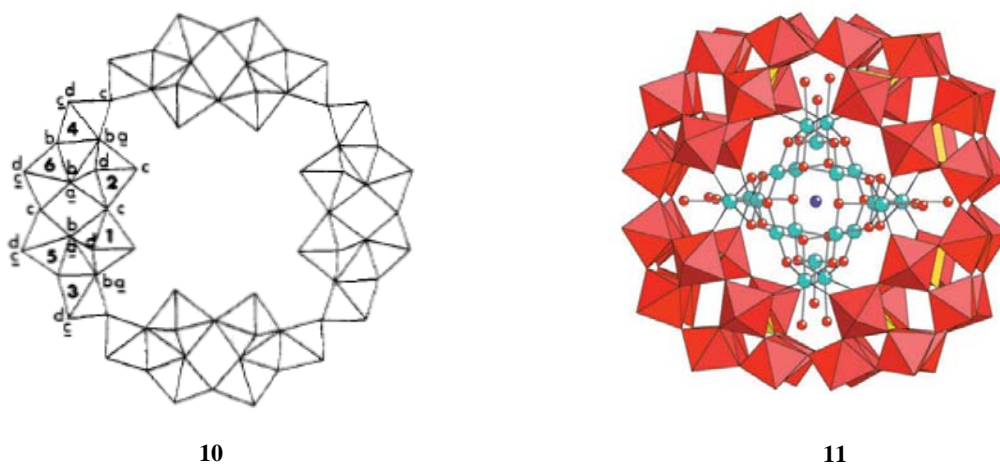


**Fig 1.7** Molecular structure of  $[\text{P}_8\text{W}_{48}\text{O}_{184}]^{40-}$  (left) and its encapsulation complex  $[\text{Cu}_{20}\text{Cl}(\text{OH})_{24}(\text{H}_2\text{O})_{12}(\text{P}_8\text{W}_{48}\text{O}_{184})]^{25-}$  (right). Structure 10 is reproduced with permission from citation <sup>20</sup> Copyright [1985] American Chemical Society and structure 11 is reproduced with permission from citation 21 Copyright (2005) Wiley-VCH Verlag GmbH &Co. KGaA.

### 1.3.2.3 Mo Based “Giant-Wheel/Sphere” Clusters and Its Encapsulation Complex

The “Giant-Wheel/Sphere” clusters constitute another important area in polyoxometalate chemistry. Most work done in this area was contributed by Müller.<sup>24-27</sup> The reduction of  $\text{Mo}^{\text{VI}}$ -type species in acid solutions ( $\text{pH} \leq 3$ ) can form a blue color solution (Mo blue) and sometimes a brown color solution (Mo brown) under strong

reduction conditions. Then by adding electrolytes, the polymerization or precipitation will result in the formation of giant wheel/sphere shaped clusters. The easiest way to characterize an MB solution is by measuring the resonance Raman spectrum with  $\lambda_e = 1064$  nm. Under such excitation conditions, the MB solution shows the characteristic features. These giant clusters can further lose  $\{\text{Mo}_2\}$  units which will generate defects in the structure. One example is  $\{\text{Mo}_{142}\}$  with 6  $\{\text{Mo}_2\}$  units missing compared to  $\{\text{Mo}_{154}\}$ . The generated defects greatly increase the overall negative charge of the cluster which requires high concentration electrolyte to isolate the cluster by incorporating more counter ions. In the meanwhile, the large negative charge can promote linking the cluster into chains or layers under related conditions. In addition, the defect sites allow the incorporation of electrophilic substrates. More detailed information can be found in the review by Müller.<sup>26</sup>

#### ***1.3.2.3.1 Sphere Clusters $\{\text{Mo}_{132}\}$ <sup>28</sup>:***

The building block of giant sphere clusters is pentagonal  $\{(\text{Mo})\text{Mo}_5\} \equiv \{(\text{Mo})^0(\text{Mo}_5)^I\}$  which is formed by linking central bipyramidal  $\text{MoO}_7$  ( $(\text{Mo})^0$ ) with 5  $\text{MoO}_6$  octahedrals ( $(\text{Mo}_5)^I$ ) through the edges. The building block can then be further connected into spherical-type clusters in the presence of linkers. For example, an icosahedral molecular system can be formed with  $\{\text{Mo}^V_2\text{O}_4\}^{2+}$  as linkers. The structure thus revealed is 12  $\{(\text{Mo})\text{Mo}_5\}$  linked by 30  $\{\text{Mo}^V_2\text{O}_4\}^{2+}$  linkers which can be formulated as  $\{\text{Mo}_{11}\}_{12} \equiv \{(\text{Mo})^0(\text{Mo}_5)^I(\text{Mo}_5)^V\}_{12}$ . Structure 12 is shown in Fig.1.8. Interestingly, the solid of  $\{\text{Mo}_{132}\}$  resembles fullerene  $\text{C}_{60}$  and is commonly referred to “inorganic fullerene”.

The introduction of  $\text{FeCl}_3$  into  $\{\text{Mo}_{132}\}$  cause the substitution of  $\{\text{Mo}_2^{\text{V}}\}$  spacers by aqua-ligand- $\text{Fe}^{\text{III}}$  polyhedra, and the formation of  $\{\text{Mo}_{72}\text{Fe}_{30}\}$ <sup>29 24</sup>(13 in Fig 1.8) which shows a more compact structure than  $\{\text{Mo}_{132}\}$  due to the different nature of  $\text{Fe}^{\text{III}}$  spacers from that of  $\{\text{Mo}_2^{\text{V}}\}$ . Therefore the 12 pentagons are present as isolated forms in  $\{\text{Mo}_{132}\}$  and condensed forms in  $\{\text{Mo}_{72}\text{Fe}_{30}\}$ . The incorporation of 30  $\text{Fe}^{\text{III}}$  enables the cluster exhibit extraordinary magnetic properties. The vanadium derivatives such as  $\{\text{Mo}_{75}\text{V}_{20}\}$ <sup>24</sup> (14 in Fig 1.8),  $\{\text{Mo}_{80}\text{V}_{22}\}$ <sup>30</sup> also show significant magnetism. In all of these cases, the introduction of another species has some templating effect on the final enclosure product (size and shape). More interestingly, the  $\{\text{Mo}_{72}\text{Fe}_{30}\}$  cluster can further encapsulate Keggin-ion electron reservoirs and cross-link into a two-dimensional network.<sup>31</sup>

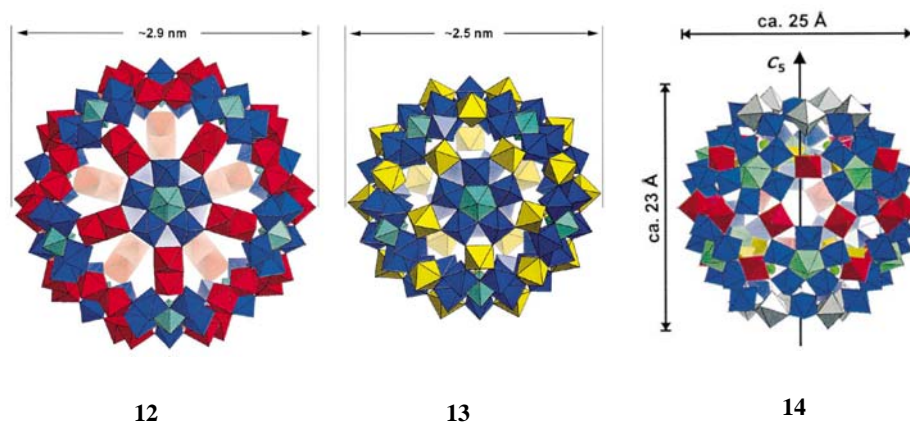


**Fig. 1.8** Structures of  $\{\text{Mo}_{132}\}$  (left)  $\{\text{Mo}_{72}\text{Fe}_{30}\}$  (middle) and  $\{\text{Mo}_{75}\text{V}_{20}\}$  (right) Reproduced with permission from citation 24 Copyright (2001) Elsevier

Another significant feature of  $\{\text{Mo}_{132}\}$  is its 20 well-defined pores  $\{\text{Mo}_9\text{O}_9\}$  with diameters of 0.6-0.8 nm. These pores functionalize as inorganic crown ethers and can be reversibly closed in the presence of guanidinium. Also the highly negatively charged clusters can mediate cations such as  $\text{Na}^+$ ,  $\text{Cs}^+$ ,  $\text{Ce}^{3+}$ ,  $\text{C}(\text{NH}_2)^{3+}$ , and  $\text{OC}(\text{NH}_2)\text{NH}_3^+$

transferring through the shell into internal cavities.<sup>33</sup> The  $\text{Li}^+$  NMR study of the cluster reveals a temperature dependant equilibrium process involved upon uptaking  $\text{Li}^+$  ions at low temperature and release  $\text{Li}^+$  ions at high temperature.<sup>32</sup> In addition, the “pore gating” was demonstrated that 20 pores shut off in the presence of protonated urea and reopened when uptaking  $\text{Ca}^{2+}$  ions followed by a closed state again.<sup>33, 34</sup> This vividly resembles biological ion transport. The  $\{\text{Mo}_{132}\}$  porous structure can be further tuned by introducing other units. The reported  $\{\text{Mo}_{80}\text{V}_{22}\}$ <sup>30</sup> with smaller  $\{\text{Mo}_6\text{O}_6\}$  pores and less symmetrical shell structures can only uptake smaller potassium ions.

#### ***1.3.2.3.2 Wheel Clusters $\{\text{Mo}_{154}\}$ or $\{\text{Mo}_{176}\}$ :***

In the above mentioned structure of  $\{\text{M}_{132}\}$ , the building block has a  $\text{C}_5$  symmetry. If the pentagonal building blocks  $\{(\text{Mo})\text{Mo}_5\}$  deform into a  $\text{C}_s$  symmetry, then the wheel shaped clusters such as  $\{\text{Mo}_{154}\}$  (16 in Fig 1.9) and  $\{\text{Mo}_{176}\}$  (15 in Fig 1.9) will be formed. The structure of these wheel shaped clusters can be formulated as  $[\{\text{Mo}_8\}\{\text{Mo}_2\}\{\text{Mo}_1\}]_m$ . When  $m=14$ , the  $\{\text{Mo}_{154}\}$  forms, while when  $m=16$ ,  $\{\text{Mo}_{176}\}$  forms.  $\{\text{Mo}_{154}\}$  and  $\{\text{Mo}_{176}\}$  have an external diameter of 3.4 nm and 4.1 nm respectively.

The incorporation of the Eu(III) ions into  $\{\text{Mo}_{154}\}$  leads to a giant dimeric cluster  $\{\text{Mo}_{256}\text{Eu}_8\} = [\{\text{Mo}_{128}\text{Eu}_4\text{O}_{388}\text{H}_{10}(\text{H}_2\text{O})_{81}\}_2]^{20-}$  (17 in Fig 1.9) with a diameter of 4 nm<sup>35</sup>. The formation of a dimer is caused by the Eu(III) ions which acts as a symmetry breaker that prevents the highly symmetrical parent-ring from closing.

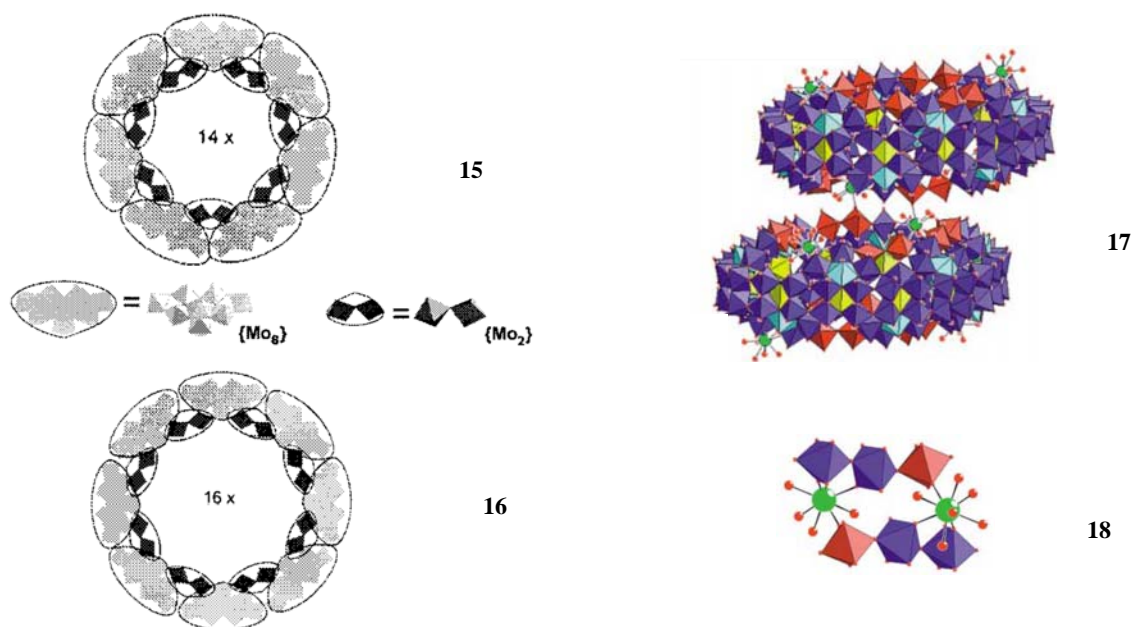
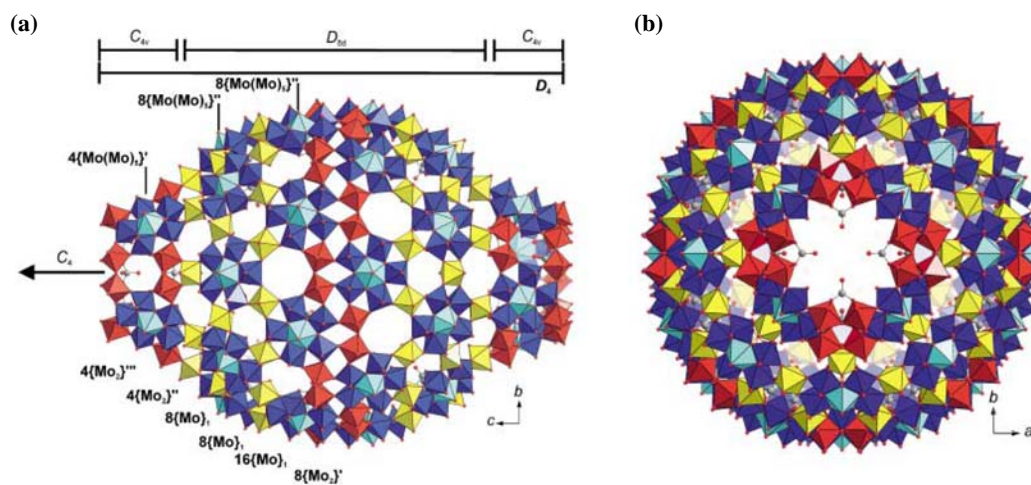


**Fig. 1.9** Molecular structure of  $\{\text{Mo}_{154}\}$  (15) and  $\{\text{Mo}_{176}\}$  (16) clusters showing the basic  $\{\text{Mo}_8\}$  and  $\{\text{Mo}_2\}$  units (the equatorial  $\{\text{Mo}_1\}$  units are not visible in this representation), and the expanded view of Mo-O-Eu groups linking the two cluster rings (18) Structure 15,16 are reproduced with permission from citation <sup>25</sup> Copyright 2000 American Chemical Society and structure 17,18 are reproduced with permission from <sup>35</sup> Copyright (2002) Wiley-VCH Verlag GmbH & Co. KGaA.

### 1.3.2.3.3 Blue Lemon $\{\text{Mo}_{368}\}$ :

The giant lemon shape  $\{\text{Mo}_{368}\}$ <sup>36</sup> was formed in the presence of sulfate anions (Fig 1.10). This is so far the largest reported polyoxometalate cluster with an external diameter of 6 nm. It consisted of 64  $\{\text{Mo}_1\}$ , 32  $\{\text{Mo}_2\}$  and 40  $\{(\text{Mo}) \text{Mo}_5\}$  (32 with sulphate ligand and 8 without). The structure can be regarded as a mixture of  $\{\text{Mo}_{176}/\text{Mo}_{154}\}$  type clusters and  $\{\text{Mo}_{132}\}$  type clusters with 24  $\{\text{Mo}_{11}\}$  units of  $C_5$  symmetry and 16  $\{\text{Mo}_{10}\}$  units of Cs symmetry which have one  $\text{MO}_6$  octahedral removed compared to the  $\{\text{Mo}_{11}\}$  units in the  $\{\text{Mo}_{132}\}$  structure.  $\{\text{Mo}_{368}\}$  contains a

central part  $\{\text{Mo}_{288}\} \equiv \{\text{Mo}_{288}\text{O}_{784}(\text{H}_2\text{O})_{192}(\text{SO}_4)_{32}\}$  showing ball shaped fragments with  $D_{8d}$  symmetry and two capping regions  $\{\text{Mo}_{40}\} \equiv \{\text{Mo}_{40}\text{O}_{124}(\text{H}_2\text{O})_{24}(\text{SO}_4)_8\}$  having a  $C_{4v}$  symmetry.



19

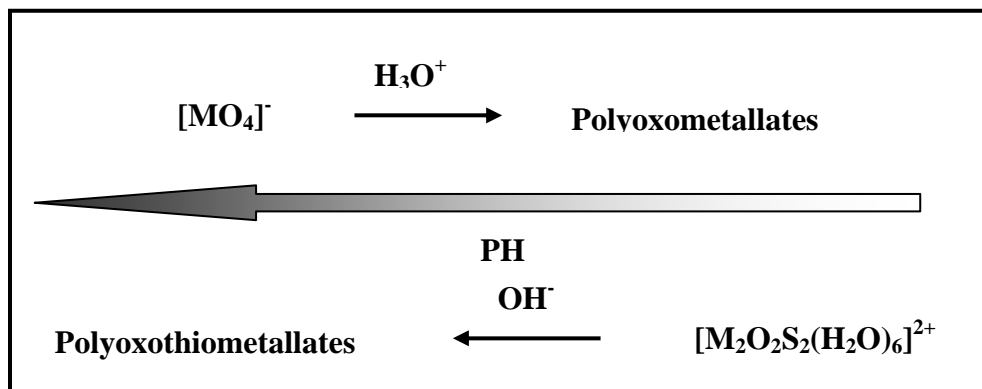
**Fig 1.10** Molecular structure of  $\{\text{Mo}_{368}\}$ : (a) and (b) are representations perpendicular to the  $C_4$  axis and along the  $C_4$  axis respectively. Reproduced with permission from citation <sup>36</sup> Copyright (2002) Wiley-VCH Verlag GmbH & Co. KGaA.

#### 1.3.2.4 Polythiooxometalate and Its Encapsulation Complex

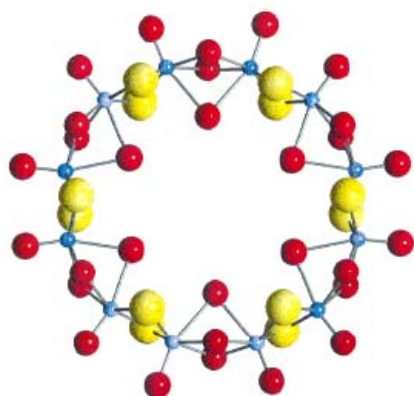
Polythiooxometalate is another important polyoxometalate that can form cyclic ring structures. The work in this area is mainly contributed by Cadot's group.<sup>37, 38</sup> The basic building block of Polythiooxometalate is  $[\text{M}_2\text{O}_2\text{S}_2]^{2+}$  ( $\text{M} = \text{Mo}$  or  $\text{W}$ ), whose structure is shown in Fig 1.11. In contrast to the acidification of basic monomeric oxoanions  $[\text{MO}_4]^{2-}$  ( $\text{M} = \text{Mo}$  or  $\text{W}$ ) to form polyoxometalates, in which the aggregation process was directed in the presence of small anionic assembling groups with fixed geometry, for example tetrahedral (phosphate or silicate) or trigonal (arsenite or antimonate), the dinuclear oxo-thio cations  $[\text{M}_2\text{O}_2\text{S}_2]^{2+}$  ( $\text{M} = \text{Mo}$  or  $\text{W}$ ) undergo the



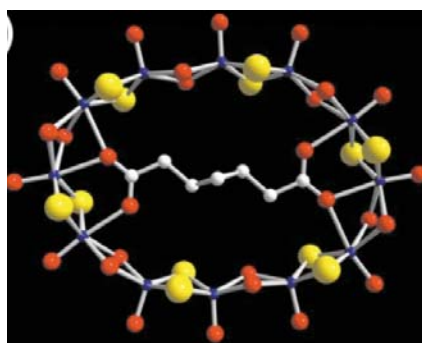




**Scheme 1.2** Illustration of the formation process of Polyoxometallates and Polyoxothiometalates



20



21

**Fig 1.12** Molecular structure of  $[Mo_{12}S_{12}O_{12}(OH)_{12}(H_2O)_6]$  (20) and  $[Mo_{12}\text{-pim}]^{2-}$  complex (21). Structure 20 was reproduced with permission from citation <sup>39</sup> Copyright (1998) Wiley-VCH Verlag GmbH & Co. KGaA, and 21 was reproduced from citation <sup>37</sup> by permission of The Royal Society of Chemistry

### **1.3.3 Polyoxometalate Based LBL Assembly**

#### ***1.3.1.1 Introduction of LBL Assembly***

Layer by layer assembly (LBL) is a technique to form superamolecular structures through electrostatic interactions (conventional way). It was first reported by Iler in 1966 that multilayer thin film can be fabricated by alternative deposition of oppositely charged nanoparticles.<sup>40</sup> In addition to charged colloids, they also pointed out the potentials of using other charged species such as polyvalent ions, surfactants, water soluble polymer and even proteins to build the multilayer assembly. However, their suggestive work did not get public attention until later. Decher and Hong rediscovered and established the work in this area.<sup>41, 42</sup> In 1997, a feature article named “Fuzzy Nanoassemblies: Toward Layered Polymeric Multicomposites”, published in *Science* by Decher, systematically reviewed the work of LBL assembly.<sup>43</sup>

LBL assembly can be built through conventional methods such as electrostatic interactions, hydrogen bonding, step by step reaction, surface sol-gel process, molecular recognition and bio-recognition, charge transfer interaction, stepwise stereocomplex formation, and electrochemical deposition, as well as unconventional methods such as inclusion complexes, noncovalent modification, coordination polyelectrolyte, electrostatic complex formation, and block copolymer micelles.<sup>44</sup> In this study, LBL assembly mainly covers the assembly of charged species.

The preparation of LBL is relatively easy without sophisticated procedures or instruments. Beakers containing dipping solutions and waters are all we need. The detailed preparation process of LBL assembly is shown in Fig 1.13. First, substrates with cleaned hydrophilic surfaces such as glass, silica or mica, which exhibit a nonzero

surface charge, must be employed. The deposition of a first layer is achieved by dipping the charged substrate into a solution of a polyion of opposite charge. After a typical 20 min immersion, the substrate is washed in water to remove excess polyions. During this process, the adsorption of a polyion layer leads to overcompensation of surface charge. Therefore, the sign of net charge on the surface is inverted, and the subsequent deposition of an oppositely charged polyion becomes possible. In most cases, drying is performed after layer deposition. By repeating the process, dipping alternately in Beaker A and B with washing and drying in between, a multilayer assembly with the desired number of layers can be built up.

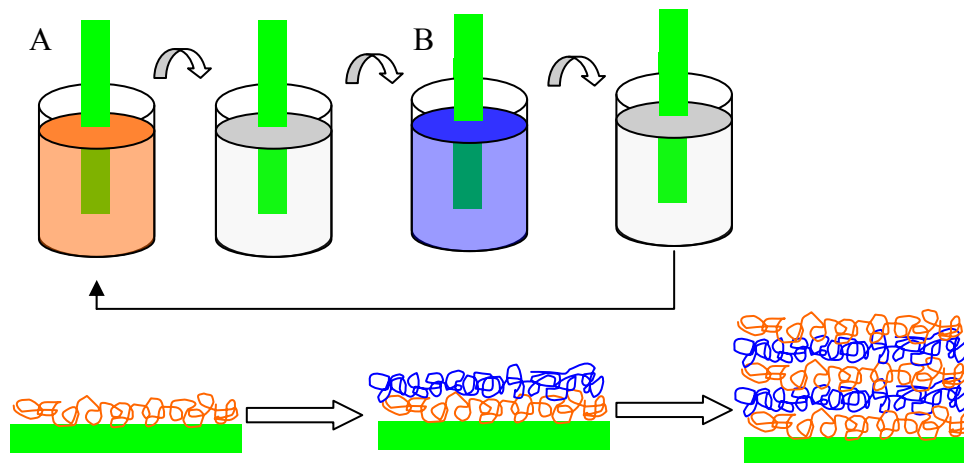


**Fig 1.13** Illustration of LBL assembly fabrication

There are many advantages using LBL assembly over other strategies for ultrathin film preparation such as the Langmuir-Blodgett (LB) technique and the self-assembled monolayer (SAM) method.<sup>45-49</sup> LB method suffers from the requirement of expensive instruments and is not applicable with many kinds of non-amphiphilic materials. SAM can

be built up on a wider range of materials; however, it can not form multilayers. Compared to these techniques, LBL stands out for the following reasons: (1) LBL is extremely cheap, no expensive instrument required. (2) The fabrication process is simple, and can be achieved either manually or by machine. (3) The film can form not only on planar substrates, but also on substrates with different shapes. The thickness increment per layer is self-regulating; similar surface roughness of LBL is expected regardless of the roughness of substrates. (4) LBL can incorporate different functional groups into the system for different applications. The applied materials include conventional polyelectrolytes as well as various functional polyelectrolytes. More interestingly, water-soluble biomaterials with charged sites on their surfaces can also be incorporated, such as proteins, DNA, and charged viruses. In addition, charged inorganic substances constitute another important part of LBL. Colloidal nanoparticles, clay, zeolite and polyoxometalates have been reported for use in LBL assembly. Charged supramolecular assemblies have also been incorporated into LBL assembly. A detailed citation involving the above function group can be found in the review by Katsuhiko.<sup>50</sup> Therefore, versatile materials can be used based on the application needs. The following will survey the recent advances in the field of LBL assembly involving POM and other functional groups.

#### ***1.3.3.2 LBL Assembly with Keggin Type Polyoxometalate***

Keggin structure is one of the famous structures in polyoxometalate. It shows good catalytic activity towards certain reactions such as hydration, polymerization and oxidation reaction. Several research groups have reported the combination of Keggin POM with other functional groups to build an LBL assembly. The corresponding properties as well as potential applications have been studied. Qian reports the

preparation of network composite films containing  $\text{H}_3\text{PMo}_{12}\text{O}_{40}$  and multi-walled carbon nanotubes (MWNTs) on glassy carbon substrate.<sup>51</sup> The film was fabricated by alternately dipping an electrode in POM and PDDA-MWNT solutions with deposition of a POM layer first. The prepared LBL-modified electrode was characterized by ESEM and electrochemistry. Interestingly, the plot of the second reduction peak current of PDDA-MWNTs/ $\text{PMo}_{12}$  electrode vs. the number of deposition cycles leads to a linear relationship; while for PDDA/ $\text{PMo}_{12}$  electrode, after two cycles the peak current begins to decrease compared to that of PDDA-MWNTs/ $\text{PMo}_{12}$  electrode and a curved plot is observed. The MWNTs/ $\text{PMo}_{12}$  electrode does not exhibit any current changes with increasing cycles indicating the failure of LBL assembly to form without pre charging MWNTs with PDDA. The superior performance of a PDDA-MWNTs/ $\text{PMo}_{12}$  electrode over a PDDA/ $\text{PMo}_{12}$  electrode was attributed to the function of MWNTs as “molecular wires”. In another study, Feng fabricated a LBL assembly using either  $\text{H}_4\text{SiW}_{12}\text{O}_{40}\cdot n\text{H}_2\text{O}$  or  $\text{H}_3\text{PMo}_{12}\text{O}_{40}\cdot n\text{H}_2\text{O}$  and chitosan.<sup>52</sup> The electrode was assembled with chitosan first and followed by the deposition of POM layer in acidic solution. The LBL was characterized by UV, XPS, AFM and electrochemistry. The antibacterial activity of the composite film against *E. coli* was also studied. Interestingly, the  $(\text{chitosan}/\alpha\text{-PMo}_{12})_n$  multilayer films exhibit antibacterial activity while the  $(\text{chitosan}/\alpha\text{-SiW}_{12})_n$  multilayer films do not. The antibacterial activity of  $(\text{chitosan}/\alpha\text{-PMo}_{12})_n$  film may be attributed to the oxidation of the cell membrane of the bacteria which inhibits bacteria’ growth. This is suggested by the blue color showing in the loop area around the  $(\text{chitosan}/\alpha\text{-PMo}_{12})_n$  multilayer films due to the reduction of  $\alpha\text{-PMo}_{12}$ . Yang reported a hybrid film containing  $\text{H}_4\text{SiW}_{12}\text{O}_{40}$  ( $\text{SiW}_{12}$ ) and 4-aminobenzo-15-crown- 5 ether (4-AB15C5) on both ITO

substrate and glassy carbon electrode.<sup>53</sup> The nanostructure of the film on ITO was found to be different from that of film on GCE. The former corresponds to a layer structure where 4-AB15C5 is horizontally orientated to ITO substrate, while the latter corresponds to an intercalation structure and 4-AB15C5 is vertical to GCE. Another study done by Glezos in which  $\text{H}_3\text{PW}_{12}\text{O}_{40}$  and 1,12-diaminododecane(DD,  $\text{H}_2\text{N}(\text{CH}_2)_{12}\text{NH}_2$ ) were built into a multilayer film, focused on the electron trapping behavior as well as the tunneling behavior of POM.<sup>54</sup>

### ***1.3.3.3 LBL Assembly with Wells Dawson Type Polyoxometalate***

The Wells Dawson structure is another well defined structure in polyoxometalate. It is a good catalyst towards many reactions such as reduction of oxygen, hydrogen peroxide, nitrite and bromate. Several groups reported the fabrication of bifunctional composite materials using the Wells Dawson compound and transition metal complexes. Kuhn and Anson prepared an LBL assembly containing  $\text{Os}(\text{bpy})_3^{2+}$ -  $\text{P}_2\text{Mo}_{18}\text{O}_{62}^{6-}$  on various electrode surfaces, including glassy carbon, highly ordered pyrolytic carbon, indium tin oxide, and gold-coated quartz.<sup>55</sup> The successful assembly involved the adsorption of a monolayer of  $\text{P}_2\text{Mo}_{18}\text{O}_{62}^{6-}$  followed by washing with water and one cycle of electrochemical treatment in the range of 0.3V to 0.8V in 0.5 M  $\text{NaHSO}_4$  solution. The coated electrode was then immersed in the solution containing 0.5~3 mM of either  $\text{Os}(\text{bpy})_3^{2+}$  or  $\text{Ru}(\text{bpy})_3^{2+}$  to adsorb another layer. In the preparation process, the identity of the electrode surface, the electrochemical treatment, and the PH of the deposition solution all affected the final composition of the film. The multilayer assembly was examined by electrochemistry, spectroelectrochemical and quartz crystal microgravimetric techniques. It was proven that the film is quite stable. Later, the same

group published the electrocatalysis results of these LBL assemblies towards  $\text{NO}_2^-$  reduction and benzyl alcohol oxidation. The catalytic activity of the coatings is attributed to the first POM layer in the multilayer assembly. Following their work, Fay reported a similar multilayer assembly on the GC electrode using Dawson heteropolyanion  $[\text{P}_2\text{W}_{18}\text{O}_{62}]^{6-}$  and  $[\text{Fe}(\text{bpy})_3]^{2+}$ .<sup>56</sup> The film prepared is both stable and reproducible. More than thirty monolayers can be coated on the surface of the electrode with good conductivity. In addition, the system exhibits better redox activity of the moieties deposited on the electrode surface compared to the system reported by Kuhn and Anson. The catalytic ability of the LBL assembly towards nitrite, bromate and hydrogen peroxide reduction was also studied. Besides transition metal bipy complexes, cationic phthalocyanine<sup>57</sup> and ruthenium metallodendrimer<sup>58</sup> were also incorporated into the LBL assembly with Dawson type polyoxometalate; their corresponding catalytic activities were reported. Other than commonly used ITO and GCE substrates, poly(vinyl alcohol) nanofiber modified ITO was employed as a substrate for PDDA/ $\text{P}_2\text{W}_{18}$  multilayer assembly.<sup>59</sup>

#### ***1.3.3.4 LBL Assembly with Wheel or Sphere Shaped Polyoxometalate***

As introduced in 1.3.2, wheel or sphere shaped POMs have many advantages due to their nanometer scale size, and a series of Mo-based wheel shaped POM have been reported to be incorporated into the LBL assembly such as  $(\text{NH}_4)_{42}[\text{Mo}_{132}\text{O}_{372}(\text{CH}_3\text{COO})_{30}(\text{H}_2\text{O})_{72}](\text{Mo}_{132})^{60}$ ,  $((\text{NH}_4)_{21}[\text{H}_3\text{Mo}_{57}\text{V}_6(\text{NO})_6\text{O}_{183}(\text{H}_2\text{O})_{18}]$   $(\text{Mo}_{57})^{61}$  and  $\text{Mo}_{36}$ .<sup>62</sup> The LBL was fabricated with the following steps: (1) A clean substrate was deposited with a layer of poly(ethylenimine) (PEI) (2) After washing, poly(styrenesulfonate) (PSS) and poly(allyamine hydrochloride) (PAH) were

successively deposited onto the PEI modified substrate. (3) POM of interest was then absorbed on the positively charged PAH. (4) The deposition of PAH and POM was repeated to achieve the desired number of layers. The LBL film was characterized using optical spectroscopy, AFM, QCM and small-angle X-ray reflectivity (XR). The surface density of  $(\{\text{Mo}_{132}\}/\text{PAH})_n$  was found to be  $(4.4\pm 0.2)\times 10^{12}$  clusters/cm<sup>2</sup> and that of  $(\{\text{Mo}_{57}\}/\text{PAH})_n$ ,  $(1.4\pm 0.4)\times 10^{13}$  clusters/cm<sup>2</sup> corresponding to an average surface coverage of 50% and  $56\pm 12\%$  respectively. The measured thickness for a  $(\{\text{Mo}_{132}\}/\text{PAH})$  layer pair is  $2.2\pm 0.2$  nm and  $0.8\pm 0.1$  nm for a  $(\{\text{Mo}_{57}\}/\text{PAH})$  layer pair. The LBL film density can be easily controlled by varying the polyelectrolyte-inter layer separation between each POM layer, and the total film thickness can be controlled by changing the number of layers deposited on the surface.

#### ***1.3.3.5 LBL Assembly with Preyssler Type Polyoxometalate***

Following the same fabrication strategy described in 1.3.3.4, the Preyssler-type POM  $(\text{NH}_4)_{14}[\text{NaP}_5\text{W}_{30}\text{O}_{110}]$  and poly(4-vinylpyridine)[P4VP] was incorporated into a self-assembled multilayer in Kurth's group for electro- and photochromic dual-mode devices.<sup>63</sup> P4VP serves as a proton reservoir which is needed for photochromic response. The film can change color from transparent to blue when exposed to a low-intensity UV lamp or electrochemically reduced under certain potential (below -0.2V). The blue color can be bleached by heating to 100 degree Celsius, irradiation with visible light, and applying potential at -0.2V. The combination of electro-and photochromism such as electro reduction followed by visible irradiation or UV irradiation followed by electro reoxidation also works. It was observed that the photo- and electroinduced switching gave different efficiencies. The overall performance of the device is reliable and fast. In



another study done by Nagaoka, Preyssler-type POM  $\text{NaP}_5\text{W}_{30}\text{O}_{110}$  was made into LBL assembly with PEI. The outmost PEI layer can be detached upon exposure to UV irradiation and then recovered by simply dipping into a PEI solution. Using this method, a photopatterned multilayer can be prepared by image-wise UV exposure with highly site-selective adsorption.<sup>64</sup>

#### ***1.3.3.6 LBL Assembly Using POM Stabilized Nanostructures***

Another type of LBL assembly involving POM is the use of POM to fabricate nanostructures such as nanoparticles or nanotubes and then to assemble the POM modified nanostructure into an LBL system. Kulesza reported the fabrication of LBL assemblies containing phosphododecamolybdate ( $\text{PMo}_{12}\text{O}_{40}^{3-}$ ) stabilized Pt nanoparticles and positively charged conducting polymers such as polyaniline (PANI), polypyrrole (PPy) or poly(3,4-ethylenedioxythiophene), PEDOT.<sup>65</sup> Pt- $\text{PMo}_{12}$  was prepared by suspending Pt black in  $\text{PMo}_{12}\text{O}_{40}^{3-}$  solution and sonicating for 2 hours. The prepared nanoparticle was about 7 nm in diameter and was used to build an LBL assembly. The general procedure involved the deposition of a layer of Pt- $\text{PMo}_{12}$  followed by absorption of a layer of monomer ion such as Anilinium, and then electropolymerization of the monomer into a thin layer by potential cycling at a certain range. The surface coverage of  $\text{PMo}_{12}$  based on the second cathodic peak was about  $2 \times 10^{-10}$  mol  $\text{cm}^{-2}$ . They also try to study the dynamics of charge transfer using potential step experiment. The calculated diffusion coefficient of the first positive redox reaction in the hybrid film was around  $1 \sim 2 \times 10^{-8}$   $\text{cm}^2\text{s}^{-1}$  based on the estimated concentration of  $\text{PMo}_{12}$  redox center which was about  $0.6 \sim 0.8$  mol  $\cdot \text{dm}^{-3}$ . The catalytic activity of this hybrid film was measured toward the reduction of nitrite, bromate and dioxygen. The dioxygen reduction with the hybrid

film showed a negative shift compared to that of a monolayer (Pt-PMo<sub>12</sub>) modified GC electrode indicating an inhibiting of the aniline monomer. In another similar study, they substituted PMo<sub>12</sub> with PW<sub>12</sub> and followed the same strategy to build the hybrid film.<sup>66</sup> The size of the PW<sub>12</sub> stabilized Pt nanoparticle is about 5~10 nm. The dioxygen reduction of the hybrid film showed similar behavior in that less potential was observed than monolayer Pt-PW<sub>12</sub> modified electrode. The inhibition effect of the hybrid material on oxygen reduction is not quite clear so far. The study also shows that in the presence of PW<sub>12</sub>, a large amount of Pt nanoparticles can be immobilized on the electrode surface while PW<sub>12</sub>- free Pt nanoparticles tend to be washed off the electrode. More recent work in this area is to build LBL assemblies with conducting polymer PEDOT or polyaniline and PMo<sub>12</sub> stabilized carbon nanostructures such as carbon nanoparticles (CNPs) or carbon nanotubes (CNTs).<sup>67, 68</sup> The CNPs show smaller size after being modified with PMo<sub>12</sub> (30~50 nm) than before modification (80-100 nm), while most CNTs increase the diameter from 9-10 nm to 11-12 nm after PMo<sub>12</sub> treatment. The increased size of the CNTs is attributed to the attached PMo<sub>12</sub>. The prepared hybrid film is of potential utility in the construction of supercapacitors.

#### ***1.3.3.7 LBL Assembly with Other Type Polyoxometalate***

In addition to the above mentioned POMs, other types of POM and POM derivatives have also been reported incorporated into LBL films. Dong used a mixed-addenda polyoxometalate K<sub>10</sub>H<sub>3</sub>[Eu(SiMo<sub>9</sub>W<sub>2</sub>O<sub>39</sub>)<sub>2</sub>] to form an LBL assembly with Ru(bpy)<sub>3</sub><sup>2+</sup>.<sup>69</sup> The hybrid film {PEI/[EuSiMo<sub>9</sub>W<sub>2</sub>/Ru(bpy)<sub>3</sub>]<sub>n</sub>} showed five characteristic peaks in the emission spectra. Also the film exhibited remarkable catalytic activities towards the reduction of IO<sub>3</sub><sup>-</sup>, H<sub>2</sub>O<sub>2</sub>, BrO<sub>3</sub><sup>-</sup> and NO<sub>2</sub><sup>-</sup> which are due to the function of

POM, as well as the oxidation of  $C_2O_4^{2-}$  which is due to the function of  $Ru(bpy)_3^{2+}$ . Gao prepared an LBL assembly containing POM ( $BW_{12}O_{40}^{5-}$ ,  $Co_4(H_2O)_2(PW_9O_{34})_2^{10-}$ ) and phendione transition metal complexes  $[M(\text{phendione})_3]^{2+}$  ( $M = Fe^{2+}$ ,  $Co^{2+}$ , phendione = 1,10-phenanthroline-5,6-dione).<sup>70</sup> Further examples include nickel-substituted Dawson-type polyoxometalate hybrid  $(P_2W_{17}Ni/PAH)_n$ <sup>71</sup>, sandwich-type polyoxometalate based film  $(Sb_2W_{20}Fe_2/PDDA)_n$ <sup>72</sup>. In this study, cobalt- or Ruthenium-substituted dawson type polyoxometalates was used to fabricate LBL assembly; more detailed information can be found in Chapter V.

#### 1.4 Conclusions

In summary, supramolecular assemblies generate a facile synthesis strategy to construct mesostructure in a long range order and display important functions such as molecular recognition, sensing, ion transport and catalysis. Further work on superamolecular assemblies will yield more functional materials displaying extraordinary photonic and electronic properties.

#### 1.5 References

1. Slone, R. V.; Hupp, J. T.; Stern, C. L.; Albrecht-Schmitt, T. E., *Inorg. Chem.* **1996**, 35, 4096-4097.
2. Sun, S.-S.; Lees, A. J., *Coord. Chem. Rev.* **2002**, 230, 171-192.
3. Sun, S.-S.; Lees, A. J., *J. Am. Chem. Soc.* **2000**, 122, 8956-8967.
4. Slone, R. V.; Hupp, J. T., *Inorg. Chem.* **1997**, 36, 5422-5423.
5. Belanger, S.; Hupp, J. T.; Stern, C. L.; Slone, R. V.; Watson, D. F.; Carrell, T. G., *J. Am. Chem. Soc.* **1999**, 121, 557-563.
6. Ferrer, M.; Rodriguez, L.; Rossell, O., *J. Organomet. Chem.* **2003**, 681, 158-166.

7. Ferrer, M.; Mounir, M.; Rossell, O.; Ruiz, E.; Maestro, M. A., *Inorg. Chem.* **2003**, 42, 5890-5899.
8. Ferrer, M.; Gutierrez, A.; Mounir, M.; Rossell, O.; Ruiz, E.; Rang, A.; Engeser, M., *Inorg. Chem.* **2007**, 46, 3395-3406.
9. Lee, S. J.; Lin, W., *Acc. Chem. Res.* **2007**, 41, (4), 521-537.
10. Zhang, L.; Niu, Y.-H.; Jen, A. K.-Y.; Lin, W., *Chem. Commun.* **2004**, 8, 1002–1004.
11. Lee, S. J.; Lin, W., *J. Am. Chem. Soc.* **2002**, 124, 4554-4555.
12. Drain, C. M.; Lehn, J.-M., *J. Chem. Soc., Chem. Commun.* **1994**, 2313-2315.
13. Lee, S. J.; Hupp, J. T., *Coord. Chem. Rev.* **2006**, 250, 1710-1723.
14. Maeda, C.; Kamada, T.; Aratani, N.; Osuka, A., *Coord. Chem. Rev.* **2007**, 252, 2743-2752.
15. Splan, K. E.; Massari, A. M.; Hupp, J. T., *J. Phys. Chem. B* **2004**, 108, 4111-4115.
16. Yatskou, M. M.; Koehorst, R. B. M.; Donker, H.; Schaafsma, T. J., *J. Phys. Chem. A* **2001**, 105, 11425-11431.
17. Yatskou, M. M.; Koehorst, R. B. M.; Hoek, A. v.; Donker, H.; Schaafsma, T. J., *J. Phys. Chem. A* **2001**, 105, 11432-11440.
18. Kelley, R. F.; Goldsmith, R. H.; Wasielewski, M. R., *J. Am. Chem. Soc.* **2007**, 129, 6384-6385.
19. Hasenknopf, B., *Front. Biosci.* **2005**, 10, 275-287.
20. Contant, R.; Teze, A., *Inorg. Chem.* **1985**, 24, 4610-4614.
21. Mal, S. S.; Kortz, U., *Angew. Chem. Int. Ed.* **2005**, 44, 3777-3780.

22. Jabbour, D.; Keita, B.; Nadjo, L.; Kortz, U.; Mal, S. S., *Electrochem. Commun.* **2005**, 7, 841-847.
23. Liu, G.; Liu, T.; Mal, S. S.; Kortz, U., *J. Am. Chem. Soc.* **2006**, 128, 10103-10110.
24. Müller, A.; Kogerler, P.; Dress, A. W. M., *Coord. Chem. Rev.* **2001**, 222, 193-218.
25. Müller, A.; Serain, C., *Acc. Chem. Res.* **2000**, 33, 2-10.
26. Cronin, L.; Beugholt, C.; Müller, A., *J. Mol. Struct.* **2000**, 500, 181-193.
27. Long, D.-L.; Burkholder, E.; Cronin, L., *Chem. Soc. Rev.* **2007**, 36, 105-121.
28. Müller, A.; Krickemeyer, E.; Bögge, H.; Schmidtman, M.; Peters, F., *Angew. Chem. Int. Ed.* **1998**, 37, (24), 3360-3363.
29. Müller, A.; Sarkar, S.; Shah, S. Q. N.; Bogge, H.; Schmidtman, M.; Sarkar, S.; Kogerler, P.; Hauptfleisch, B.; Trautwein, A. X.; Schunemann, V., *Angew. Chem. Int. Ed.* **1999**, 38, (21), 3238-3241.
30. Müller, A.; Botar, B.; Bogge, H.; Kogerler, P.; Berkle, A., *Chem. Commun.* **2002**, 2944-2945.
31. Müller, A.; Das, S. K.; Kogerler, P.; Bogge, H.; Schmidtman, M.; Trautwein, A. X.; Schunemann, V.; Krickemeyer, E.; Preetz, W., *Angew. Chem. Int. Ed. Engl.* **2000**, 39, 3414.
32. Müller, A.; Rehder, D.; K., E. T.; Haupt, A. M.; Bogge, H.; Schmidtman, M.; Heinze-Bruckner, G., *Angew. Chem. Int. Ed.* **2004**, 43, 4466–4470.
33. Müller, A.; Zhou, Y.; Bogge, H.; Schmidtman, M.; Mitra, T.; Haupt, E. T. K.; Berkle, A., *Angew. Chem. Int. Ed.* **2006**, 45, 460-465.
34. Müller, A.; Toma, L.; Bogge, H.; Schaffer, C.; Stammler, A., *Angew. Chem. Int. Ed.* **2005**, 44, 7757-7761.

35. Cronin, L.; Beugholt, C.; Krickemeyer, E.; Schmidtman, M.; Bogge, H.; Kogerler, P.; Luong, T. K. K.; Müller, A., *Angew. Chem. Int. Ed.* **2002**, 41, (15), 2805-2808.
36. Müller, A.; Beckmann, E.; Bogge, H.; Schmidtman, M.; Dress, A., *Angew. Chem., Int. Ed.* **2002**, 41, (7), 1162-1167.
37. Cadot, E.; Secheresse, F., *Chem. Commun. (Cambridge, U. K.)* **2002**, (19), 2189-2197.
38. Secheresse, F.; Dolbecq, A.; Mialane, P.; Cadot, E., *C. R. Chim.* **2005**, 8, (11-12), 1927-1938.
39. Cadot, E.; Salignac, B.; Halut, S.; Secheresse, F., *Angew. Chem., Int. Ed.* **1998**, 37, (5), 611-612.
40. Iler, R. K., *J. Colloid Interface Sci.* **1966**, 21, 569.
41. Decher, G.; Hong, J. D., *Makromol. Chem., Macromol. Symp* **1991**, 46, 321.
42. Decher, G.; Hong, J. D., *Ber. Bunsen-Ges. Phys. Chem* **1991**, 95, 1430.
43. Decher, G., *Science* **1997**, 277, 1232-1237.
44. Zhang, X.; Chen, H.; Zhang, H., *Chem. Commun.* **2007**, 1395-1405.
45. Love, J. C.; Estroff, L. A.; Kriebel, J. K.; Nuzzo, R. G.; Whitesides, G. M., *Chem. Rev.* **2005**, 105, 1103.
46. Dubois, L. H.; Nuzzo, R. G., *Annu. Rev. Phys. Chem.* **1992**, 43, 437.
47. Ulman, A., *Chem. Rev.* **1996**, 96, 1533.
48. Maoz, R.; Frydman, E.; Cohen, S. R.; Sagiv, J., *Adv. Mater.* **2000**, 12, 424.
49. Ginger, D. S.; Zhang, H.; Mirkin, C. A., *Angew. Chem., Int. Ed.* **2004**, 43, 30.
50. Ariga, K.; Hill, J. P.; Ji, Q., *Phys. Chem. Chem. Phys.* **2007**, 9, 2319-2340.

51. Qian, L.; Yang, X., *Electrochem. Commun.* **2005**, 7, 547-551.
52. Feng, Y.; Han, Z.; Peng, J.; Lu, J.; Xue, B.; Li, L.; Ma, H.; Wang, E., *Mater. Lett.* **2006**, 60, 1588–1593.
53. Yang, G.; Guo, H.; Wang, M.; Huang, M.; Chen, H.; Liu, B.; Dong, S., *J. Electroanal. Chem.* **2007**, 600, 318-324.
54. Glezos, N.; Douvas, A. M.; Argitis, P.; Saurenbach, F.; Chrost, J.; Livitsanos, C., *Microelectron. Eng.* **2006**, 83, 1757–1760.
55. Kuhn, A.; Anson, F. C., *Langmuir* **1996**, 12, 5481-5488.
56. Fay, N.; Dempsey, E.; McCormac, T., *J. Electroanal. Chem.* **2005**, 574, 359-366.
57. Jin, Y.; Xu, L.; Zhu, L.; An, W.; Gao, G., *Thin Solid Films* **2007**, 515, 5490-5497.
58. Cheng, L.; Cox, J. A., *Chem. Mater.* **2002**, 14, 6-8.
59. Shan, Y.; Yang, G.; Sun, Y.; Pang, S.; Gong, J.; Su, Z.; Qu, L., *Electrochim. Acta* **2007**, 53, 569–574.
60. Kurth, D. G.; Volkmer, D.; Ruttorf, M.; Richter, B.; Müller, A., *Chem. Mater.* **2000**, 12, 2829-2831.
61. Caruso, F.; Kurth, D. G.; Volkmer, D.; Koop, M. J.; Muller, A., *Langmuir* **1998**, 14, 3462-3465.
62. Wang, L.; Jiang, M.; Wang, E. B.; Liana, S. Y.; Xua, L.; Li, Z., *Mater. Lett.* **2004**, 58, 683-687.
63. Liu, S.; Mohwald, H.; Volkmer, D.; Kurth, D. G., *Langmuir* **2006**, 22, 1949-1951.
64. Nagaoka, Y.; Shiratori, S.; Einaga, Y., *Chem. Mater.* **2008**, 20, (12), 4004-4010.

65. Karnicka, K.; Chojak, M.; Miecznikowski, K.; Skunik, M.; Baranowska, B.; Kolary, A.; Piranska, A.; Palys, B.; Adamczyk, L.; Kulesza, P. J., *Bioelectrochemistry* **2005**, 66, 79-87.
66. Kulesza, P. J.; Karnicka, K.; Miecznikowski, K.; Chojak, M.; Kolary, A.; Barczuk, P. J.; Tsirlina, G.; Czerwinski, W., *Electrochim. Acta* **2005**, 50, 5155-5162.
67. Kulesza, P. J.; Skunik, M.; Baranowska, B.; Miecznikowski, K.; Chojak, M.; Karnicka, K.; Frackowiak, E.; Beguin, F.; Kuhn, A.; Delville, M.-H.; Starobrzynska, B.; Ernst, A., *Electrochim. Acta* **2006**, 51, 2373-2379.
68. Skunik, M.; Baranowska, B.; Fattakhova, D.; Miecznikowski, K.; Chojak, M.; Kuhn, A.; Kulesza, P. J., *J. Solid State Electrochem.* **2006**, 10, 168-175.
69. Dong, T.; Ma, H.; Zhang, W.; Gong, L.; Wang, F.; Li, C., *J. Colloid Interface Sci.* **2007**, 311, 523-529.
70. Gao, S.; Lia, X.; Yang, C.; Lia, T.; Cao, R., *J. Solid State Chem.* **2006**, 179, 1407-1414.
71. Gao, G.; Xu, L.; Wang, W.; Wang, Z.; Qiu, Y.; Wang, E., *J. Electrochem. Soc.* **2005**, 152, (7), H102-H106.
72. Bi, L.-H.; McCormac, T.; Beloshapkin, S.; Dempsey, E., *Electroanalysis* 20, (1), 38-46.



## CHAPTER TWO

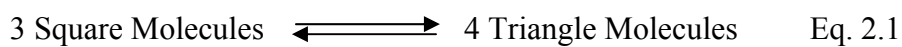
### SYNTHESIS AND CHARACTERIZATION OF RUTHENIUM (II) MOLECULAR SQUARES, AND TRIANGLE-SQUARE EQUILIBRIUM STUDIES

#### 2.1 Introduction

Transition-metal-directed self-assembly has gained wide attention in recent years. Following the pioneering work done by Fujita<sup>1,2</sup> and Stang<sup>3</sup> in the 1990s, different shape metallocycles such as squares,<sup>4, 5</sup> rectangles,<sup>6</sup> triangles,<sup>7-9</sup> helices,<sup>10</sup> boxes and frameworks<sup>11-13</sup> have been synthesized. Among these self-assembled supramolecules, molecular squares with metallo-corners of  $\sim 90^\circ$  angles and linear bidentate bridging ligand has been extensively studied. There are many significant features of this type of molecule: (1) Flexible design: molecular squares with different properties can be obtained by changing either metal corner ions or bridging ligand. (2) Tunable porosity: the size of the internal porosity of squares can be tuned by using linkers with variable length. (3) Highly ordered structures in crystal phase: molecular squares tend to form one dimensional channels through their cavity sites.<sup>14</sup> (4) Special optical properties: molecular squares such as porphyrine containing metallo squares exhibit strong fluorescence and fast energy transfer.<sup>15</sup> (5) Enantioselectivity and catalytic activity.<sup>16</sup>

The synthesis of molecular squares is controlled by thermodynamics; however, triangles can be isolated as kinetic products under circumstances. In general, molecular

squares are less strained and therefore more stable in terms of enthalpy, while entropic factors favor the triangles since their assembly uses fewer components. Previous study showed that most Pt- or Pd- based metal corners formed mixtures of squares and triangles. Both species are in equilibrium with each other shown in equation 2.1, and this equilibrium is concentration dependant: at higher concentration, the equilibrium favors squares according to Le Chatelier's Law. Many factors such as the rigidity of the building blocks, the value of the angle of the adjacent coordination sites, and the lability of the metal-pyridine bond will all affect the self-assembly process. For example, with  $[\text{Pb}(\text{NO}_3)_2(\text{en})]$  as a metal corner, molecular squares form by using 4,4'-bipyridine. Longer ligands result in a mixture of squares and triangles; if the ethylenediamine group on palladium is replaced with the more sterically demanding 2,2'-bipyridine, a mixture of square and triangles will form even with 4,4'-bipyridine. Much effort has been put forth towards better understanding the equilibrium process: Ferrer designed a series of metal corners with different steric factors to study the effect. Meanwhile the ligand effect can be obtained from metallocycles with the same metal corner but a different bridging ligand. In addition, more techniques have been developed for studying the equilibrium, such as solution phase X-ray diffraction,<sup>17</sup> Diffusion NMR,<sup>18</sup> Gel Permeation Chromatography,<sup>19</sup> and computer modeling.<sup>9</sup> However, there is as yet no straightforward way to predict the composition of the equilibrium (squares or triangles). To the best of our knowledge, such equilibrium has not been observed in other transition metal such as rhenium, rhodium, and iridium based systems in which only single products, either squares or triangles, can be produced.



In this study, we extended our scope to synthesize Ruthenium (II)- based metallo complexes with bridging ligands of 4,4'-Azodipyridine(AZP), 4,4'-(1,3-butadiyne-1,4-diyl)bis-Pyridine(DPB) and 3,6-di-4-pyridinyl-1,2,4,5-Tetrazine(dipyTz). This was prompted by a previous study done by S. L. Queiroz in which a series of molecular squares containing diphosphine Ruthenium (II) corners and bridging ligands of pyrazine (pz), 4,4'-bipyridine (4,4'-bipy), 1,2-bis-trans-(4-pyridyl)ethane (pieta), and 1,2-bis-trans-(4-pyridyl)ethylene (pyetil) were synthesized and characterized. For comparison purposes, pz and 4,4'-bipy based molecular squares were also synthesized. The molecular structures of all the ligands used in this study are listed in Figure 2.1. Our interest in this ruthenium diphosphine system is not only out of curiosity of whether equilibrium (squares and triangles) exists in such a system when using longer and more basic bridging ligands, but also the octahedral coordination center which provides opportunities to build more complicated structures by replacing the two chlorides with functional ligands. Some potential applications of these supramolecules have also been explored.

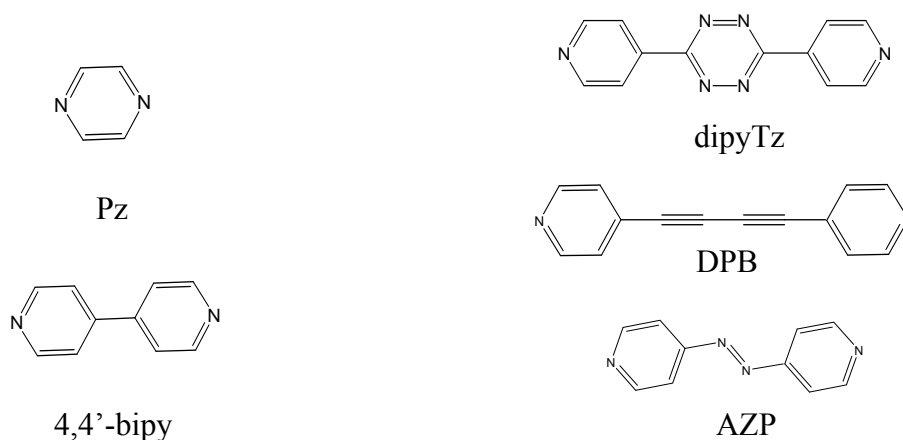


**Figure 2.1** Molecular structures of bridging ligands of this study

## 2.2 Experimental

### 2.2.1 Chemicals and reagents

Dichlorotris (triphenyl-phosphine) ruthenium (II) (97%), 4,4-dipyridyl(BP) (98%), 1,4-Bis(diphenyl-phosphino) butane(dppb) (98%), Pyrazine(Pz) ( $\geq 99\%$ ), 4,4'-Azodipyridine(AZP), Chloroform-*d* (99.8 atom%D), Silver tetrafluoroborate (98%) were purchased from Sigma-Aldrich; 3,6-di-4-pyridinyl-1,2,4,5-Tetrazine(dipyTz), 4,4'-(1,3-butadiyne-1,4-diyl)bis-Pyridine(DPB) (milligram quantities) were purchased from the Florida Center for Heterocyclic Compounds, Department of Chemistry, University of Florida; Tetrabutylammonium perchlorate (98%) and  $\beta$ -Cyclodextrin were purchased from Fluka. Solvents including benzene, diethyl ether, hexane, acetone and dichloromethane and chloroform were purchased from Fisher Scientific. Tetrabutylammonium perchlorate was recrystallized from ethanol–water and dried overnight under vacuum before use. Solvents were dried and distilled following the proper procedure in continuous stills using either calcium hydride or self-indicating sodium/benzophenone and stored over 4Å molecular sieves. Purified and dried argon or nitrogen (passing the gas through silica gel desiccant) was used to remove the dissolved oxygen in all the procedures.

### 2.2.2 Apparatus

*UV–vis Measurements:* UV-vis spectra were collected on a Shimadzu UV-3600 UV–vis-near infrared (UV–vis-NIR) spectrophotometer.

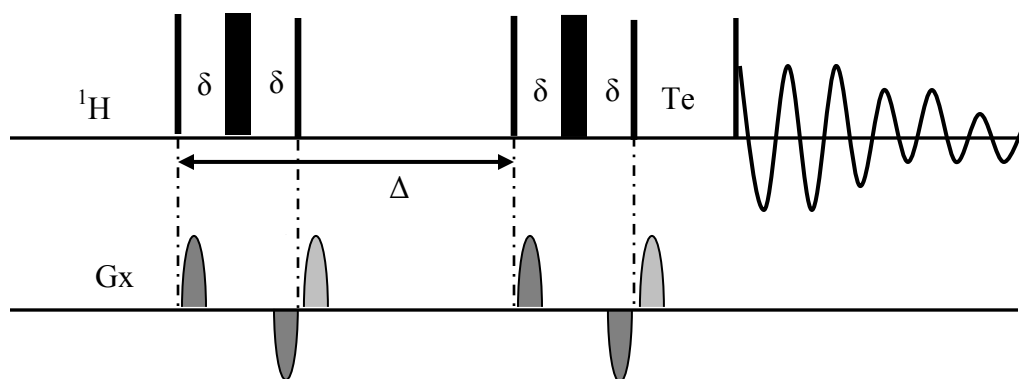
*Electrochemistry Measurements:* All the measurements were performed in freshly distilled dichloromethane solvent containing 0.1M tetrabutylammonium perchlorate electrolyte (TBAP). Cyclic voltammograms and controlled potential electrolysis were

measured using a three-electrode one-compartment cell and a three electrode two-compartment cell equipped with a glassy carbon working electrode (3mm in diameter) and a platinum counter-electrode respectively. The reference electrode used was Ag | AgCl with salt in a Luggin capillary, 0.1 M TBAP in CH<sub>2</sub>Cl<sub>2</sub>. Epsilon Potentiostat from BASi was employed.

*Raman Measurements:* Raman spectra were collected with Renishaw inVia Raman Microscope using 785 nm laser excitation for 10s exposure at 0.05% output power.

*NMR Measurements:* <sup>1</sup>H and <sup>13</sup>C NMR spectra were recorded on a Bruker AC 400 Spectrometer. All <sup>1</sup>H chemical shifts were reported in δ relative to the internal standard tetramethylsilane (TMS, δ=0.00) The spin multiplicities were indicated by the symbols “s” (singlet), “d” (doublet), “t” (triplet), “q” (quartet), “m” (multiplet) and “br” (broad).

PFG-NMR was collected using the ledbpgp2s1d pulse program shown below in Scheme 2.1. The coil constant, 369 G·s<sup>-1</sup> was calibrated with β-cyclodextrin in D<sub>2</sub>O which has a diffusion coefficient of 3.332×10<sup>-6</sup> cm<sup>2</sup>/s. The difference in solvent viscosity was based on the reported value. All <sup>1</sup>H free induction decay (FIDs) were acquired at around 294 K. The experimental parameters were set as follows: relaxation delay (1 s), diffusion delay Δ (0.2 s), gradient pulse duration δ (1 ms), delay between gradient pulses τ (0.1 ms), eddy current delay time T<sub>e</sub> (50 ms). The gradient ratios, gpz6, were varied from 1-100 while gpz7 and gpz8 were set -17.13 and -13.17 respectively. All the spectra were collected with incremented gradient amplitude values.



**Scheme 2.1** The pulse diagram of ledbpgp2s1d.

### 2.2.3 Synthesis Procedures

*Synthesis of  $[RuCl_2(dppb)]_2(\mu-dppb)$ :* Complex  $RuCl_2(PPh_3)_3$  (0.1 g, 0.1043 mmol) was stirred with 2 equivalent of dppb (0.089 g, 0.2086 mmol) in  $C_6H_6$  (25 ml) for one hour at room temperature under argon. The resulting green solution was reduced in volume to around 5 ml, and hexane (20 ml) was added to precipitate a mustard solid. The mustard product was collected by filtration, washed with hexanes ( $4 \times 10$  ml), and dried under vacuum.

*Synthesis of  $\{[RuCl_2(dppb)](\mu-N-N)\}_n$  ( $n=3$  or  $4$ ):* The synthesis followed the procedure of reference.<sup>20</sup>  $[RuCl_2(dppb)]_2(\mu-dppb)$  (0.200 g; 0.123 mmol) was dissolved in benzene (8 ml), and about 2 equivalent amount of bridging ligand (BP, Pz, AZP, DPB, dipyTz) was added to produce a colored solution. This solution was stirred at room temperature for 30 min after which its volume was reduced to approximately 1 ml, and then diethyl ether was added to precipitate a solid. The product was collected by filtration, washed well with diethyl ether and dried under vacuum.

## 2.3 Results and Discussion

### 2.3.1 Synthesis

The synthetic route for  $\{[\text{RuCl}_2(\text{dppb})](\mu\text{-N-N})\}_n$  is shown in Figure 2.2. In the first step, all the triphenyl-phosphine groups are substituted by dppb that result in the formation of a dimer  $[\text{RuCl}_2(\text{dppb})]_2(\mu\text{-dppb})$  with two dppb molecules capping a corner of each ruthenium and one linking the two ruthenium atoms together.  $[\text{RuCl}_2(\text{dppb})]_2(\mu\text{-dppb})$  has low or zero solubility in aromatic or non-aromatic solvents; however it is very useful precursor for preparation of mono- and dinuclear complexes containing the 'RuCl<sub>2</sub>(dppb)' moiety such as RuCl<sub>2</sub>(dppb)-(L)<sub>2</sub> and  $\{[\text{RuCl}_2(\text{dppb})](\mu\text{-N-N})\}_n$ . In the second step, bridging ligands are added to the precursor solution to form cyclic structures. The mole ratio of the bridging ligand to the precursor is around 2:1. Access of bridging ligands does not affect the reaction except for pyrazine which requires control of the mole ratio.

### 2.3.2 UV-Vis Spectra

An indication that the reaction is occurring is the color change of the solution; therefore UV-vis spectra can be used to monitor the coordination process. For example DPB solution is colorless and there is no absorption in the visible region; however after reacting with precursor, a broad absorption peak at 419 nm can be observed in agreement with the resulting red color solution; AZP solution which is in red color becomes purple after complexation and dipyTz solution changes from pink to brown after reaction. The UV-Vis spectra of DPB, AZP and dipyTz as well as their corresponding complexes are recorded and shown in Figure 2.3. Their adsorption wavelength is summarized in Table 2.1 as well. Intense absorptions below 325 nm present in the free ligands and complexes

are assigned to  $\pi \rightarrow \pi^*$  transitions from the aromatic rings. Small absorptions in the visible range for AZP and dipyTz are also assigned to  $\pi \rightarrow \pi^*$  transitions. Moderately intense absorption peaks observed in the complexes are assigned to charge transfer ( $\text{Ru(II)}d\pi \rightarrow \text{py}\pi^*$ ). As explained by Salet L. Queiroz, the d-d transitions of the metal ions are obscured by the broad peak of charge transfer at lower energies. For reference, the UV-Vis spectra of BP and Pz based complexes are also recorded, and the  $\lambda_{\text{max}}$  values are in agreement with the reported values.<sup>20</sup>

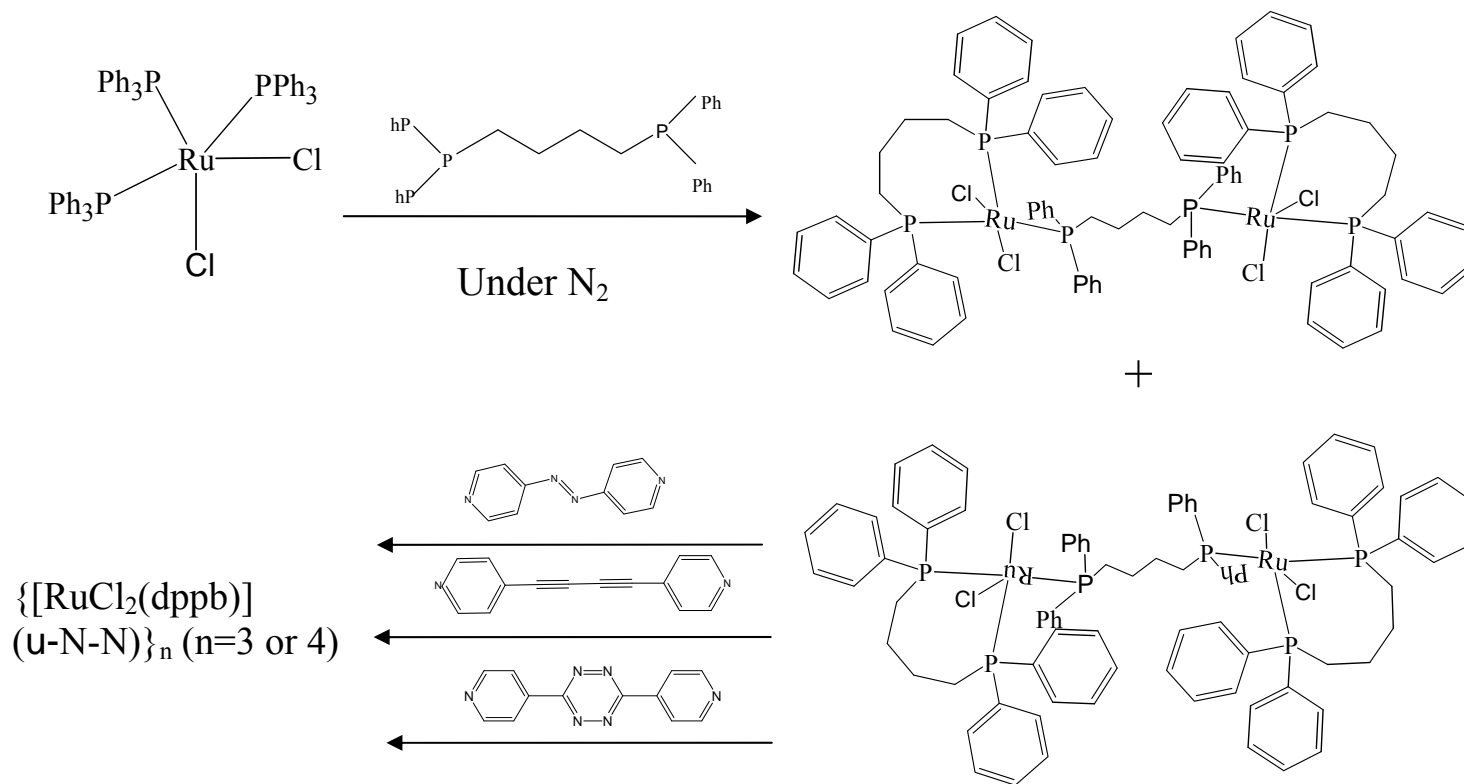
**Table 2.1** UV-Vis Absorption of  $\{[\text{RuCl}_2(\text{dppb})](\mu\text{-N-N})\}_n$

Compounds	Absorption Spectra $\lambda_{\text{max}}$ , nm
AZP bridged complex*	227,275,497(br)
DPB bridged complex *	289,308,329,419(br)
dipyTz bridged complex <sup>#</sup>	227,273,464(br)
AZP <sup>21</sup> *	287,458
DPB <sup>22</sup> *	245,256,285,304,325
dipyTz <sup>#</sup>	271,544

\* Spectra were taken in  $\text{CH}_2\text{Cl}_2$  solution. # Spectra were taken in  $\text{CHCl}_3$  solution. (br) broad



**Figure 2.2** Synthetic route for  $\{[\text{RuCl}_2(\text{dppb})](\mu\text{-N-N})\}_n$



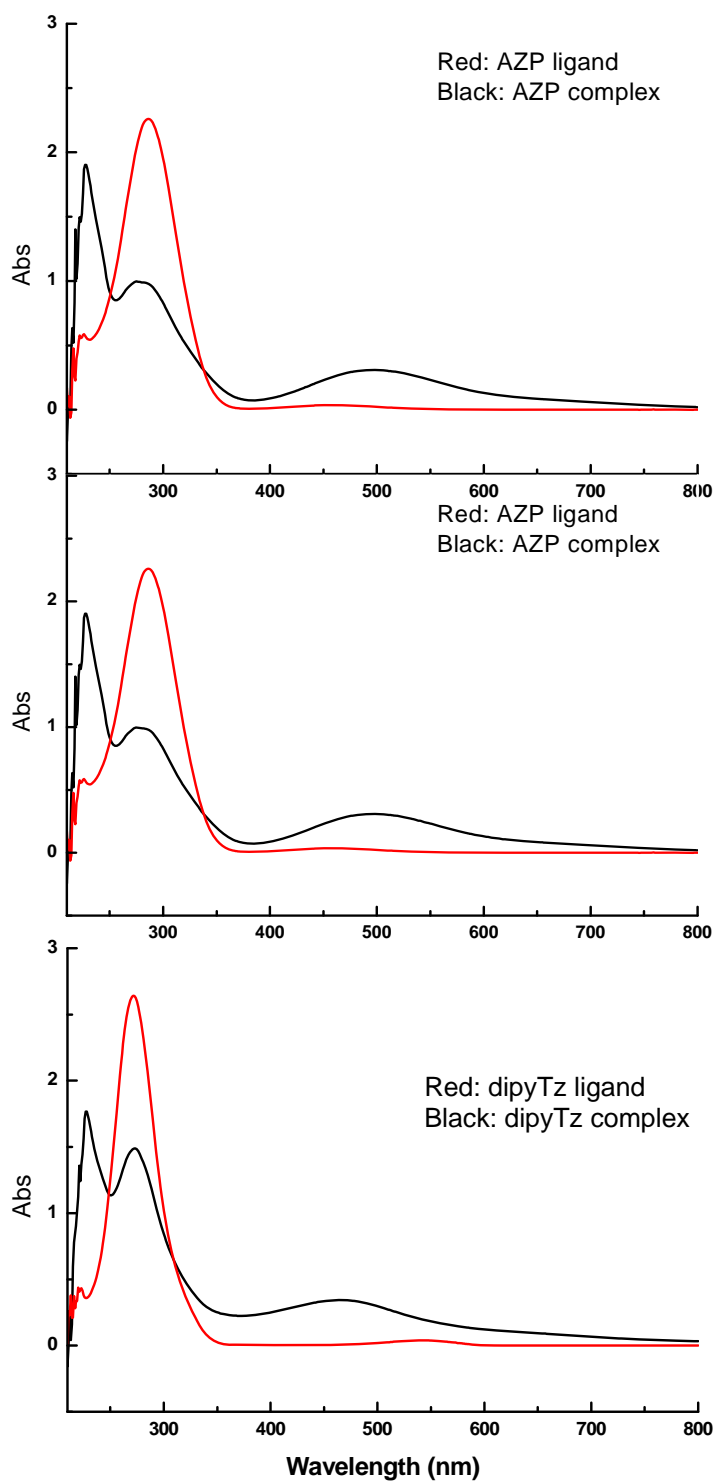


**Figure 2.3** UV – Vis Spectra of DPB ligand and DPB complex in CH<sub>2</sub>Cl<sub>2</sub>(top); AZP and AZP complex in CH<sub>2</sub>Cl<sub>2</sub>(middle) ; dipyTz and dipyTz complex in CHCl<sub>3</sub>(bottom)

### 2.3.3 Raman Spectra

Since the synthesized compounds have good symmetry, they are both IR and Raman active; however the signal to noise ratio of IR spectra collected is not good. In contrast, the Raman spectra (Figure 2.4 to Figure 2.8) display well defined peaks and are shown below. Peaks in the range of 500~2000  $\text{cm}^{-1}$  are mainly from the bridging ligand and the complete assignments of those peaks are summarized in Table 2.2. It is interesting to see some shifts of certain vibrational wave numbers of the coordinated pyridines compared to those of free molecules. For example, the vibration of BP at 1620, 1219, 759  $\text{cm}^{-1}$  shifts to 1612, 1230, 777  $\text{cm}^{-1}$  respectively, and the peak intensity at 1073 and 1021 increases after coordination with Ruthenium. The vibration of Pz at 1580, 1016, 602  $\text{cm}^{-1}$  shifts to 1594, 1026, 644  $\text{cm}^{-1}$  after coordination. Similar upward shifts in wave numbers after coordination were also observed for DPB and dipyTz; however a downward shift occurred for AZP which may have been caused by running the two samples under different conditions (the AZP data was cited from reference<sup>23</sup>). All these observations are consistent with previously study that the coupling between the pyridine and the low wave number vibrations of metal, particularly, the M-N stretching mode causes the upward shifts of certain vibrational wave numbers.<sup>24</sup> Vibrations below 500  $\text{cm}^{-1}$  are observed for some of the bridging ligand (some show strong fluorescence which block the vibration peaks at this region) and the coordination compound. Figure 2.9 shows the comparison of the vibration spectra of AZP complex, dipyTz complex and DPB complex in the region of 100~500  $\text{cm}^{-1}$ . All of them show similar patterns except that the AZP complex does not show the peak at 293  $\text{cm}^{-1}$ . The vibrations in this region can provide useful information for determining the cis or trans structure. Previous work

indicated that in octahedral  $ML_4Cl_2$ , if only one  $\nu(Ru-Cl)$  peak shows up then the two chlorides are in trans configuration. If two  $\nu(Ru-Cl)$  peaks appear, then the two chlorides are in cis position.<sup>25</sup> Based on the study done by Bandeira<sup>26</sup>, the peaks at  $260\text{ cm}^{-1}$  and  $293\text{ cm}^{-1}$  can be assigned to  $\nu(Ru-N)$ , giving the possibilities of  $\nu(Ru-Cl)$  at either  $211\text{ cm}^{-1}$  or  $420\text{ cm}^{-1}$ . In both cases, only singlet was observed indicating the two chlorides are in trans position. This would be useful information for determining the structure of these coordination compounds.

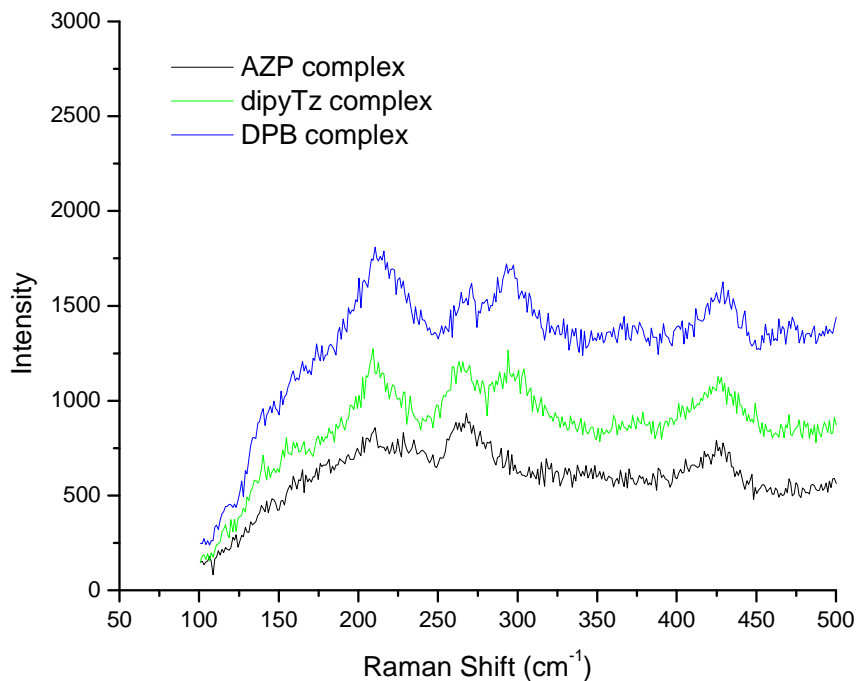


**Figure 2.9** Comparison of Raman spectra of  $\{[RuCl_2(dppb)](\mu-N-N)\}_n$  ( $\mu-N-N =$  AZP, DPB and dipyTz) in the range of  $50\sim 500\text{cm}^{-1}$ .

**Table 2.2** Raman Assignment of Bridging Ligands and Their Corresponding Ruthenium Complex

Assignment*	BP	BP complex	Pz <sup>27</sup>	Pz Complex	AZP <sup>23</sup>	AZP Complex	DPB	DPB Complex	dipyTz	dipyTz Complex
$\nu_{\text{ring}}^{28}$	1620	1612								1610
$\nu_{\text{ring}}^{28}$	1605		1580	1594	1587	1601	1589	1604	1589	
							1494	1501		
$\nu_{\text{N=N}}^{23}$					1495	1495			1494	1503
$\nu_{\text{ring}} + \delta_{\text{(CH)}}^{23}$					1465	1458				1439
$\nu_{\text{ring}} + \delta_{\text{(CH)}} + \nu_{\text{N=N}}^{23}$					1413	1419				
$\nu_{\text{ring}} + \delta_{\text{(CH)}}^{28}$	1300	1299			1333	1330	1345	1348	1305	1313
$\delta_{\text{(CH)}}^{28}$	1219	1230	1233	1234	1232		1211	1220	1214	1215
ring breathing+v (C-Nazo) + $\delta_{\text{(CH)}}^{23}$					1167	1162				
$\nu_{\text{ring}} + \delta_{\text{(CH)}}^{28}$		1073			1076					
$\nu_{\text{ring}}^{28}$		1021	1016	1026	1060	1013	1019	1014		1012
ring breathing <sup>28</sup>	1001	1003		999	990	936	988	997	994	
$\delta_{\text{ring}} + \nu_{\text{ring}}^{28}$					928				820	825
$\delta_{\text{ring}} + \nu_{\text{ring}}^{28}$	759	777								
$\delta_{\text{ring}}^{28}$	661		602	644	661	692	667	687		667
$\delta_{\text{ring}}^{28}$					657					606
		520		518		573	548	526		518

\*  $\nu$  = stretch,  $\delta$  = deformation

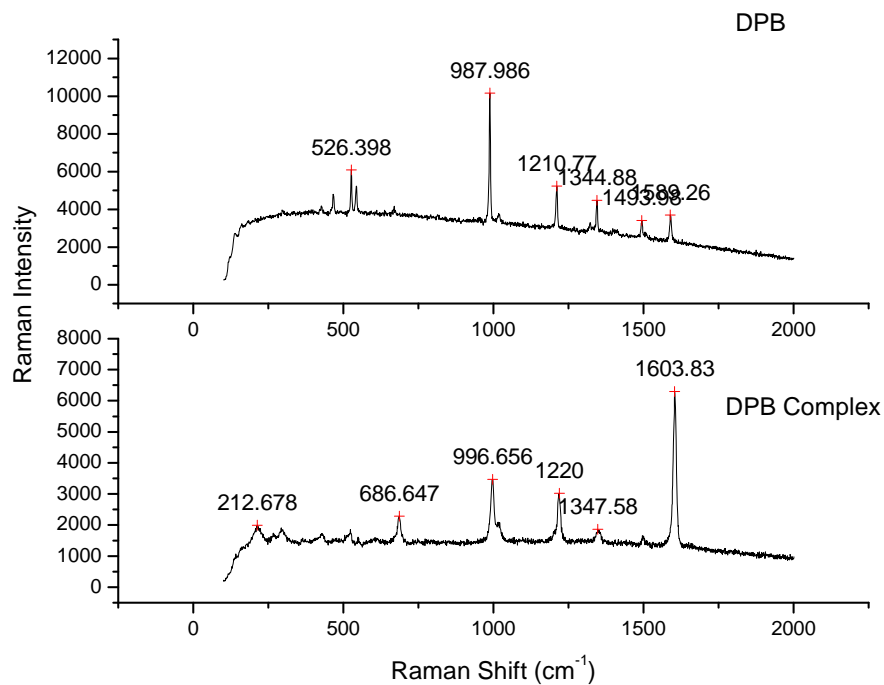


**Figure 2.4** Raman spectra of DPB and  $\{[\text{RuCl}_2(\text{dppb})](\mu\text{-DPB})\}_n$

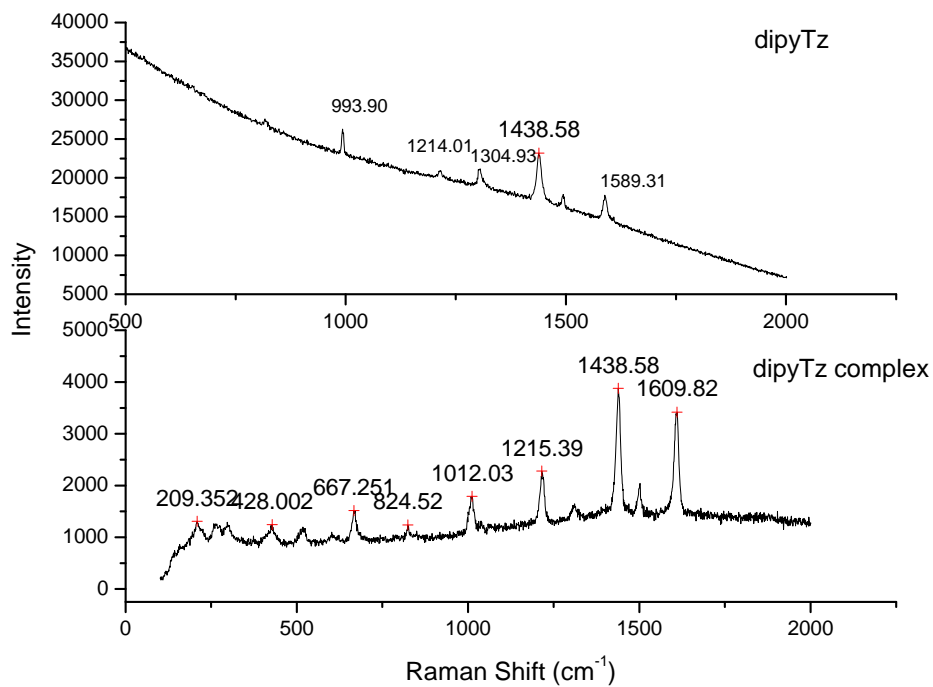


**Figure 2.5** Raman spectra of dipyTz and  $\{[\text{RuCl}_2(\text{dppb})](\mu\text{-dipyTz})\}_n$

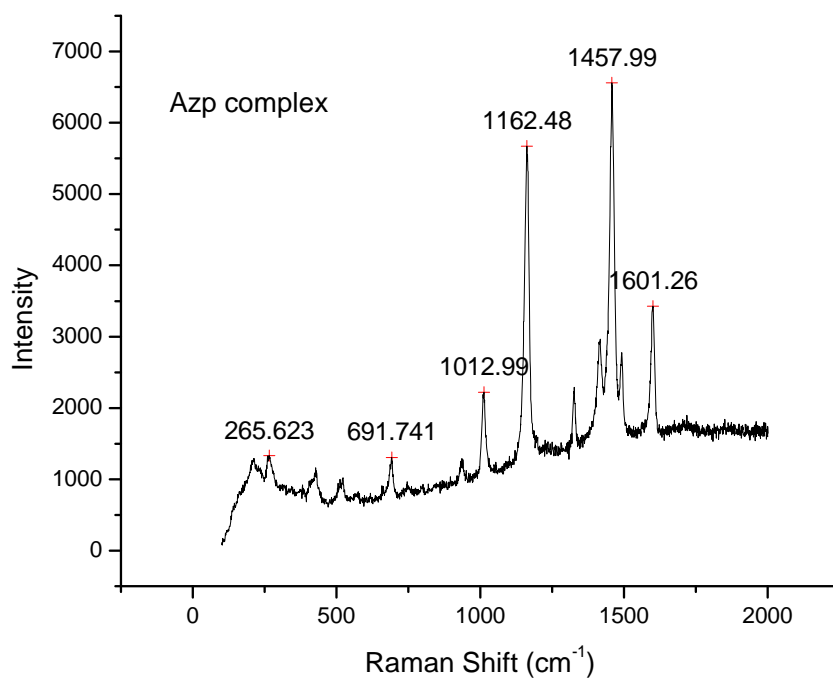


**Figure 2.6** Raman spectra of  $\{[\text{RuCl}_2(\text{dppb})](\mu\text{-AZP})\}_n$

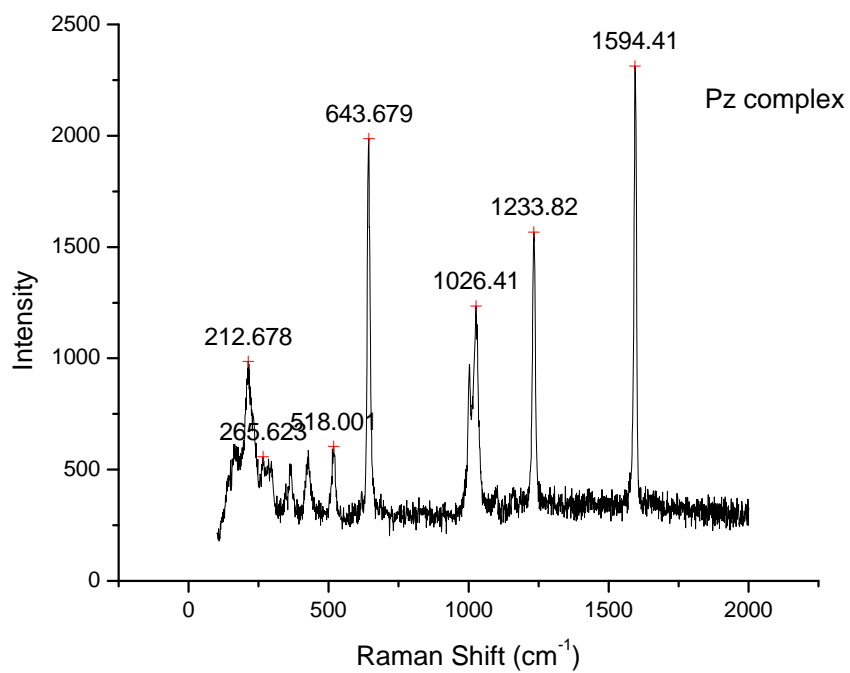


**Figure 2.7** Raman spectra of  $\{[\text{RuCl}_2(\text{dppb})](\mu\text{-pz})\}_n$

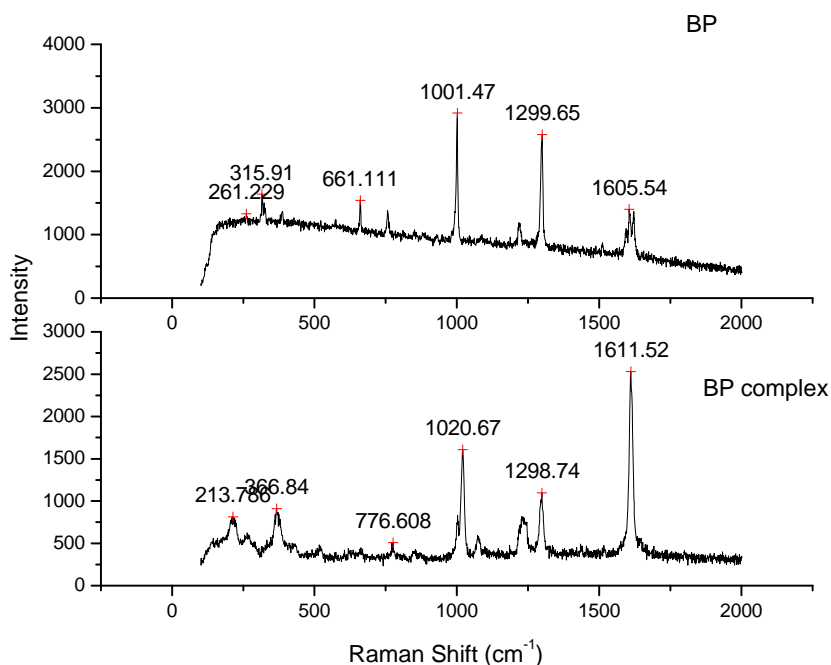


**Figure 2.8** Raman spectra of BP and  $\{[\text{RuCl}_2(\text{dppb})](\mu\text{-BP})\}_n$

### 2.3.4 NMR Spectra

The  $^1\text{H}$  NMR was measured for all the complexes, and the complete assignments are shown in Table 2.3. For the chemical shift at  $\alpha$ -pyridine position, all the coordinated complexes show a downfield shift compared to their corresponding free ligand; for the chemical shifts at  $\beta$ -pyridine position, all the coordinated complexes show an upfield shift compared to their free ligand. The changes in chemical shift suggest the interactions between the bridging ligands and Ruthenium atoms. Also the chemical shift of the Pz complex we measured is consistent with the published value although they define the peak at 7.07 as a doublet but a moderate broaden peak which is hard to determine the splitting observed in our case.<sup>20</sup> Interestingly, S. L. Queiroz could not assign the  $^1\text{H}$  NMR peaks of the complexes with 4,4'-bipyridine, 1,2-bistrans-(4-pyridyl)ethane and



1,2-bis-trans-(4-pyridyl)-ethylene ligands due to the complexity of the spectra which they attributed to the asymmetric structure affected by the environment surrounding the atoms in solution. However, the complex we synthesized with BP ligand and even more complicated ligands AZP, DPB and dipyTz show clean  $^1\text{H}$  NMR spectra and allow us to assign those peaks. From the integration of the peaks, we calculated the ratio of ligand to ruthenium dppb complex as 1:1. This is very useful information for determining the structure of these supramolecules. There are two main possibilities: one is the formation of a one dimensional linear structure, the other is to form a cyclic structure. Based on the Raman measurement, which suggests the two chloro are in trans position, the coordinated pyridines must be in cis positions that are trans to the two phosphines. This rationality eliminates the possibility of forming a one dimensional chain but a one dimensional loop which can hardly be achieved due to the rigidity of the bridging ligand. Considering all the information, cyclic structure is more reasonable.

More interestingly, two sets of pyridine peaks in the  $^1\text{H}$  NMR can be observed for DPB- and dipyTz- based complexes. This can be explained as equilibrium between triangle species and square species. According to a previous study,<sup>8</sup> the triangle species show an upfield shift at both  $\alpha$ -pyridine and  $\beta$ -pyridine positions compared to square species.  $\alpha$ -pyridine peaks at 8.82 and 8.87 are assigned to triangles and squares respectively for DPB complex; however,  $\beta$ -pyridine peaks of the two species overlap and cannot be differentiated. Similarly, for dipyTz complexes, peaks at 7.75 and 9.25 are assigned to triangle species and peaks at 9.3 and 7.8 are assigned to square species. In addition, the ratio of the two species has concentration dependence. Figure 2.11 shows  $^1\text{H}$  NMR of DPB complex at different concentrations. As the concentration increases from 1

mM to 5 mM to 18 mM, the ratio of squares to triangles changes from 1:6.3 to 1:1.4 to 1:0.96 based on the integrated area of relevant peaks. Thus, at low concentration, triangles are the abundant species while at high concentration, squares dominate. This behavior follows the general trend of thermodynamic control. Similar to DPB complex, dipyTz- based complex (Figure 2.12) also shows some change with increasing concentrations: the peak height at 7.80 decreases compared to that at 7.75. The changes become more obvious using a peak at 7.68 as a reference. This is because the baseline becomes noisier and the peaks are less resolved as concentration increases. Under such conditions, the integration of peaks at 7.75 and 7.80 may not be accurate enough to elucidate the trend. However, the spectra suggest that triangles dominate at both low and high concentrations. Such behavior has been observed for Pt- and Pd- based systems too,<sup>9</sup> although the controlling factor causing triangles to be dominant is still not clear at this stage. The AZP based complex (Figure 2.10) only shows one set of peaks indicating no equilibrium is involved. It also shows concentration dependence but in a different way. With concentration increasing, all the peaks become broader. The broadening of the peaks is probably due to some diamagnetic impurities in the sample.

**Table 2.3**  $^1\text{H}$  NMR Data in  $\text{CDCl}_3$ 

$\delta$ $^1\text{H}(\text{N—N})$ in $\text{CDCl}_3$	Pz	Pz Complex	BP	BP complex	AZP	AZP complex	DPB	DPB complex	dipyTz	dipyTz complex
$\alpha$ -pyr	8.60(s)	8.77(s)	8.75(d)	8.90(d)	8.66(d)	9.03(d)	8.45(d)	8.87(d)	8.96(d)	9.30(d)
$\alpha'$ -pyr								8.82(d)		9.25(d)
$\beta$ -pyr			7.54(d)	6.55(d)	7.53(d)	6.92(m)	7.25(d)	6.64(m)	8.52(d)	7.80(d)
$\beta'$ -pyr										7.75(d)
o-Ph		7.47(br)		7.59(br)		7.63(br)		7.57(br)		7.68(br)
m-Ph		7.09(t)		7.04(t)		7.07(t)		7.05(t)		7.10(t)
p-Ph		6.96(t)		7.14(t)		7.16(t)		7.15(t)		7.16(t)
P-CH <sub>2</sub> -		2.79(s, br)		3.03(s,br)		3.05(s,br)		3.03(s,br)		3.13(s,br)
P-CH <sub>2</sub> - CH <sub>2</sub> -		1.68(s,br)		1.62(s,br)		1.72(s,br)		1.65(s,br)		1.72(s,br)

\* s — singlet; d — doublet; t — triplet; m — multiplet; br — broad.

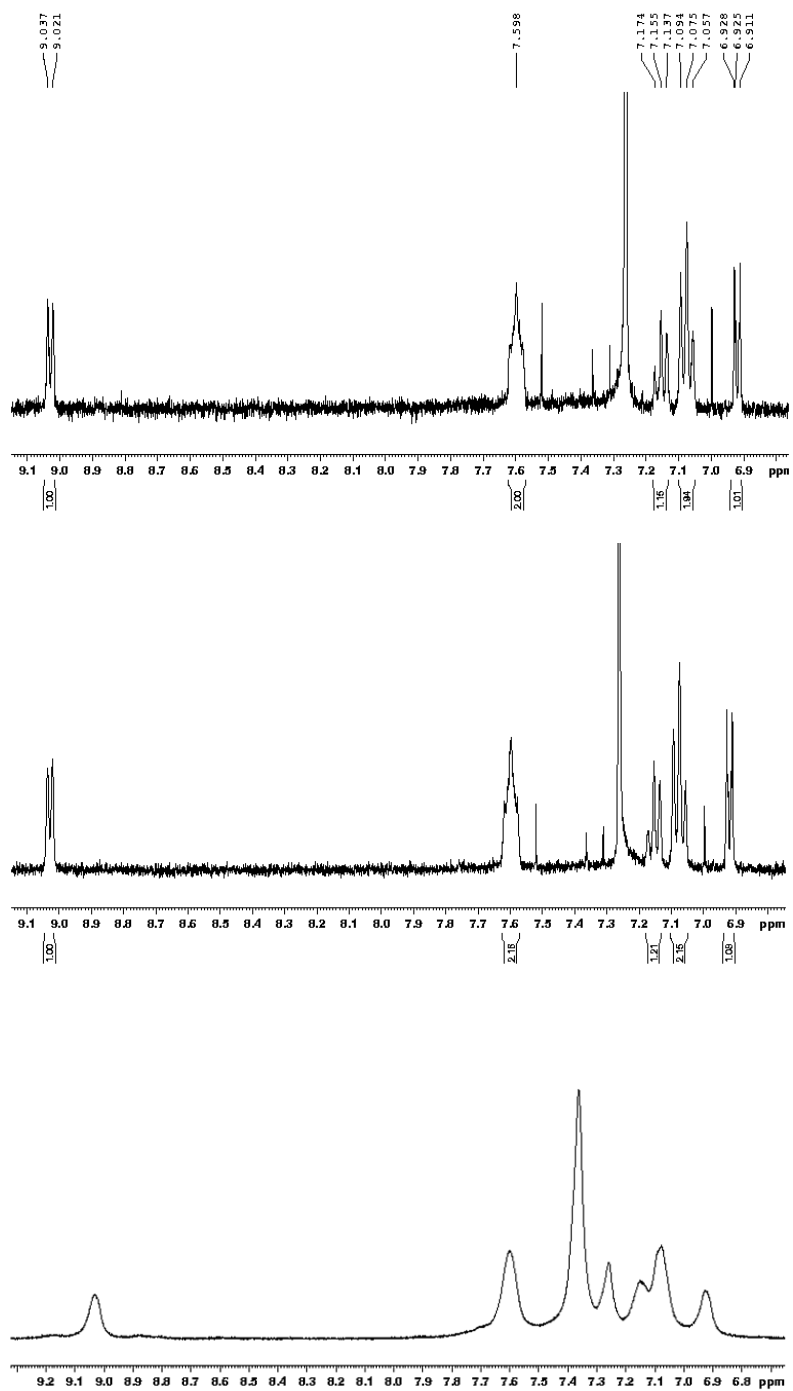


**Figure 2.10**  $^1\text{H}$  NMR Spectra changes with increasing AZP complex concentration, the concentration of the bottom one is 16mM

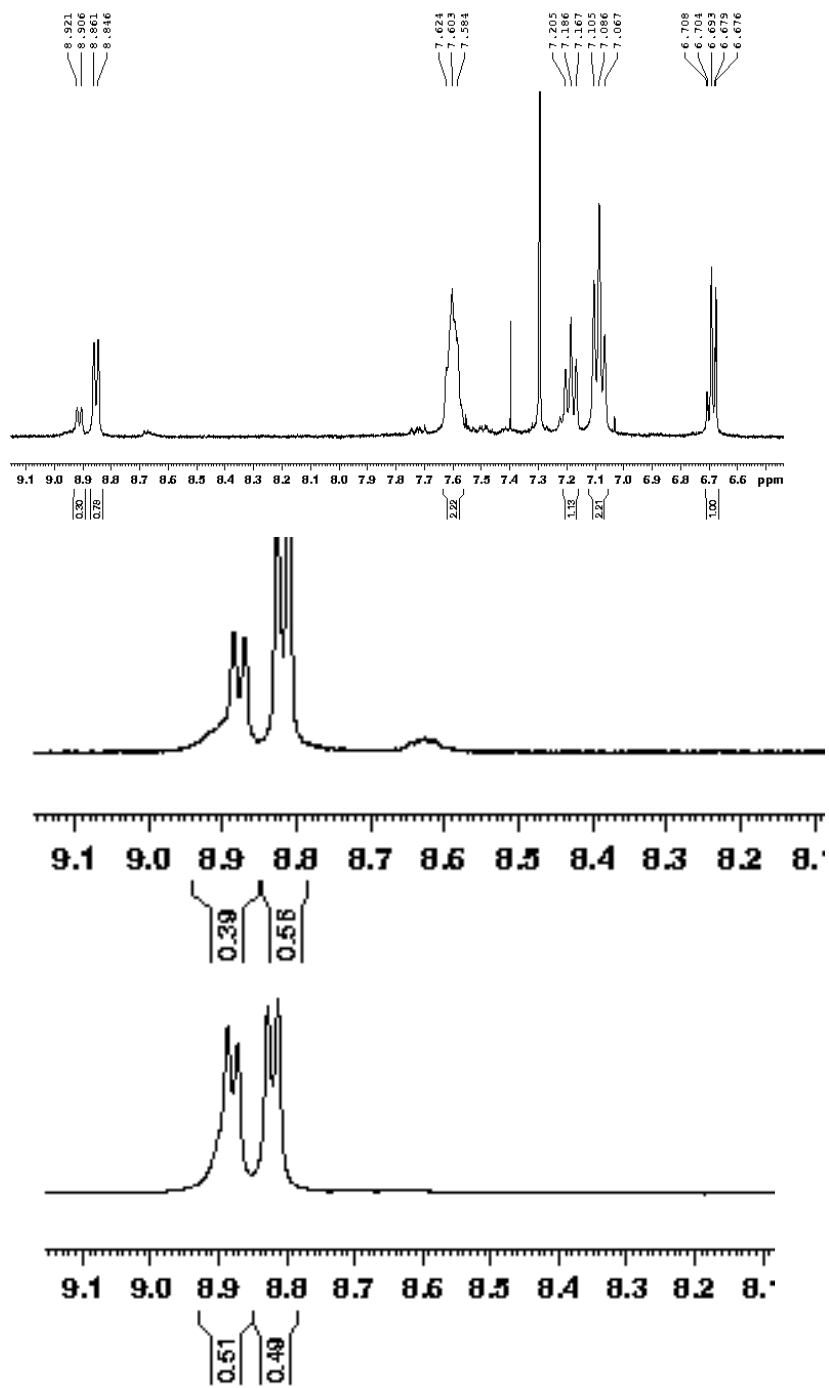


**Figure 2.11**  $^1\text{H}$  NMR Spectra changes with increasing DPB complex concentration.

The concentrations from top to bottom are 1mM, 5mM and 18 mM respectively.

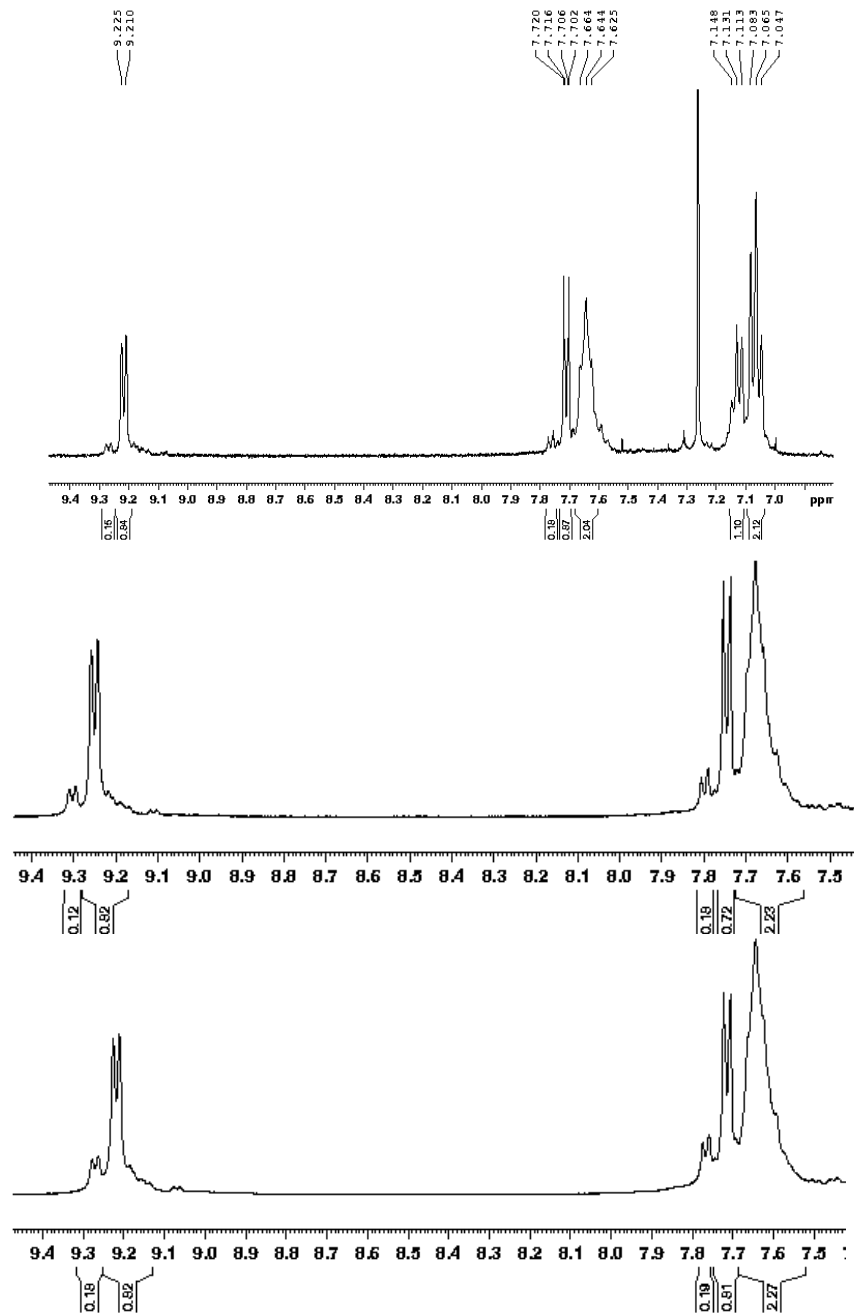


**Figure 2.12**  $^1\text{H}$  NMR Spectra changes with increasing dipyTz complex concentration

To further study the size effect of these supramolecules, Pulsed-Field Gradient NMR Spectroscopy (PFG-NMR) was employed in this study. This method was first adopted in Otto's study to characterize large molecular squares.<sup>18</sup> The concept behind this measurement is that the larger the size of molecule, the smaller the diffusion coefficient. Based on the determined diffusion coefficient from certain NMR peak, it could tell whether the multiple resonances are related to species with different sizes (i.e. contaminants with slightly shifted resonances) or species with identical sizes (low – symmetry conformer or set of conformers of a single species). In a PFG-NMR experiment with BPPLIED program, the attenuation of a resonance depends on the gradient area as shown in equation 2.2:

$$I = I_0 \exp[-D(\Delta - \delta/3 - \tau/2)g^2\gamma^2\delta^2] \quad \text{Eq. 2.2}$$

Where  $I_0$  is the resonance intensity in the absence of a gradient pulse, ( $g=0$ ),  $\gamma$  is the gyromagnetic ratio,  $\Delta$  is the diffusion delay time,  $g$  and  $\delta$  are the amplitude and duration of the gradient pulses, and  $D$  is the self-diffusion coefficient. The diffusion coefficient can be extracted from the linear fits using Origin software. To compare the values from our study and from the literature, diffusion coefficients measured in chloroform were converted to numbers at other media using the Stokes-Einstein equation 2.3:

$$D = K_B T / 6\pi\eta r \quad \text{Eq. 2.3}$$

Where  $K_B$  is Boltzmann's constant,  $r$  is the effective molecular radius,  $T$  is the absolute temperature, and  $\eta$  is the solvent viscosity ( $\eta_{\text{H}_2\text{O}}$  is 1cP,  $\eta_{\text{CHCl}_3}$ =0.57cP,  $\eta_{\text{DMSO}}$ =2.24cP). Table 2.4 shows the measured diffusion coefficient in  $\text{CHCl}_3$  and the calculated diffusion

coefficient in DMSO. These values are consistent with the reported values. For example, the diffusion coefficient of 4, 4-bipyridine in DMSO that we calculated is  $5.3 \pm 0.85 \times 10^{-6} \text{ cm}^2 \text{ sec}^{-1}$  compared to the published value of  $6.03 \pm 0.04 \times 10^{-6} \text{ cm}^2 \text{ sec}^{-1}$ . The diffusion coefficient of bipy complex in DMSO we obtained is  $1.36 \pm 0.06 \times 10^{-6} \text{ cm}^2 \text{ sec}^{-1}$  in comparison with the reported value of  $[\text{Re}^1(\text{CO})_3\text{Cl}(\text{BP})]_4$ , which is  $1.42 \pm 0.05 \times 10^{-6} \text{ cm}^2 \text{ sec}^{-1}$ .<sup>18</sup> The difference of the latter could be attributed to the bulky corner  $\text{Ru}(\text{dppb})\text{Cl}_2(\text{N-N})$  which would have resulted in a larger size molecule and a smaller diffusion coefficient. Comparing the diffusion coefficients of all the complexes in Table 2.4, it is difficult to come up with a trend since the differences are within the error. Again, the bulky corner makes the size of the complexes less sensitive to the length of bridging ligands and could not be differentiated. However, from PFG-NMR measurement, we can conclude that the diffusion coefficients of complexes are of the magnitude of a trimer or a tetramer.

**Table 2.4** Molecular Diffusion Coefficients Measured from PFG-NMR

Molecules	Measured D ( $\text{CHCl}_3$ ) ( $\times 10^{-6} \text{ cm}^2 \text{ sec}^{-1}$ )	Calculated D (DMSO) ( $\times 10^{-6} \text{ cm}^2 \text{ sec}^{-1}$ )
4,4-bipyridine	20.92	5.3
	(3.34)	(0.85)
$\{[\text{RuCl}_2(\text{dppb})](\text{BP})\}_4$	5.36	1.36
	(0.23)	(0.06)
$\{[\text{RuCl}_2(\text{dppb})](\text{AZP})\}_4$	5.41	1.38
	(0.03)	(0.008)
$\{[\text{RuCl}_2(\text{dppb})](\text{DPB})\}_3$	5.31	1.35
	(0.096)	(0.025)
$\{[\text{RuCl}_2(\text{dppb})](\text{dipyTz})\}_3$	5.45	1.39
	(0.021)	(0.054)

\* The numbers in the parentheses are standard deviation based on three measurements.



### 2.3.5 Electrochemistry

The cyclic voltammetry of the AZP complex in Figure 2.13 shows a reversible redox couple with  $E_{1/2}$  around 631 mV versus Ag|AgCl. In addition, the oxidation peak current increases linearly with the square root of scan rate indicating that the electrochemical process is mainly a solution behavior and no molecules are absorbed on the electrode surface. Similar to AZP complex, BP, DPB and dipyTz based complexes all show a single redox couple with a slightly different half-wave potential. These values are summarized in Table 2.5. The half-wave potentials are consistent with a previous study<sup>25</sup> that the two trans chlorides makes the reduction of the complex easier. The electrolysis of these complexes suggests one electron transfer corresponding to each Ruthenium corner. Considering the observed wave of these complexes have all of the shape characteristics of a one-electron transfer even though it is actually the result of multi-merged one-electron transfers, the electrochemical behavior of these complexes can be categorized into the special case in ErEr system where  $\Delta E_0 = E_k^0 - E_1^0 = -\frac{2RT}{F} \ln K$  (K is the number of electron transferred). Such a system has been observed for electrochemical oxidation of poly(vinylferrocene) in which the multiple redox centers are noninteracting with each other<sup>29</sup> and been well studied by Polcyn<sup>30</sup>. Thus, the electron transfer process of these Ruthenium complexes involves either four successive one-electron transfers or three successive one-electron transfers depending on their actual geometries in solution. Different from the redox behavior described above, Pz based complex shows two consecutive redox couples (Figure 2.14). This is caused by the interaction of neighboring ruthenium atoms. Since Pz is much shorter than the other linkers in terms of the length, the interaction between the ruthenium corners is much

stronger. The electron transfer process for Pz complex was proposed by Queiroz <sup>20</sup> that involved two consecutive oxidations of Ruthenium atoms located on opposite positions in the square.

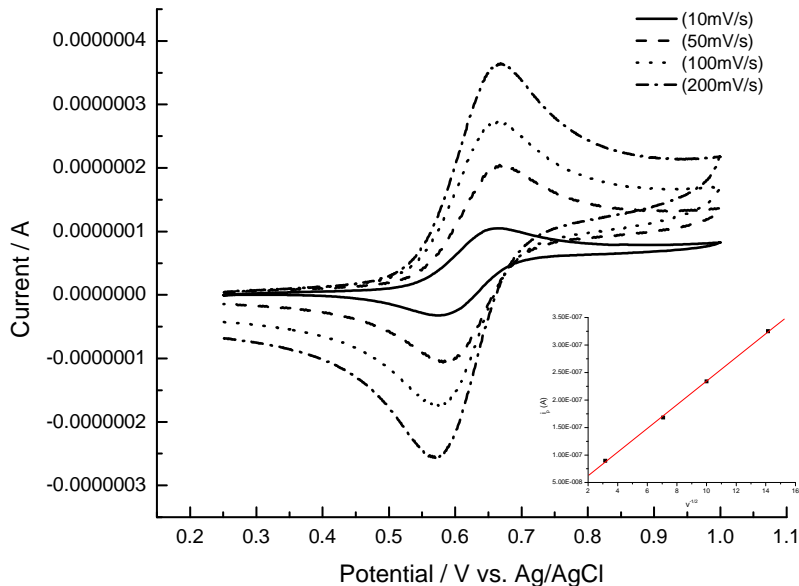


**Figure 2.13** Cyclic voltammetry of AZP complex at different scan rates in CH<sub>2</sub>Cl<sub>2</sub>, electrolyte is 0.1M TBAP.

**Table 2.5** Summary of half wave potential and peak separation of

{[RuCl<sub>2</sub>(dppb)](μ -N-N)}<sub>n</sub>, μ -N-N=AZP, DPB and dipyTz

{[RuCl <sub>2</sub> (dppb)](μ -N-N)} <sub>n</sub>	E <sub>ap</sub> (mV)	E <sub>cp</sub> (mV)	E <sub>1/2</sub> (mV)	Δ E (mV)
μ -N-N=AZP	667	595	631	72
μ -N-N=DPB	675	618	647	57
μ -N-N=dipyTz	675	622	649	53

\* ap denotes anodic peak and cp denotes cathodic peak

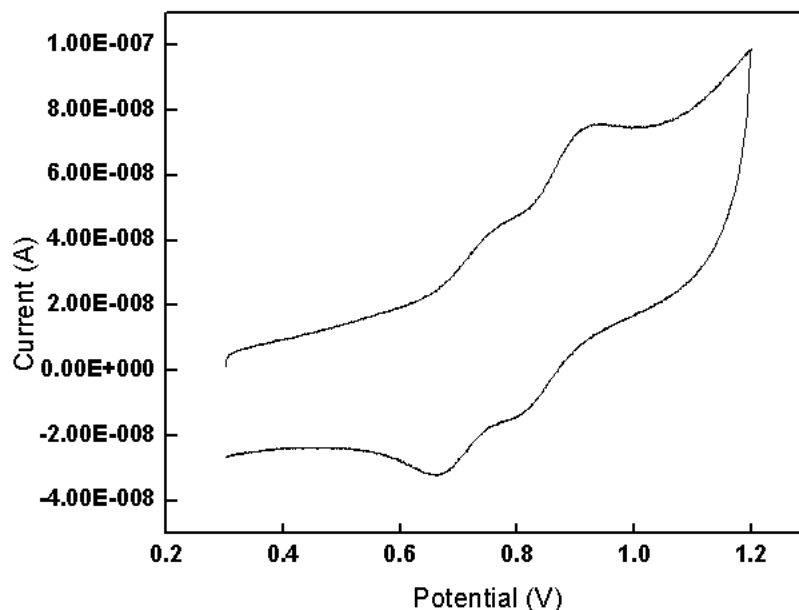


**Figure 2.14** Cyclic voltammetry of Pz complex in CH<sub>2</sub>Cl<sub>2</sub>, electrolyte is 0.1M TBAP.

Since all these complexes are electro active, it is more convenient to use the potential step method to measure their diffusion coefficient. This method is based on the Cottrell Equation shown below:

$$I = nFAC_0 \sqrt{\frac{D}{\pi \cdot t}} \quad \text{Eq. 2.4}$$

Where I is the faradic current, n is the electron transferred, F is Faraday's constant, A is the geometric area of the electrode, C<sub>0</sub> is the bulk concentration of the solution, D is the diffusion coefficient, and t is the time. By making a plot of I vs. t<sup>-1/2</sup>, a slope can be derived. Based on the slope, D can be calculated. In order to reduce the capacitance current, a home made Pt electrode with diameter of 0.6 mm was used. There are two main advantages of using this method in this system: (1) In equation 2.4, the term C<sub>0</sub> can

be rewritten as shown in equation 2.5 where  $W$  is the complex weight measured during the experiment;  $n=3$  stands for a triangle and  $n=4$  stands for a square;  $M_{corner}$  is the molecular weight of  $Ru(dppb)Cl_2(N-N)$ ; and  $V$  is the volume of the solvent. By substituting equation 2.5 into equation 2.4, equation 2.6 can be derived where  $n$  will be cancelled out. Therefore no presumption needs to be made in terms of square or triangle in this method.

$$C_0 = \frac{\text{moles}}{V} = \frac{W / (n \cdot M_{corner})}{V} \quad \text{Eq. 2.5}$$

$$I = \frac{FAW}{M_{corner}V} \sqrt{\frac{D}{\pi \cdot t}} \quad \text{Eq. 2.6}$$

(2) Due to the high sensitivity of electrochemistry, quantitative analysis can be achieved at a very low concentration. Based on the  $^1H$  NMR study, at low concentrations triangles will be the dominating species in the DPB- and dipyTz- based system. Therefore, the diffusion coefficient measured should be very close to that of a triangle. The experimental results are shown in Table 2.6.

**Table 2.6** Diffusion Coefficient measured from Potential Step Experiment

Molecules	Measured D ( $CHCl_3$ ) ( $\times 10^{-6} \text{ cm}^2 \text{ sec}^{-1}$ )
$\{[RuCl_2(dppb)](BP)\}_4$	3.82
$\{[RuCl_2(dppb)](AZP)\}_4$	2.46
$\{[RuCl_2(dppb)](DPB)\}_3$	3.48
$\{[RuCl_2(dppb)](dipyTz)\}_3$	2.90

In comparison to the diffusion coefficient measured using PFG-NMR, the value we obtained from the potential step experiment is in the same magnitude but relatively

small probably due to the electrolyte used in the electric cell which drags down the diffusion of  $\{[\text{RuCl}_2(\text{dppb})](\mu\text{-N-N})\}_n$ . However when all the data in Table 2.6 is compared, they are self-consistent. BP is the shortest linker; therefore it has the largest diffusion coefficient. DPB complex exists as triangles at low concentration. Due to DPB's long chain, its complex has slightly smaller diffusion coefficient than the BP complex. The AZP complex has a diffusion coefficient larger than both the BP and DPB complexes, suggesting a square geometry. The diffusion coefficient of the dipyTz complex is smaller than the DPB complex which is somewhat unexpected considering triangles dominate both complexes at studied concentrations, and dipyTz has a slightly shorter chain than DPB. This may be caused by an experimental error. Overall the potential step experiment is a valid method to study the diffusion coefficient of this type of complex. It is fast, convenient and efficient; no sophisticated instrumentation and data processing is required. To the best of our knowledge, this is the first report of using a potential step experiment to measure these triangle and square mixtures. A theoretical model which can separate the current of triangle from that of square will further increase the accuracy of this method.

### **2.3.6 Other Characterization Techniques**

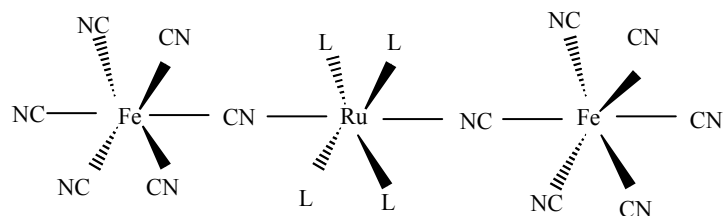
Crystals can be grown for certain complexes through the slow diffusion method; however the crystals cannot survive the strong intensity of X-rays. Mass spectrometers including ES-MS and MALDI-MS have also been tried to study these supramolecules. ES-MS is limited by the measurable mass range which is less than 3000, and all our complexes have a molecular weight over 3000. MALDI-MS has a larger mass range, but the  $\text{N}_2$  laser is too strong to decompose the complex even with the matrix. For all the

mass spectra, only the fragmentations can be detected, which is consistent with the proposed structure. Parent ions, however, cannot be detected.

### 2.3.7 Extended Framework

In this study, we paid particular attention to the development of three dimensional frameworks using these molecular squares or triangles as building blocks. Since BP- and AZP- based complexes can be isolated as unique products, they are used as the starting materials to build more complicated structures. Two strategies have been tried in this study:

(1) Using cyano complex as a linker to interconnect these squares. A previous study done by Alborés showed that  $\text{trans-RuL}_4\text{Cl}_2$  (L) (L=pyridine, 4-tert-butylpyridine, or 4-methoxypyridine) could react with potassium hexacyanoferrate(III) and form trinuclear cyano-bridged mixed-valent compounds (scheme 2.2).<sup>31</sup> Based on this, it is reasonable to propose connecting ruthenium molecular squares in which the two chlorides are in trans position with a cyano-complex. The reaction was carried out by mixing the two phases of potassium hexacyanoferrate(III) in  $\text{H}_2\text{O}$  and ruthenium bipy squares in  $\text{CH}_2\text{Cl}_2$ . The mixture was then sonicated in a sonicator overnight. The initial orange color of ruthenium bipy square gradually changed into a green color. The resulting green solid material proved to be insoluble in most of the solvents. This is actually consistent with previous reports that large building units tend to form insoluble materials when linked by a cyano complex. The insolubility of the complex creates difficulty in characterizing this supramolecule particularly well. The solid state NMR was run and the spectra observed supported the proposed structure; however a detailed structure of the complex can not be obtained.



**Scheme 2.2** Molecular structure of cyano-bridged compound

(2) Using  $\text{AgBF}_4$  to remove the chloride atoms by forming  $\text{AgCl}$  precipitate, then substituting the chlorides with linkers. This synthetic strategy is widely used for  $\text{PtL}_2\text{Cl}_2$  or  $\text{PdL}_2\text{Cl}_2$  based metal corners. In addition to  $\text{AgBF}_4$ ,  $\text{AgOTf}$  can also be used. The experiment was carried out with a BP complex as starting material.  $\text{AgBF}_4$  was added under dark conditions and stirred overnight to make sure that the chloride ions were removed completely. After that, the turbid solution was separated by filtration and AZP was added to the filtrate to form the framework. The difficulty in this synthesis is the filtration step: the formed  $\text{AgCl}$  cannot be completely separated from the filtrate. The unremoved  $\text{AgCl}$  can continue to react with the bridging ligand and form impurities. The crude product is characterized with SERS on the surface of silver colloid, which is shown in Figure 2.15. The spectra at different polarizations support the proposed structure where the added AZP linker is perpendicular to the BP square plane. More characterization needs to be done to fully confirm the structure.

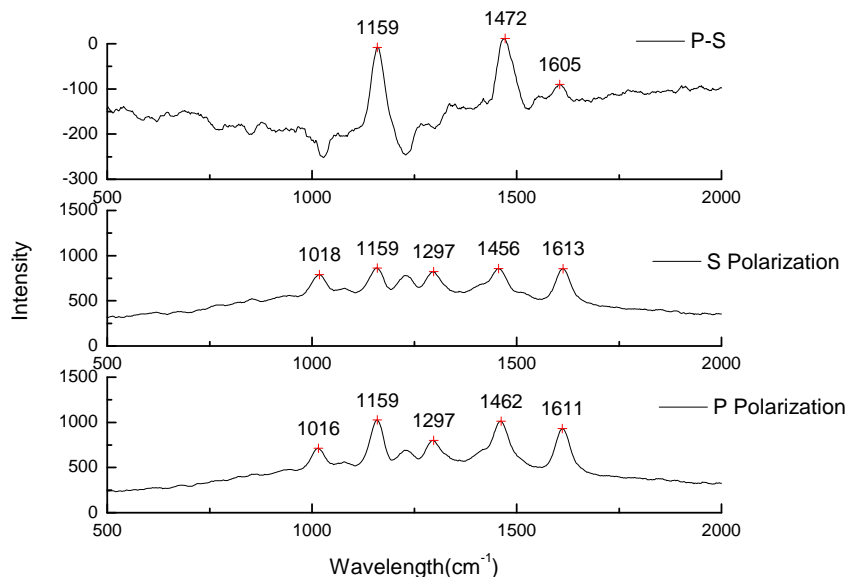


**Figure 2.15** SERS of  $\{[\text{RuCl}_2(\text{dppb})](\mu\text{-BP})\}_4$  after removing Chloroatoms and adding AZP as an intersquare linker. (P-S — SERS at P Polarization subtracts that at S Polarization)

## 2.4 Conclusions

Three new supramolecules  $\{[\text{RuCl}_2(\text{dppb})](\mu\text{-N-N})\}_n$ ,  $\mu\text{-N-N}=\text{AZP}$ , DPB, dipyTz were synthesized and characterized using UV-Vis, Raman and NMR. The characterization confirms the square structure of the AZP complex and a mixture of square and triangle of the DPB and dipyTz complexes. At low concentrations, triangle species are dominant for both complexes, while at high concentrations square species are dominant for DPB complex and triangle dominates for dipyTz complex. The equilibrium in DPB complex solution is under thermodynamic control and that of dipyTz complex is still not quite understood. Electrochemical experiments (cyclic voltammetry and controlled potential electrolysis) show the shape characteristics of a one-electron transfer



although it is the result of multi merged one-electron transfers for the complexes containing AZP, DPB and dipyTz ligands suggesting the multiple Ruthenium redox centers are not interacting with each other due to the long distance of the bridging ligand. The potential step experiment was proved to be a valid method for studying square/triangle complexes which gave results consistent with the established PFG-NMR method.

## 2.5 References

1. Fujita, M., *Chem. Soc. Rev.* **1998**, 27, 417-425.
2. Fujita, M.; Ogura, K., *Coord. Chem. Rev.* **1996**, 148, 249-164.
3. Leininger, S.; Olenyuk, B.; Stang, P. J., *Chem. Rev.* **2000**, 100, 853-908.
4. Fujita, M.; Kwon, Y. J.; Washizu, S.; Ogura, K., *J. Am. Chem. Soc.* **1994**, 116, 1151-1152.
5. Slone, R. V.; Hupp, J. T., *Inorg. Chem.* **1997**, 36, 5422-5423.
6. Thanasekaran, P.; Liao, R.-T.; Liu, Y.-H.; Rajendran, T.; Rajagopal, S.; Lu, K.-L., *Coord. Chem. Rev.* **2005**, 249, 1085-1110.
7. Schweiger, M.; Seidel, S. R.; Arif, A. M.; Stang, P. J., *Angew. Chem. Int. Ed.* **2001**, 40, (18), 3467-3469.
8. Ferrer, M.; Rodriguez, L.; Rossell, O., *J. Organomet. Chem.* **2003**, 681, 158-166.
9. Ferrer, M.; Mounir, M.; Rossell, O.; Ruiz, E.; Maestro, M. A., *Inorg. Chem.* **2003**, 42, 5890-5899.
10. Fujita, M.; Yazaki, J.; Ogura, K., *J. Am. Chem. Soc.* **1990**, 112, 5645-5647.
11. Milac, T. N.; Chi, N.; Yablon, D. G.; Flynn, G. W.; Batteas, J. D.; Drain, C. M., *Angew. Chem. Int. Ed.* **2002**, 41, 2117.

12. Drain, C. M.; Batteas, J. D.; Flynn, G. W.; Milac, T.; Chi, N.; Yablon, D. G.; Sommers, H., *Proc. Natl. Acad. Sci.* **2002**, 99, 6498.
13. Drain, C. M.; Nifiatis, F.; Vasenko, A.; Batteas, J. D., *Angew. Chem. Int. Ed.* **1998**, 37, 2344.
14. Belanger, S.; Hupp, J. T.; Stern, C. L.; Slone, R. V.; Watson, D. F.; Carrell, T. G., *J. Am. Chem. Soc.* **1999**, 121, 557-563.
15. Lee, S. J.; Hupp, J. T., *Coord. Chem. Rev.* **2006**, 250, 1710-1723.
16. Lee, S. J.; Lin, W., *Acc. Chem. Res.* **2007**, 41, (4), 521-537.
17. Holló-Sitkei, E.; Tárkányi, G.; Párkányi, L.; Megyes, T.; Besenyei, G., *Eur. J. Inorg. Chem.* **2008**, 1573-1583.
18. Otto, W. H.; Keefe, M. H.; Splan, K. E.; Hupp, J. T.; Larive, C. K., *Inorg. Chem.* **2002**, 41, 6172-6174.
19. Graves, C. R.; Merlau, M. L.; Morris, G. A.; Sun, S.-S.; Nguyen, S. T.; Hupp, J. T., *Inorg. Chem.* **2004**, 43, 2013-2017.
20. Queiroz, S. L.; Kirkuti, E.; Ferreira, A. G.; Santlago, M. O.; Batista, A. A.; Castellano, E. E.; Ellena, J., *Supramol. Chem.* **2004**, 16, (4), 255-262.
21. Sun, S.-S.; Lees, A. J., *J. Am. Chem. Soc.* **2000**, 122, 8956-8967.
22. Rajendran, T.; Manimaran, B.; Liao, R.-T., *Inorg. Chem.* **2003**, 42, 6388-6394.
23. Zhuang, Z.; Cheng, J.; Wang, X.; Yin, Y.; Chen, G.; Zhao, B.; Zhang, H.; Zhang, G., *J. Mol. Struct.* **2006**, 794, 77-82.
24. Akyuz, S.; Dempster, A. B.; Morehouse, R. L., *J. Mol. Struct.* **1973**, 17, 105-125.

25. Queiroz, S. L.; Batista, A. A.; Oliva, G.; Teresa, M.; Gambardella, D. P.; Santos, R. H. A.; MacFarlane, K. S.; Rettig, S. J.; James, B. R., *Inorg. Chim. Acta* **1998**, 267, 209-221.
26. Bandeira, M. C. E.; Crayston, J. A.; Gonçalves, N. S.; Noda, L. K.; Glidle, A.; Franco, C. V., *J. Solid State Electrochem.* **2007**, 11, 231-239.
27. Arenas, J. F.; Woolley, M. S.; Otero, J. C.; Marcos, J. I., *J. Phys. Chem.* **1996**, 100, 3199-3206.
28. Akyuz, S.; Akyuz, T.; Davies, J. E. D., *J. Mol. Struct.* **1995**, 349, 61-64.
29. Flanagan, J. B.; Margel, S.; Bard, A. J.; Anson, F. C., *J. Am. Chem. Soc.* **1978**, 100, (13), 4248-4253.
30. Polcyn, D. S.; Shain, I., *Anal. Chem.* **1966**, 38, (3), 370-375.
31. Albores, P.; Slep, L. D.; Weyhermüller, T.; Baraldo, L. M., *Inorg. Chem.* **2004**, 43, 6762-6773.

**CHAPTER THREE**

**PERMEATION STUDY OF RUTHENIUM (II) MOLECULAR SQUARE BASED  
MEMBRANES IN SOLUTION PHASE AND GAS PHASE**

**3.1 Introduction**

Membrane separation technology has attracted tremendous interest in recent years due to its cost-effective advantages over conventional technology. It plays an important role in environmental- and energy-related purification processes such as VOC removal, water filtration, and hydrogen purification. So far, different kinds of membranes such as polymer membranes,<sup>1-4</sup> inorganic membranes,<sup>5,6</sup> and organic-inorganic hybrid membranes<sup>7</sup> have been fabricated. And recently, transition metal directed cyclic materials “molecular squares” show promise in membrane separation.<sup>8, 9, 10, 11</sup> These tetramers were formed by coordination of metal-ion corners and difunctional bridging ligands. Their rigid structure, flexible design and most importantly, their tunable porosities and chemical properties, make them ideal candidates for separation. The most commonly used metal ion corners under study are Re-, Pt- or Pb- based corners. However few Ru-based molecular squares have been reported. In 2004, Salefe L. Queiroz published a study revealing the synthesis and characterization of a series ruthenium- based molecular squares.<sup>12</sup> As they claimed that the bulky phosphino groups may somehow prevent the formation of channels, they didn’t report any application regarding these molecular squares. After restudying these molecules, we surprisingly found that these materials

showed good separation properties as well. Here we report the permeation study of membranes based on these ruthenium molecular squares in both solution phase and gas phase.

## 3.2 Experimental

### 3.2.1 Materials

$\{[\text{RuCl}_2(\text{dppb})](\mu\text{-}4,4'\text{-bipy})\}_4$  (cavity dimension  $11\text{\AA}\times 11\text{\AA}$ )<sup>12</sup> and  $\{[\text{RuCl}_2(\text{dppb})](\mu\text{-pz})\}_4$  (cavity dimension  $5.6\text{\AA}\times 5.7\text{\AA}$ )<sup>13</sup> were synthesized by mixing precursor  $[\text{RuCl}_2(\text{dppb})](\mu\text{-dppb})$  stoichiometrically with bridging ligands 4,4'-bipyridine and pyrazine, respectively, under  $\text{N}_2$  protection<sup>12</sup>. Redox probe molecules  $\text{Co}(\text{bpy})_3(\text{ClO}_4)_3$  ( $d \sim 11\text{\AA}$ )<sup>14</sup> were prepared and purified according to the procedures given in the literature<sup>15</sup>;  $\text{Ru}(\text{NH}_3)_6\text{Cl}_3$  ( $d \sim 5.5\text{\AA}$ )<sup>9</sup> were purchased from Sigma-Aldrich and used as received. Benzene, cyclohexane, toluene (reagent grade) used for gas phase separation and other solvents were purchased from Fisher. Alumina filters with diameter 25 mm and pore size  $0.2\text{ }\mu\text{m}$  were purchased from Whatman.

### 3.2.2 Membrane preparation

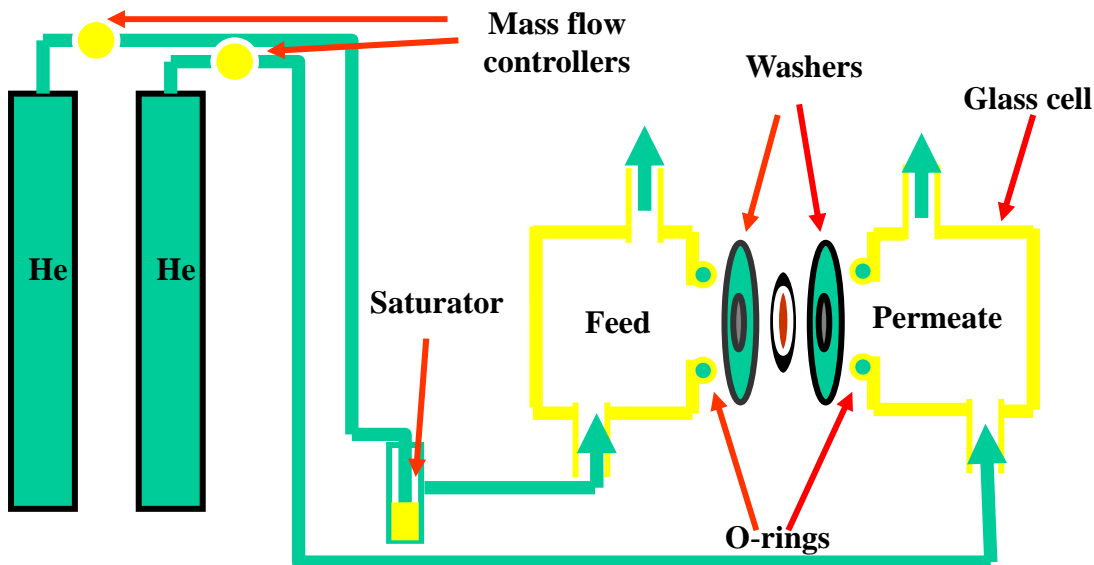
Molecular squares were first dissolved in dichloromethane. For solution phase separation, the membrane was made by drop-coating a molecular square solution directly onto glassy carbon surface. For gas phase separation, porous alumina was used as a membrane support and molecular square solution was drop-coated onto the support through a syringe. To avoid defects, layer by layer formation is required. The second layer was introduced only after the previous layer was completely dried.

### 3.2.3 Measurements

Solution phase separation was monitored by electrochemical method. All the measurements were performed in an aqueous solution containing 0.1M KNO<sub>3</sub> as the electrolyte. A standard three-electrode, one-compartment cell was employed. The working electrode was a 3 mm diameter glassy carbon electrode covered with molecular square film. The reference and counter electrodes are Ag/AgCl and platinum gauge, respectively. Epsilon Potentiostat from BASi was employed.

Gas phase separation was monitored by Gas Chromatography. The permeation measurements were performed by placing the molecular square membranes between the two halves of a home-made cell. The set up is shown in scheme 3.1. Each half cell contained an inlet, an outlet, and an opening that exposed the gases to the membrane. The molecular square membrane was first stabilized by two washers and then placed between the two half cells. The connection parts were sealed by grease and were kept air-tight. Helium was used as the carrier gas, and the flow was controlled by mass flow controllers. There were two gas flow lines. One was the feed line which flowed to the saturator containing a binary mixture of VOCs and then went to the half cell. The other line swept past the other side of the membrane and served as the permeate line. During each experiment, the initial flow rates of the feed line and permeate line were set the same, around 12-15 cm<sup>3</sup>min<sup>-1</sup> (ccm). The composition of each half cell was repeatedly measured by Gas Chromatography until the system reached equilibrium. After the measurements, only helium was used as feed to remove the VOCs that stuck on the membrane surface. All the parallel measurements were made under similar experiment conditions. Gas Chromatography with a flame ionization detector and a C<sub>18</sub> Column were

employed.



**Scheme 3.1** Gas separation Setup

### 3.3 Results and Discussion

#### 3.3.1 Membrane characterization

The membrane is characterized by AFM and contact angle changes. As a glassy carbon electrode can not be directly scanned by AFM, gold sputter-coated mica is used as substrates. The membrane formed by drop-coating proves to be not quite uniform due to the different evaporation speeds on the center and edge parts, which is clearly shown in the AFM images. Usually the centre part is thin and uniform as shown in Figure 3.1, while the edge is relative thick and rough. Although several defects can be detected, the depth of the defects is less than the thickness of the film which means the under layer defects could be covered by upper layer. Therefore, layer by layer formation could effectively avoid severe defects forming. The membrane formed on alumina support is

also characterized by AFM as shown in Figure 3.2. Some molecular squares fill in the pores, and some spread on the surface. In addition, the alumina membrane after coating becomes more hydrophobic, a fact reflected by the increased contact angle of a water droplet on the surface.

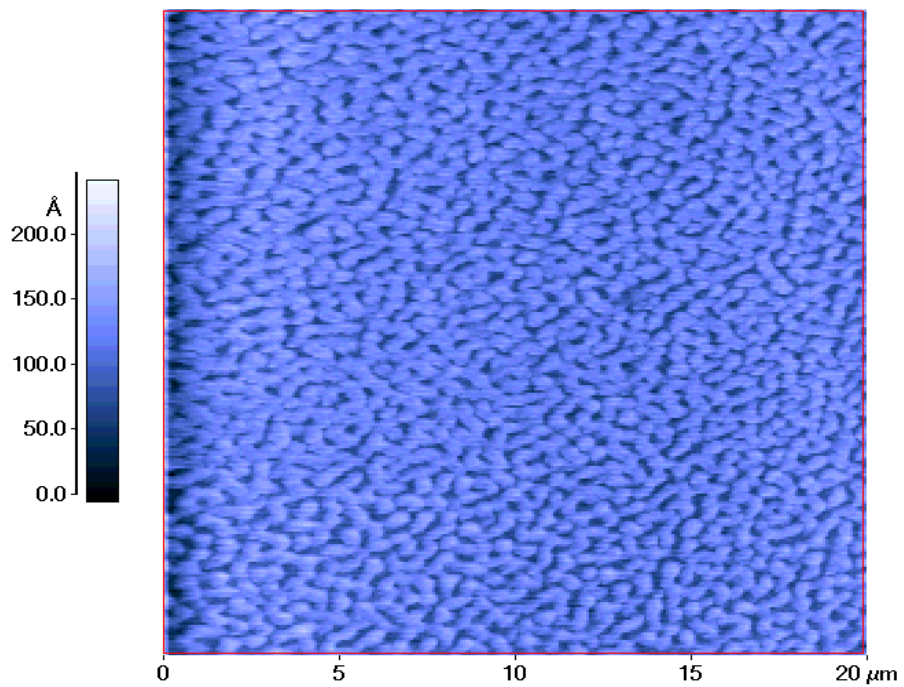


**Figure 3.1** AFM image of central part of drop-coated-square membrane using gold sputter coated mica as substrate



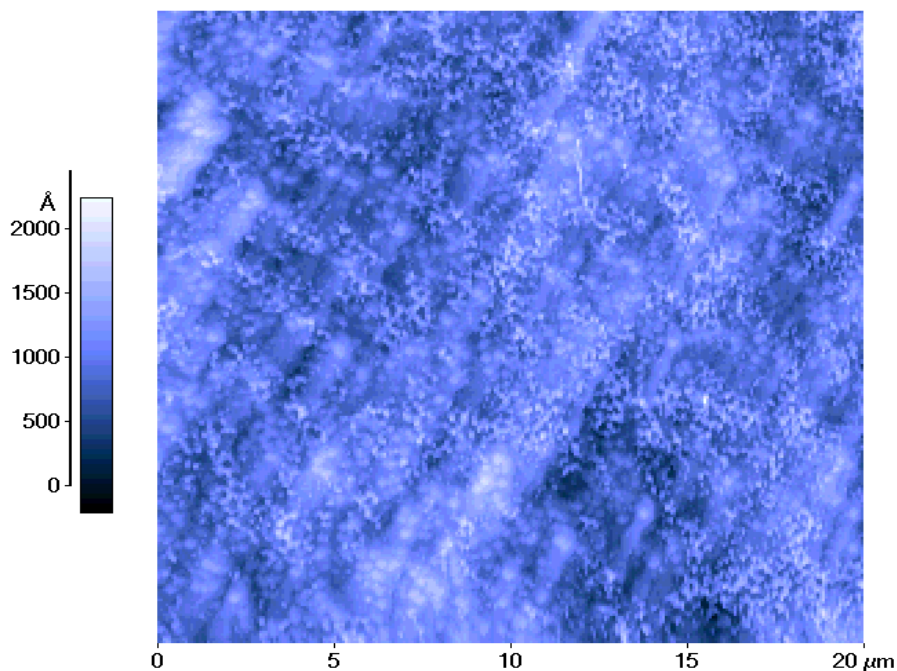
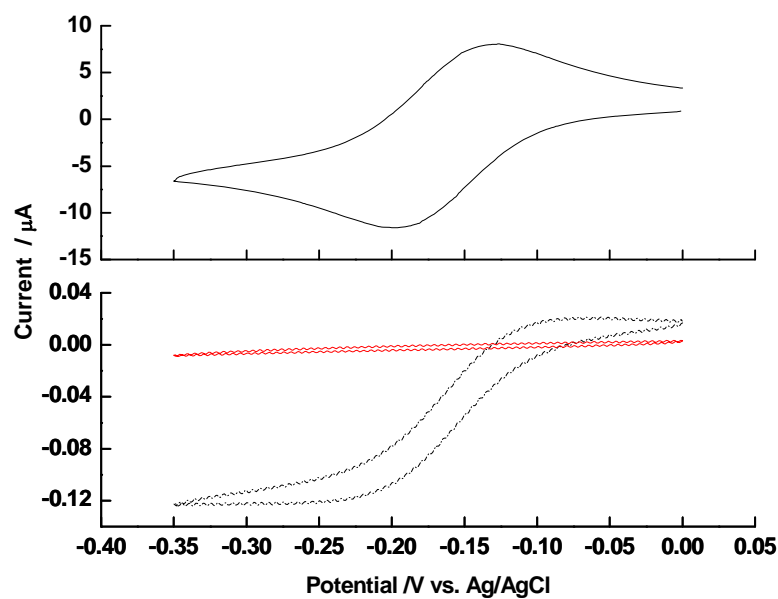


**Figure 3.2** AFM images of drop-coated-square membrane on top of alumina.

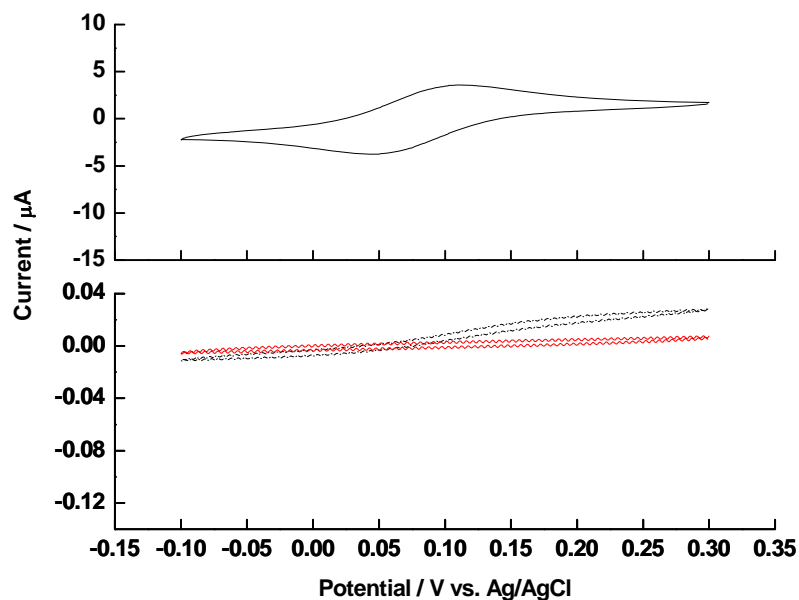
### 3.3.2 Solution Phase Sieving

Solution phase sieving was carried out based on the peak current recorded at different probe solutions when the scan rate is 50mV/s. Figure 3.3 shows the sieving results of  $\{[\text{RuCl}_2(\text{dppb})](\mu - \text{pz})_4\}$  based membrane. After the GC electrode is covered with film, the peak current decreases considerably compared to that of bare GC electrode. In addition, when the size of the probes increases, the peak current ratio decreases from 0.015 to 0.007 indicating the amount of  $\text{Ru}(\text{NH}_3)_6\text{Cl}_3$  diffused through the membrane is

more than that of the  $\text{Co}(\text{bpy})_3(\text{ClO}_4)_3$ . Indeed, the peak current in the  $\text{Co}(\text{bpy})_3(\text{ClO}_4)_3$  solution is almost undetectable. Figure 3.4 shows the sieving results of the  $\{[\text{RuCl}_2(\text{dppb})](\mu - 4,4'\text{-bipy})_4\}$  based membrane. Similar trends can be observed. The only difference is the peak current ratio does not decrease that much: in  $\text{Ru}(\text{NH}_3)_6\text{Cl}_3$  solution, the ratio is about 0.039 and in  $\text{Co}(\text{bpy})_3(\text{ClO}_4)_3$  solution, the ratio is about 0.033. This indicates that both probes can diffuse through the membrane with similar speed. Figure 3.5 is the sieving results of  $\{[\text{RuCl}_2(\text{dppb})](\mu - \text{AZP})_4\}$  based membrane which shows a current decrease ratio of 0.54 in  $\text{Ru}(\text{NH}_3)_6\text{Cl}_3$  solution and 0.4 in  $\text{Co}(\text{bpy})_3(\text{ClO}_4)_3$  solution, respectively. The peak current of the modified electrode in different probe solutions is summarized in Table 3.1. The data can be explained by size-selective effect. For  $\{[\text{RuCl}_2(\text{dppb})](\mu - \text{pz})_4\}$  based membrane, the size of probe  $\text{Ru}(\text{NH}_3)_6\text{Cl}_3$  is similar to the pore size of the membrane, therefore it can diffuse through; while the size of probe  $\text{Co}(\text{bpy})_3(\text{ClO}_4)_3$  is larger than the pore size of the membrane, it is blocked and can not go through. Since the size of  $\text{Ru}(\text{NH}_3)_6\text{Cl}_3$  and  $\text{Co}(\text{bpy})_3(\text{ClO}_4)_3$  are either smaller than or similar to the pore size of the  $\{[\text{RuCl}_2(\text{dppb})](\mu - 4,4'\text{-bipy})_4\}$ - and  $\{[\text{RuCl}_2(\text{dppb})](\mu - \text{AZP})_4\}$ - based membrane, both of them can go through the membrane. Interestingly, the sieving results from  $\{[\text{RuCl}_2(\text{dppb})](\mu - \text{AZP})_4\}$ - based membranes show slight selectivity towards  $\text{Ru}(\text{NH}_3)_6\text{Cl}_3$  indicating that affinity between probe molecules and membrane also plays a role in the process.

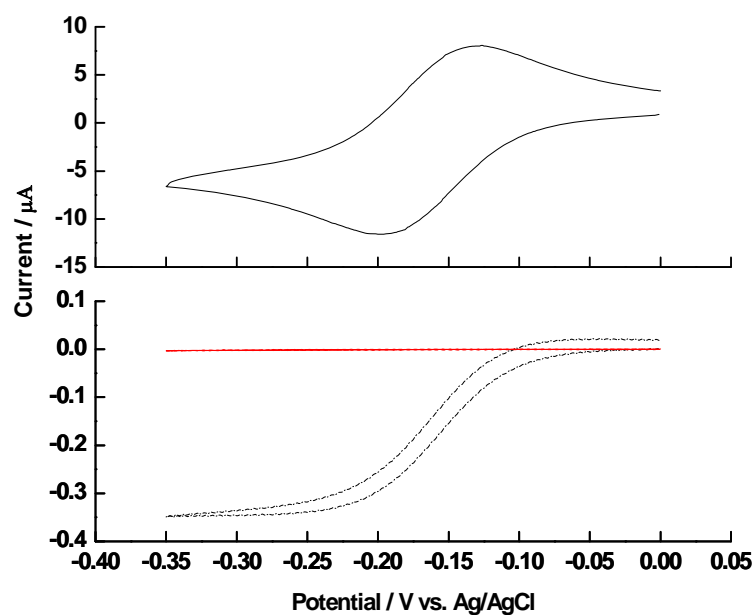


a

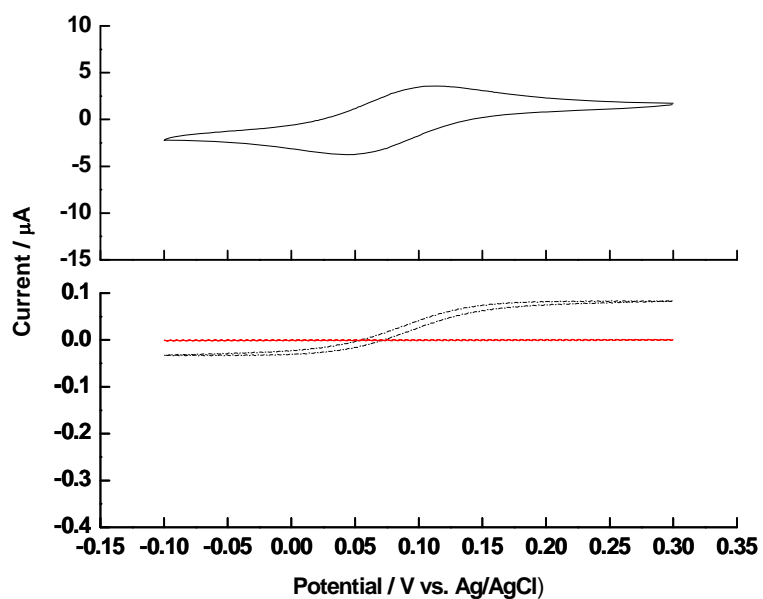


b

**Figure 3.3** Molecular sieving test with  $\{[\text{RuCl}_2(\text{dppb})](\mu\text{-pz})_4\}$  Film. Black solid: CV with bare electrode; Black dash: CV with electrode covered with film; a: test in 1mM  $\text{Ru}(\text{NH}_3)_6\text{Cl}_3$ ; b: test in 1mM  $\text{Co}(\text{bpy})_3(\text{ClO}_4)_3$ , The electrolyte is 0.1M  $\text{KNO}_3$ . Red: background current of the electrode covered with film. Scan rate in all cases in 50 mv/s.

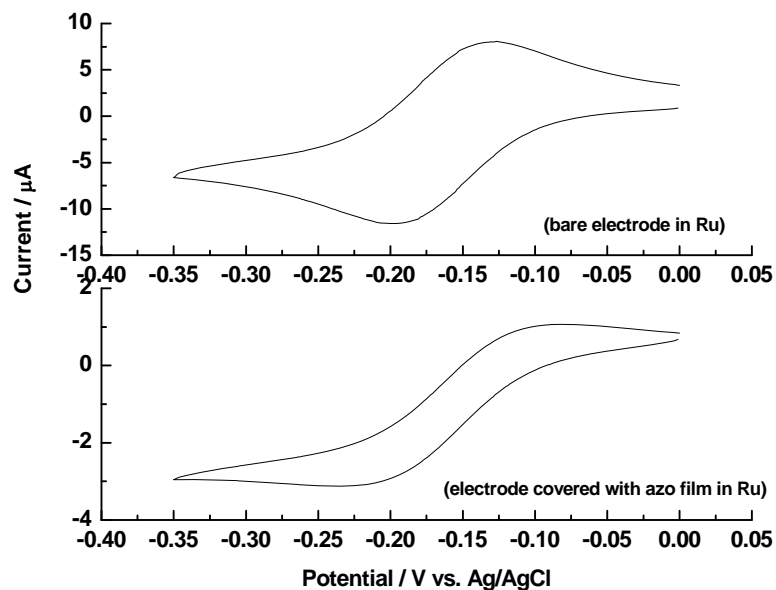


a

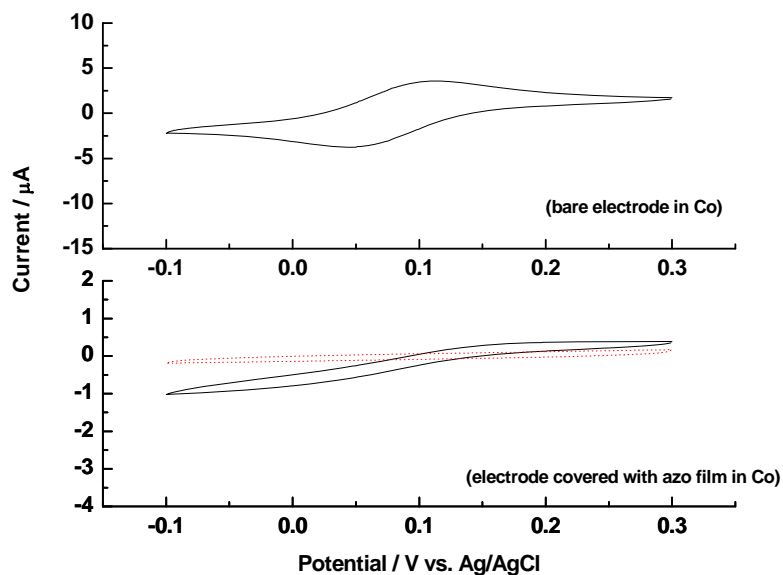


b

**Figure 3.4** Molecular sieving test with  $\{[\text{RuCl}_2(\text{appb})](\mu\text{-}4,4'\text{-bipy})_4\}$  Film. Black solid: CV with bare electrode; Black dash: CV with electrode covered with film; a: test in 1mM  $\text{Ru}(\text{NH}_3)_6\text{Cl}_3$ ; b: test in 1mM  $\text{Co}(\text{bpy})_3(\text{ClO}_4)_3$ , The electrolyte is 0.1M  $\text{KNO}_3$ . Red: background current of the electrode covered with film. Scan rate in all cases in 50 mv/s.



a



b

**Figure 3.5** Molecular Sieving Test with  $\{[\text{RuCl}_2(\text{dppb})](\mu\text{-AZP})_4\}$  Film. Black solid: CV with bare electrode; Black dash: CV with electrode covered with film; a: test in 1mM  $\text{Ru}(\text{NH}_3)_6\text{Cl}_3$ ; b: test in 1mM  $\text{Co}(\text{bpy})_3(\text{ClO}_4)_3$ , The electrolyte is 0.1M  $\text{KNO}_3$ . Red: background current of the electrode covered with film. Scan rate in all cases in 50 mv/s.

**Table 3.1** Summary of Sieving Results of {[RuCl<sub>2</sub>(dppb)](μ -N-N)}<sub>4</sub> Based Membrane ( μ -N-N = pz, bpy and AZP)

{[RuCl <sub>2</sub> (dppb)](μ-N-N)} <sub>4</sub>	Probe Molecule	I <sub>pb</sub> (μA)	I <sub>pf</sub> (μA)	I <sub>pf</sub> / I <sub>pb</sub>
{[RuCl <sub>2</sub> (dppb)](μ- pz)} <sub>4</sub>	Ru(NH <sub>3</sub> ) <sub>6</sub> Cl <sub>3</sub>	9.31	0.14	0.015
	Co(bpy) <sub>3</sub> (ClO <sub>4</sub> ) <sub>3</sub>	3.62	0.025	0.007
{[RuCl <sub>2</sub> (dppb)](μ-4,4'-bipy)} <sub>4</sub>	Ru(NH <sub>3</sub> ) <sub>6</sub> Cl <sub>3</sub>	9.31	0.37	0.039
	Co(bpy) <sub>3</sub> (ClO <sub>4</sub> ) <sub>3</sub>	3.62	0.12	0.033
{[RuCl <sub>2</sub> (dppb)](μ-AZP)} <sub>4</sub>	Ru(NH <sub>3</sub> ) <sub>6</sub> Cl <sub>3</sub>	9.31	5.04	0.54
	Co(bpy) <sub>3</sub> (ClO <sub>4</sub> ) <sub>3</sub>	3.62	1.43	0.40

\*I<sub>pb</sub> is the peak current of the bared GC electrode

I<sub>pf</sub> is the peak current of the GC electrode covered with molecular square film

### 3.3.3 Gas Phase Separation

Table 3.2 shows the separation results of benzene and toluene. The feed ratio and permeate ratio were directly calculated from the integration of the benzene and toluene peaks. All the data shown were collected when the system reached equilibrium. As alumina was used as membrane support, a comparison experiment with only alumina membrane was conducted, which yielded 1.07 ratio of permeate over feed. When alumina was covered with {[RuCl<sub>2</sub>(dppb)](μ - 4,4'-bipy)}<sub>4</sub>, the ratio lowered to 0.87, indicating the percentage of benzene in the permeate site decreased, that is, toluene permeated faster than benzene did. On the third run, the alumina was covered with {[RuCl<sub>2</sub>(dppb)](μ - pz)}<sub>4</sub>. The ratio of permeate over feed decreased further, which means benzene has a stronger interaction with {[RuCl<sub>2</sub>(dppb)](μ - pz)}<sub>4</sub> than {[RuCl<sub>2</sub>(dppb)](μ - 4,4'-bipy)}<sub>4</sub>. Table 3.3 shows the results of separating benzene and cyclohexane. In this case, benzene permeated faster relative to cyclohexane since the percentage of benzene increased after permeation. Also, with the porosity of the membrane decreasing, the ratio of permeate over feed kept increasing suggesting {[RuCl<sub>2</sub>(dppb)](μ - pz)}<sub>4</sub> has stronger interaction

with cyclohexane than  $\{[\text{RuCl}_2(\text{dppb})](\mu - 4,4'\text{-bipy})\}_4$ .

**Table 3.2** Separation of benzene and toluene

Membrane material	Feed ratio ( $A_b/A_t$ )	Permeate ratio ( $A_b/A_t$ )	Ratio of permeate over feed
Alumina	10.83	11.56	1.07
Alumina+ bipy based square	9.87	8.61	0.87
Alumina+pyrazine based square	14.26	5.32	0.37

**Table 3.3** Separation of benzene and cyclohexane

Membrane material	Feed ratio ( $A_b/A_c$ )	Permeate ratio ( $A_b/A_c$ )	Ratio of permeate over feed
Alumina	1.46	2.25	1.54
Alumina+ bipy based square	1.55	2.74	1.77
Alumina+pyrazine based square	1.44	2.98	2.07

\* A is integrated area of relevant peak

From the above data, it can be concluded that a  $\{[\text{RuCl}_2(\text{dppb})](\mu - \text{pz})\}_4$ - based membrane has the best separation in both cases. This can be explained by size selective. If the porosity of the membrane is smaller, then interaction with permeates is stronger. In addition, by comparing permeation data of  $\{[\text{RuCl}_2(\text{dppb})](\mu - \text{pz})\}_4$ - based membrane with the ratio of binding constant of previous study<sup>13</sup> as shown in Table 3.4, it can be seen that the  $\alpha$  value calculated from our experiment is very close to the adsorption data of  $\{[\text{ReCl}_2(\text{CO})_3](\mu - \text{pz})\}_4$ - based membranes, which suggests affinity also plays an important role in the gas transportation process.

**Table 3.4** Comparison of permeation data of {[RuCl<sub>2</sub>(dppb)](μ -pz)}<sub>4</sub> based membrane with previous study

Compound	K <sub>bind</sub> (M <sup>-1</sup> )	K <sub>b</sub> /K <sub>i</sub> (i=c or t)	α <sub>b/i</sub> (i= c or t)
Cyclohexane	58	2.7	2.1
Benzene	157	1	N/A
Toluene	332	0.47	0.37

### 3.4 Conclusions

{[RuCl<sub>2</sub>(dppb)](μ -N-N)}<sub>4</sub> (μ -N-N=pz, bipy and AZP)- based nanoporous membranes were fabricated and characterized by AFM. This proved that layer by layer membrane formation could effectively prevent severe defects. The permeation study was carried out in solution phase and gas phase. In the solution phase, the separation mainly contributed to size selective effects and in the gas phase, affinity played an important role in the separation process as well as size selectivity. In addition, Crystal structures of molecular squares could not account for the transportation study, since the membrane was in amorphous phase. Therefore, more work needs to be done regarding intra and/or inter molecular transportation.

### 3.5 References

1. Lin, H.; Wagner, E. v.; Freeman, B. D.; Roman, I., *Adv. Mater.* **2006**, 18, 39-44.
2. Prabhaker, R. S.; Freeman, B. D.; Roman, I., *Macromolecules* **2004**, 37, 7688-7697.
3. Budd, P. M.; Msayib, K. J.; Tattershall, C. E., *J. Membr. Sci.* **2005**, 251, 263-269.
4. Tang, J.; Tang, H.; Sun, W., *Chem. Commun.* **2005**, 3325-3327.
5. Ma, Y. H.; Akis, B. C.; Ayturk, M. E.; Guazzone, F.; Engwall, E. E.; Mardilovich, I. P., *Ind. Eng. Chem. Res.* **2004**, 43, 2936.



6. Gu, X.; Zhang, J.; Dong, J.; Nenoff, T. M., *Catal. Lett.* **2005**, 102, 9-13.
7. Abidi, N.; Sivade, A.; Bourret, D.; Larbot, A.; Boutevin, B.; Guida-Pietrasanta, F.; Ratsimihety, A., *J. Membr. Sci.* **2006**, 270, (1-2), 101-107.
8. Czaplewski, K. F.; Hupp, J. T.; Snurr, R. Q., *Adv. Mater.* **2001**, 13, (24), 1895-1897.
9. Zhang, J.; Williams, M. E.; Keefe, M. H., *Electrochem. Solid-State Lett.* **2002**, 5, (5), E25-E28.
10. Williams, M. E.; Benkstein, K. D.; Abel, C., *PNAS* **2002**, 99, (8), 5171-5177.
11. Keefe, M. H.; Slone, R. V.; Hupp, J. T., *Langmuir* **2000**, 16, 3964-3970.
12. Queiroz, S. L.; Kirkuti, E.; Ferreira, A. G.; Santlago, M. O.; Batista, A. A.; Castellano, E. E.; Ellena, J., *Supramol. Chem.* **2004**, 16, (4), 255-262.
13. Czaplewski, K. F.; Li, J.; Hupp, J. T.; Snurr, R. Q., *J. Membr. Sci.* **2003**, 221, 101-111.
14. Belanger, S.; Hupp, J. T., *Angew. Chem. Int. Ed.* **1999**, 38, (15), 2222-2224.
15. Burstall, F. H.; Nyholm, R. S., *J. Chem. Soc.* **1952**, 3570.

**CHAPTER FOUR**

**POLYTHIOOXOMETALATE-ENCAPSULATED HYDROQUINONES:  
SYNTHESIS, CHARACTERIZATION AND ELECTROCHEMISTRY**

**4.1 Introduction**

Polyoxometalates are an important class of supramolecular materials with a wide range of applications. Owing to the ability to tune contact surfaces with the solvents to idealize the entropy value of solvent interactions,<sup>1</sup> large ring and ball shaped POMs can be prepared with good solubility. A good example is Mo<sub>368</sub> prepared by Müller with a diameter  $\approx 2.5 \times 4.0$  nm cavity.<sup>2</sup> Many of these ring and ball shaped POMs resemble organic crown ethers or clathrates that can host different size anions, and thus be used for anion recognition, ion transport, and building 3D structures. Soluble vanadium oxides were the first reported inorganic hosts,<sup>3-6</sup> and following that, tungsten and molybdenum based inorganic hosts were developed. A review from Müller summarized the basic concepts of inorganic host-guest chemistry and host-guest properties of some polyoxometalates.<sup>7</sup>

For the purpose of designing diverse polyoxometalates with different properties, sulfur was considered a potential substitute for oxygen; however, large polythiometalate clusters are very rare, giving rise to the low nuclearity of thiometalates. Cadot's group pioneered the work in this area. They successfully synthesized the wheel shaped

polythiooxometalate  $[\text{Mo}_{12}\text{S}_{12}\text{O}_{12}(\text{OH})_{12}(\text{H}_2\text{O})_6]$ .<sup>8</sup> Then, by introducing anions to the building blocks, a series of polythiooxometalate encapsulated complexes can be isolated in a solid state. Anions have been incorporated so far, including alkyl based dicarboxylate,<sup>9, 10, 11</sup> tricarboxylate,<sup>12</sup> phosphate,<sup>13, 14</sup> Arsenate<sup>15</sup> and iodide anions<sup>16</sup>.

There are two main features of these polythiooxometalate systems. The first feature is the templating effect of the encapsulated anions; POM complexes with various shapes and sizes can be formed by introducing anions of different sizes and shapes. Good examples are linear dicarboxylate anion templated complexes. With the increase of the alkyl chain length from oxalate ( $\text{C}_2\text{O}_4^{2-}$ ) to glutarate ( $\text{H}_6\text{C}_5\text{O}_4^{2-}$ ) and to pimelate ( $\text{H}_{10}\text{C}_7\text{O}_4^{2-}$ ) anions, the size of the templated complexes also keep increasing from  $[\text{Mo}_8\text{-ox}]^{2-}$  to  $[\text{Mo}_{10}\text{-glu}]^{2-}$  to  $[\text{Mo}_{12}\text{-pim}]^{2-}$ . The second feature is the lability of the complexes. The  $^1\text{H}$  NMR at various temperatures reveals that for some complexes, such as  $[\text{Mo}_{10}\text{-glu}]^{2-}$  or  $[\text{Mo}_{12}\text{-pim}]^{2-}$ , there is a hopping effect of the terminal carboxylate groups over the nearby molybdenum atoms at room temperature. This is attributed to the flexibility of MoV coordination which can take either octahedral or square pyramidal geometry. In contrast to this, such an effect is not observed for  $[\text{Mo}_8\text{-ox}]^{2-}$  since all the molybdenum atoms are in an octahedral environment. The lability of the system was also illustrated by the exchange of the encapsulated anions with the environment, either with the solvent molecules or other substituting molecules at certain concentrations.  $^{31}\text{P}$  NMR at various concentrations and various temperatures provides a powerful way to study the thermodynamics of and generate robust nanostructured materials. Some applications using these synthesized supramolecular assemblies have been proven to be very successful. phosphate templated complexes, and there is further indication that there is an

equilibrium between  $[(\text{HPO}_4)_2\text{Mo}_{12}\text{S}_{12}\text{O}_{12}(\text{OH})_{12}(\text{H}_2\text{O})_2]^{4-}$  and  $[(\text{HPO}_4)\text{Mo}_{10}\text{S}_{10}\text{O}_{10}(\text{OH})_{10}(\text{H}_2\text{O})_3]^{2-}$  when the concentration is below  $0.5 \text{ mole}\cdot\text{L}^{-1}$ . This equilibrium can be expressed as follows:



When the solution becomes more concentrated,  $[(\text{HPO}_4)_4\text{Mo}_6\text{S}_6\text{O}_6(\text{OH})_3]^{5-}$  anions are produced. In the presence of arsenate, hydrogen phosphate undergoes an exchange with the arsenate anions and forms  $[(\text{HAsO}_4)_4\text{Mo}_6\text{S}_6\text{O}_6(\text{OH})_3]^{5-}$ . Quantitative analysis further indicates that the relative affinity of substituting groups toward the coordination sites are related to their acidity constants. The lability of the system is a very attractive feature in view of the host-guest interaction and sensor development, which allows the sensing material to be easily tuned by external perturbation.

The breakthrough of the work in this area is the extension to tungsten substituted polythioxometalate. However the complexes built on  $[\text{W}_2\text{S}_2\text{O}_2]^{2-}$  moieties are very limited, and so far only  $\text{Cs}_4[\text{W}_{16}\text{S}_{16}\text{O}_{16}(\text{OH})_{16}(\text{H}_2\text{O})_4(\text{C}_5\text{H}_6\text{O}_4)_2]$ <sup>17</sup> and  $\text{Rb}_3[\text{W}_8\text{S}_8\text{O}_8(\text{OH})_8(\text{H}_3\text{WO}_6)]$ <sup>18</sup> have been reported. Here we report another case using  $[\text{W}_2\text{S}_2\text{O}_2]^{2-}$  as building blocks with hydroquinone as templates. To form covalent bonds between the hydroquinone molecules and the POM backbone, 2,5-Dihydroxy-1,4-benzenediacetic acid is used in this study, and its structure is shown in Figure 4.1.

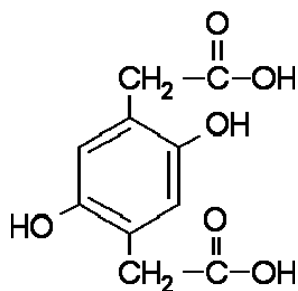
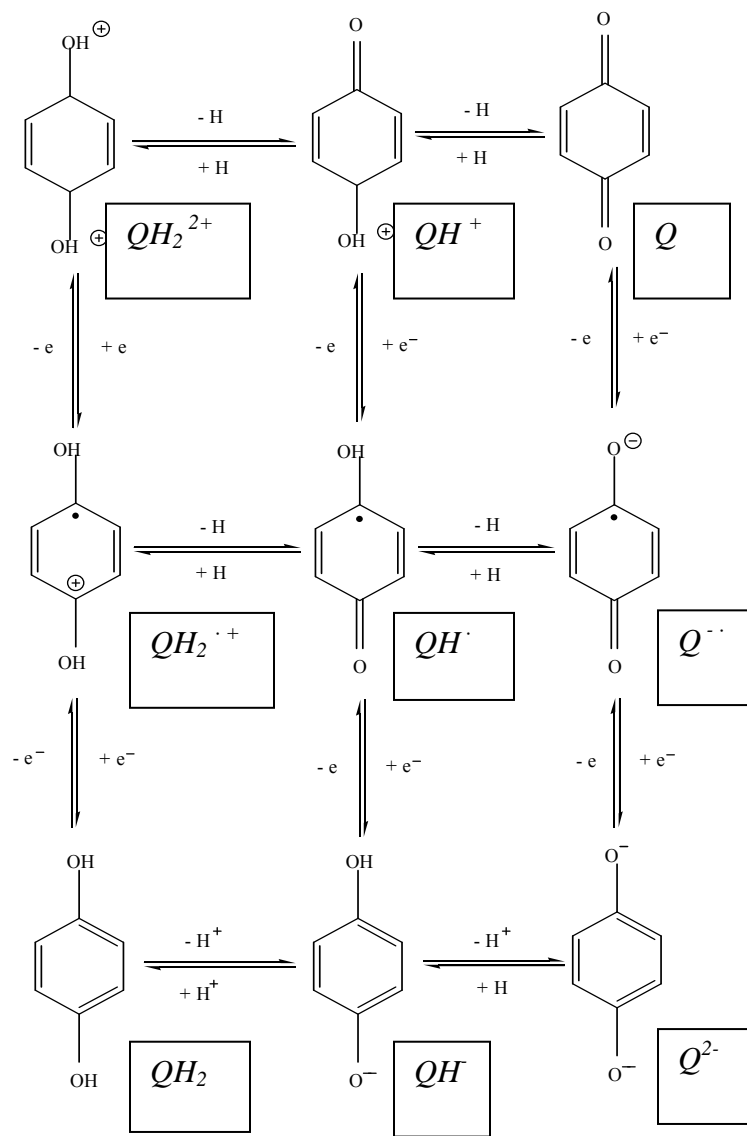


**Figure 4.1** Molecular structure of 2,5-Dihydroxy-1,4-benzenediacetic acid

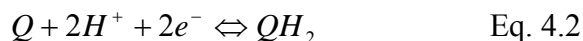
There are two main reasons for considering hydroquinone as a template. The first is that hydroquinone is an important electron-proton transfer agent in electrochemistry. When it is introduced to a polythioxometalate system, electrochemical information can now be obtained, even though no other electrochemistry study on these supramolecules has been reported so far. The electrochemical behaviors of hydroquinone-quinone couples have been well established and their reaction pathways follow the nine-membered scheme<sup>19, 20</sup> as shown in scheme 4.1.



**Scheme 4.1** Reaction pathways for the oxidation of hydroquinone

Depending on the electrode type used, the solvent and other perturbation factors, the dominating pathway of the reaction  $Q \Leftrightarrow QH_2$  differs. The following describes the general electrochemical behavior of the hydroquinone system in different solvent media:

(1) In well-buffered aqueous media (including mixtures with ethanol, dioxane, etc.), quinone-hydroquinone couples undergo reversible two-electron oxidation or reduction process shown in equation 4.2.



Where  $Q$  is p-benzoquinone, and  $QH_2$  is hydroquinone. The polarographic potentials of the reaction show pH dependence and follow a straightforward Nernstian behavior. <sup>21, 22</sup>E-pH (Pourbaix) diagrams was generated to summarize this behavior with regions of various redox and protonated species as well as their respective pK<sub>a</sub> values.<sup>20, 23, 24</sup>

(2) In dry, neutral, aprotic media, semiquinone anions can be detected and quinones show typical two consecutive one-electron cathodic polarographic waves, E<sub>1</sub> and E<sub>2</sub>, separated by about 70 mV.



In these reductions, the first step is generally reversible and the second is at least quasi-reversible at normal scan rate. Many factors can affect these reduction potentials such as solvent polarity,<sup>25-28</sup> supporting electrolyte,<sup>20, 23, 29-32</sup> and the use of acidic additives, that are related to nonspecific solvation energies, ion-pairing, and protonation equilibria,<sup>33</sup> respectively.

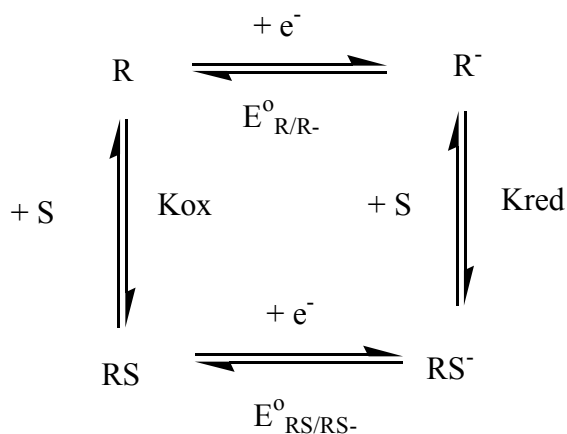
(3) In unbuffered aqueous media, the mechanism for the reduction of p-benzoquinone is disputable. Earlier studies showed that p-benzoquinone reduction in neutral unbuffered aqueous solution underwent a two-electron transfer and two-proton transfer process as shown in equation 1.<sup>34-36</sup> The study by Bailey and Ritchie indicated that “local effective pH” played an important role in the electrochemical process.<sup>24</sup> In

neutral unbuffered solution, when p-benzoquinone is reduced, the pH in the reaction layer of the solution near the electrode surface will be increased by an amount determined by the concentration of the quinone due to the consumption of protons. Likewise, the oxidation of hydroquinone will produce protons and hence decrease the local pH to an extent based on the amount of hydroquinone reacted. According to the E-pH curve in the buffered solution, the half wave potential of hydroquinone will be more positive than the half wave potential of p-benzoquinone in unbuffered solution. If small quantities of  $H^+$  or  $OH^-$  are added to the unbuffered solution, in which the concentration of added  $H^+$  or  $OH^-$  is comparable to or less than the amount consumed or produced by the reaction, the previously described single peak will split into two peaks. Again, it is the local effective pH effect, and the reaction of a substantial fraction of quinone/hydroquinone will happen the same way as in buffered solution, which results in the peak determined by the “apparent pH”. Upon depleting the available  $H^+$  or  $OH^-$ , another peak appears as the remainder of the quinone/hydroquinone reacts which is analogous to the neutral unbuffered situation. When the concentration of  $H^+$  or  $OH^-$  becomes considerably in excess of the concentration of active species, the quinone’s behaviour approaches that in buffered solution. These explanations sound reasonable, however a later study done by Tang et. al. suggested the existence of p-benzoquinone anion radical during the reduction of p-benzoquinone in unbuffered solution at pH 3 to 5 using ESR and transmission UV-Vis measurements.<sup>37</sup> The p-benzoquinone anion radical is not formed by directly one-electron reduction of p-benzoquinone, but the product of comproportionation reaction of p-benzoquinone dianion and parent p-benzoquinone.



The second reason for using hydroquinone as the templating molecule is that quinoid compounds can be used as “redox dependent” receptors. A receptor is defined as the compound that selectively binds to another substance (substrate) through a variety of weak interactions such as hydrogen binding, ion pairing or by Van der Waals force. A “redox-dependent receptor” refers to the compound whose binding strength to a particular substrate changes upon reduction or oxidation of the receptor. In such conditions and also when the redox process is reversible, the redox potential shift of the receptor will be observed in the presence of the substrate. The value of the potential shift can relate to the concentration of the substrate even though the substrate itself may not be electroactive. This provides an easy electrochemical way to study the host guest chemistry instead of NMR or Spectroscopy which requires sophisticated instrumentation.

The equilibrium involved in the redox dependent receptor-substrate binding is illustrated in scheme 4.2, where  $K_{ox}$  is the binding constant of the oxidized form and  $K_{red}$  is the binding constant of the reduced form.



**Scheme 4.2** redox dependent receptor-substrate binding equilibrium scheme

If  $K_{ox} > K_{red}$ , in which the substrate S binds to the oxidized form of the receptor R more strongly, then the reduction of R becomes harder and a negative shift of the redox potential of R will be observed; on the other hand, if  $K_{red} > K_{ox}$ , in which S binds to the reduced form R more strongly, then the reduction of R becomes easier and a positive shift of redox potential of R will occur. Assuming access substrate concentration, application of the Nernst equation and the equilibrium constant expressions yields equation 4.4.<sup>38,39</sup>

$$\Delta E' = \frac{0.0592V}{n} \log\left(\frac{1 + K_{red}[S]}{1 + K_{ox}[S]}\right) \quad \text{Eq. 4.4}$$

This equation predicts that the redox potential of R will respond to S over a certain concentration range from  $1/K_{red}$  to  $1/K_{ox}$ . Inside this range there will be a region where the redox potential will follow the Nernstian behavior, that is, a 60 mV/n change in potential per  $\log[S]$ . Also from the equation 4.4, the maximum shift can be derived:

$$\Delta E_{\max} = \frac{59.2mV}{n} \log\left(\frac{K_{red}}{K_{ox}}\right) \quad \text{Eq. 4.5}$$

The redox potential shift resulting from binding is commonly observed in transition metal-ligand systems.<sup>40</sup> In the 1980s, the concept was extended to organic hosts. Redox-active crown ethers were prepared by a couple of groups and large redox potential changes were observed in the presence of alkali metal cations.<sup>41</sup> Later the work in this area extended to host anions<sup>42</sup> and neutral compounds<sup>43</sup>. For ionic compounds, the static interactions play an important role and for the neutral compounds, the hydrogen bonding controls the process. Since organic compound templated polyoxothiomallate represents another unique host-guest system, it should be interesting to study whether such a redox potential shifting behavior exist.

## 4.2 Experimental

**4.2.1 Chemicals:**  $(\text{NH}_4)_2\text{WS}_4$  (Alfa Aesar), sulfur (99.999%, Alfa Aesar),  $(\text{CH}_3)_4\text{NCl}$  (Alfa Aesar), DMF (anhydrous, sigma-aldrich) were used as received.  $\text{C}_{10}\text{H}_{10}\text{O}_6$  (sigma-aldrich) was recrystallized according to literature before use<sup>44-46</sup>,  $(\text{NMe}_4)_2[\text{W}_2\text{O}_2\text{S}_{10}]$  was prepared according to reference<sup>47</sup>.

**4.2.2 Synthesis:** The synthesis following Cadot's recipe (reference<sup>17</sup>):  $(\text{NMe}_4)_2[\text{W}_2\text{O}_2\text{S}_{10}]$  (0.5g) was dissolved in N, N-dimethylformamide (5mL) followed by dropwise adding Iodine (0.293g) in N, N-dimethylformamide (2.5mL) to the solution while stirring. After the mixture was stirred for 60 minutes at room temperature, the resulting mixture was clarified by filtration and the deep red solution was cooled to 0 °C. 2,5-dihydroxy-1,4-benzenediacetic acid,  $(\text{C}_{10}\text{H}_8\text{O}_6)$  (0.145g) was suspended in distilled water (7mL), and by titrating NaOH ( $1\text{mol}\cdot\text{L}^{-1}$ ), the suspension was turned into clear slightly yellow solution. Continue adding NaOH until the pH was adjusted to 5. The deep red solution was then slowly added into the 2,5-Dihydroxy-1,4-benzenediacetic acid solution and the PH was maintained at 5 by dropwise adding NaOH. The resulting insoluble material was removed by filtration and CsCl (0.5g) was added to the filtrate. With mild stirring, the yellow crude product was precipitated, collected by filtration, and washed with ethanol and diethyl ether. Crystals were grown from water and ethanol. 20mg of crude product was dissolved in 2 ml water and the solution was heated until the entire complex dissolved. After the solution cooled down, insoluble material was removed by filtration. Ethanol was added to the clear filtrate drop by drop until the solution becomes cloudy. The solution was sealed and crystals grew after several days. Elemental analysis calculated (%): Cs 10.05, W 55.65, S 9.68; found: Cs 9.07, W 55.92, S 10.30.

### 4.2.3 Instrumentation

*Crystallography:* The single crystal was first introduced into paratone oil to prevent any water loss and mounted on a glass fiber and optically aligned on a Bruker APEX CCD X-ray diffractometer using a digital camera. Initial intensity measurements were performed using graphite-monochromated  $\text{Mo}_{\text{K}\alpha}$  radiation ( $\lambda = 0.71073 \text{ \AA}$ ) from a sealed tube and monocapillary collimator at 193K. SMART (v 5.624) was used for preliminary determination of the cell constants and data collection control. The intensities of reflections of a sphere were collected by a combination of three sets of exposures (frames). Each set had a different  $\phi$  angle for the crystal, and each exposure covered a range of  $0.3^\circ$  in  $\omega$ . A total of 1800 frames were collected with an exposure time per frame of 30 s.

Determination of integrated intensities and global refinement were performed with the Bruker SAINT (v 6.02) software package using a narrow-frame integration algorithm. These data were treated with a semiempirical absorption correction by SADABS.<sup>48</sup> The program suite SHELXTL (v 6.12) was used for space-group determination (XPREP)<sup>48</sup>, direct methods structure solution (XS), and least-squares refinement (XL).<sup>49</sup> The final refinements included anisotropic displacement parameters for all atoms and secondary extinction. The crystal and refinement data are summarized in Table 4.1, and selected distances and angles are shown in Table 4.2.

*Elemental Analysis:* Elemental composition of the crystal was collected on six different spots with energy-dispersive X-ray spectrometer coupled to a field emission scanning electron microscope (JEOL JSM-7001F).

*Raman Measurements:* Raman spectra of crystals were collected with a Renishaw inVia Raman Microscope using 785nm laser excitation for 10s exposure at 10 % output power; SERS was measured under similar experimental conditions expect that the output power is set 100%.

*NMR Measurements:* Proton NMR spectrum was collected on a Bruker AM400 multinuclear NMR.

*Electrochemistry Measurements:* All the measurements were performed in aqueous solution containing 0.1M NaClO<sub>4</sub> as electrolyte. A standard three-electrode, one-compartment cell was employed. The working electrode was a 3 mm diameter glassy carbon electrode. The reference and counter electrode were Ag/AgCl and platinum gauge, respectively. Epsilon Potentiostat from BASi was employed.

**Table 4.1.** Crystallographic Data and Structure Refinement Details

Empirical Formula	C <sub>10</sub> H <sub>34</sub> Cs <sub>2</sub> O <sub>31</sub> S <sub>8</sub> W <sub>8</sub>
Empirical Formula Weight	2643.16
Temperature	193 (2) K
Wavelength	0.71073 Å
Crystal System	Monoclinic
Space Group	P2 <sub>1</sub> /c
Unit Cell Dimensions	a. 13.5028(8) Å, α = 90.00 b. 23.3667(14) Å, β = 105.0210(10) c. 19.5610(12) Å, γ = 90.00
V	5960.9(6) Å <sup>3</sup>
Z	4
Density (calculated)	2.926 mg·m <sup>-3</sup>
Absorption Coefficient	16.898 mm <sup>-1</sup>
F(000)	4599
Crystal Size	0.430 × 0.110 × 0.021 mm <sup>3</sup>
θ Range for Data Collection	1.39 to 28.31°
Index Ranges	-17 ≤ h ≤ 17, -31 ≤ k ≤ 31, -26 ≤ l ≤ 26
Reflections Collected	60046
Independent Reflections	14800, [R(int) = 0.0409]
Completeness to theta = 28.31 °	99.80%
Max and Min transmission	0.44981 and 0.08246
Data/Restraints/Parameters	14800 /0/578
Goodness-of-Fit on F <sup>2</sup>	0.982
R (F) <sup>a</sup>	0.0449
R <sub>w</sub> (F <sub>o</sub> <sup>2</sup> ) <sup>b</sup>	0.1539

$$^a R(F) = \frac{\sum \|F_o\| - |F_c\|}{\sum |F_o|} \quad \text{for } F_o^2 > 2\delta(F_o^2)$$

$$^b R_w(F_o)^2 = \left[ \frac{\sum [w(F_o^2 - F_c^2)^2]}{\sum wF_o^4} \right]^{1/2}$$

**Table 4.2.** Selected Bond Distances (Å) and Angles (deg)

Bond distances (Å)					
W1—O11	1.715(8)	W4—S4	2.330(3)	W8—O7	2.063(7)
W1—O7	2.076(7)	W4—O52	2.504(9)	W8—O8	2.092(8)
W1—O8	2.086(8)	W5—O51	1.697(9)	W8—O82	2.329(8)
W1—O12	2.272(8)	W5—O3	2.089(8)	W8—S8	2.333(3)
W1—S1	2.334(3)	W5—O4	2.095(7)	W8—S7	2.350(3)
W1—S2	2.336(3)	W5—O52	2.317(8)	O82—C1	1.252(12)
W1—W2	2.818(6)	W5—S6	2.328(3)	C1—C2	1.515(15)
W2—O21	1.716(8)	W5—S5	2.342(3)	C2—C3	1.470(18)
W2—O1	2.073(8)	W5—W6	2.797(6)	C3—C8	1.347(19)
W2—O2	2.091(8)	W6—O61	1.713(8)	C3—C4	1.417(18)
W2—O22	2.297(9)	W6—O6	2.045(8)	C4—C5	1.379(19)
W2—S1	2.326(3)	W6—O5	2.081(7)	C4—O1L	1.391(18)
W2—S2	2.339(3)	W6—S6	2.329(3)	C5—C6	1.383(17)
W3—O31	1.694(8)	W6—S5	2.331(3)	C6—C7	1.369(17)
W3—O1	2.037(8)	W6—O62	2.395(8)	C6—C9	1.518(17)
W3—O2	2.071(7)	W7—O71	1.715(8)	C7—O2L	1.414(16)
W3—S3	2.316(3)	W7—O5	2.083(8)	C7—C8	1.429(18)
W3—S4	2.324(3)	W7—O6	2.088(8)	C9—C10	1.494(16)
W3—W4	2.805(6)	W7—O72	2.309(8)	O52—C10	1.266(14)
W4—O41	1.693(9)	W7—S8	2.333(3)	O62—C10	1.283(14)
W4—O4	2.067(7)	W7—S7	2.349(3)	O12—C1	1.248(13)
W4—O3	2.069(8)	W7—W8	2.8155(6)		
W4—S3	2.315(3)	W8—O81	1.725(8)		

Angles (deg)					
O11—W1—O7	96.5(4)	O8—W1—S2	90.5(2)	O12—C1—O82	125.3(10)
O11—W1—O8	95.0(4)	O12—W1—S2	83.5(2)	O12—C1—C2	116.1(9)
O7—W1—O8	70.8(3)	S1—W1—S2	104.8(10)	O82—C1—C2	118.5(10)
O11—W1—O12	173.0(3)	O11—W1—W2	99.9(3)	C5—C4—O1L	125.2(12)
O7—W1—O12	77.9(3)	O7—W1—W2	140.0(2)	O1L—C4—C3	114.4(12)
O8—W1—O12	79.3(3)	O8—W1—W2	142.4(2)	C6—C7—O2L	116.2(11)
O11—W1—S1	100.8(3)	O12—W1—W2	87.1(19)	O2L—C7—C8	121.9(12)
O7—W1—S1	88.6(2)	S1—W1—W2	52.7(7)	O52—C10—O62	123.9(10)
O8—W1—S1	155.4(2)	S2—W1—W2	53.0(7)	O52—C10—C9	116.5(11)
O12—W1—S1	83.4(2)	O21—W2—O22	170.2(3)	O62—C10—C9	119.6(10)
O11—W1—S2	100.6(3)	O1—W2—O22	76.2(3)		
O7—W1—S2	155.7(2)	O2—W2—O22	74.6(3)		

## 4.3 Results and Discussion

### 4.3.1 Synthesis

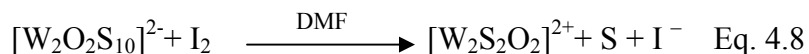
The entire synthesis starts from tetrathiotungstate  $[\text{WS}_4]^{2-}$ . In the presence of excess oxidizing agent sulfur, it forms dinuclear species  $[\text{W}_2\text{S}_{12}]^{2-}$  quantitatively in DMF at 110 °C as shown in equation 4.6.



Then the terminal sulfur of  $[\text{W}_2\text{S}_{12}]^{2-}$  can be selectively substituted by water and produce  $[(\text{S}_4)\text{WO}(\mu_2\text{-S})_2\text{WO}(\text{S}_4)]^{2-}$  as shown in equation 4.7.



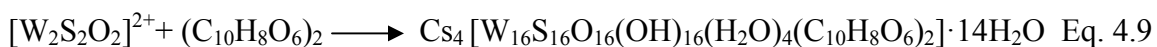
The synthesis of building block  $[\text{W}_2\text{S}_2\text{O}_2]^{2+}$  follows the procedure described by Coucouvanis in which the terminal  $(\text{Sn})^{2-}$  ligands of  $[(\text{S}_4)\text{WO}(\mu_2\text{-S})_2\text{WO}(\text{S}_4)]^{2-}$  ( $[\text{W}_2\text{O}_2\text{S}_{10}]^{2-}$ ) was selectively oxidized by iodine in DMF<sup>50, 51</sup> shown in equation 4.8. This protocol, initially designed for  $[\text{Mo}_2\text{S}_2\text{O}_2]^{2+}$ , works for  $[\text{W}_2\text{S}_2\text{O}_2]^{2+}$  as well. The only difference is the reaction media: the  $[\text{Mo}_2\text{S}_2\text{O}_2]^{2+}$  can be synthesized in either water or DMF. However, the formation of  $[\text{W}_2\text{S}_2\text{O}_2]^{2+}$  were hampered in aqueous solution due to serious stability problems: the  $[\text{W}_2\text{O}_2\text{S}_2]^{2+}$  dithiocation slowly decomposes in acidic aqueous medium with  $\text{H}_2\text{S}$  evolution into insoluble unidentified products.



The final step is the condensation step at pH = 5 in the presence of templating molecule 2,5-Dihydroxy-1,4-benzenediacetic acid shown in equation 4.9. In this step, the use of water as solvent is the key since it permits control of the condensation process by simple pH measurements. As  $[\text{W}_2\text{S}_2\text{O}_2]^{2+}$  does not stable in  $\text{H}_2\text{O}$ , mixed aqueous–DMF medium is used in order to monitor the polycondensation process of the primary dication.



Compared with the polycondensation of  $[\text{Mo}_2\text{S}_2\text{O}_2]^{2+}$  which is facilitated by the stability of building block in aqueous solution, the polycondensation of  $[\text{W}_2\text{S}_2\text{O}_2]^{2+}$  is more difficult, which is why only few such complexes have been reported.



The final products are crystallized in pure water with cesium as counterions. The crystallization can be prevented by the formation of large amount of insoluble unknown species during condensation. Only one bench product has relatively good solubility that forms fine single crystals. The crystals are stable in aqueous medium within a certain pH range. The stability may come from the charge changing from cationic to neutral or anionic.

#### 4.3.2 Structure

$\text{Cs}_4 [\text{W}_{16}\text{S}_{16}\text{O}_{16}(\text{OH})_{16}(\text{H}_2\text{O})_4(\text{C}_{10}\text{H}_8\text{O}_6)_2] \cdot 14\text{H}_2\text{O}$  was formed by the condensation of eight  $[\text{W}_2\text{S}_2\text{O}_2]^{2+}$  building blocks with two hydroquinone molecules symmetrically arranged inside the open cavity. Interestingly, the structure of  $[\text{W}_{16}(\text{C}_{10}\text{H}_8\text{O}_6)_2]^{4-}$  shown in Figure 4.2 resembles that of  $[\text{W}_{16}(\text{glu})_2]^{4-}$ , probably due to the similar molecular size of the template. In the case of  $[\text{W}_{16}(\text{glu})_2]^{4-}$ , two types of crystals were isolated, one orthorhombic and the other monoclinic. In our case, only crystals with monoclinic symmetry were obtained. The distances of W—W and W—S within the building blocks are 2.797(6) - 2.818 (6) Å and 2.315 (3) - 2.350 (3) Å respectively; the inter block hydroxo bridging bond W—O<sub>br</sub> is around 2.037 (8) - 2.095 (7) Å; and the bond length of W—O<sub>t</sub> residing at the outside of the backbone is 1.693 (9) - 1.725 (8) Å. These values are in a similar range to that of  $\text{W}_{16}\text{glu}_2$  (1b). However the structures inside the backbone are quite different. The bond lengths of carbonyl oxygen to tungsten are 2.272 (8) - 2.395

(8) Å in contrast with those of monoclinic  $[\text{W}_{16}\text{glu}_2]^{4-}$  from 2.255(9) Å to 2.337 (9) Å and the bond lengths of W with inner water  $\text{W}—\text{OH}_2$  are 2.297(9) — 2.309(8) Å in comparison with those of  $\text{W}_{16}\text{glu}_2$  at 2.363(10) — 2.403(9) Å. These differences suggest that 2,5-dihydroxy-1,4-benzenediacetic acid interacts more weakly with the backbone than glutaric acid does, while water molecules can form relatively stronger bonds with tungsten atoms in the hydroquinone complex. In addition, for hydroquinone templated complex, one carboxylate group bonds to tungsten within the building block bridged by sulfur while another carboxylate group bonds to tungsten of inter blocks bridged by hydroxo groups; for glutaric acid templated complex, each carboxylate group bonds to tungsten residing on the same building block. This structure difference suggests the interaction of each carboxylate group with tungsten in a hydroquinone templated complex may be different. Although XRD can not determine hydrogen, the bond lengths of  $\text{C}_7—\text{O}_{2\text{L}}$  and  $\text{C}_4—\text{O}_{1\text{L}}$  are within the carbon oxygen single bond range which are 1.414(16) Å and 1.391(18) Å respectively, indicating the intact dihydroxy groups maintained after the acido-basic reaction.

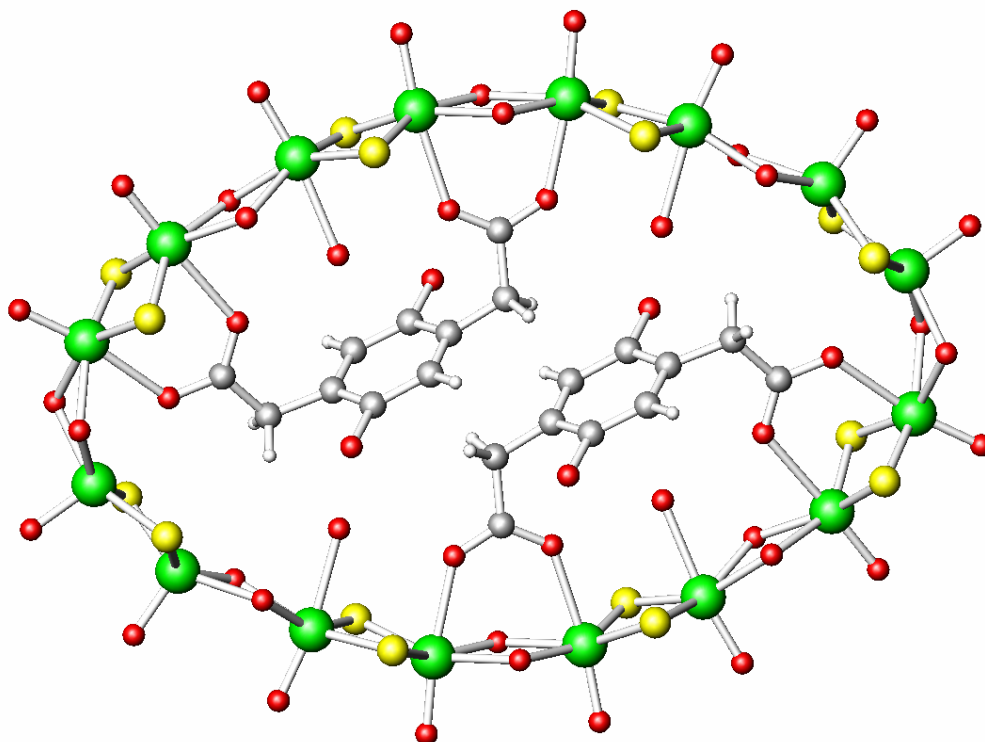


**Figure 4.2** Ball and Stick representations of  $\text{Cs}_4[\text{W}_{16}\text{S}_{16}\text{O}_{16}(\text{OH})_{16}(\text{H}_2\text{O})_4(\text{C}_{10}\text{H}_8\text{O}_6)_2] \cdot 14\text{H}_2\text{O}$  Green, tungsten; Red, oxygen; Yellow, sulfur; Grey, carbon; white, hydrogen.

### 4.3.3 Raman Spectra

Raman spectrum collected on a single crystal of  $\text{Cs}_4[\text{W}_{16}\text{S}_{16}\text{O}_{16}(\text{OH})_{16}(\text{H}_2\text{O})_4(\text{C}_{10}\text{H}_8\text{O}_6)_2] \cdot 14\text{H}_2\text{O}$  is shown in Figure 4.3b. Compared with that of 2,5-dihydroxy-1,4-benzenediacetic acid (Figure 4.3a), two peaks stand out. The peak at  $960.22 \text{ cm}^{-1}$  is assigned to  $\text{W}=\text{O}_t$  stretching and the peak at  $419.75 \text{ cm}^{-1}$  is assigned to  $\text{W}-\text{O}_{br}$  breathing. In addition, peaks from  $1300 \sim 1600 \text{ cm}^{-1}$  are assigned to

carbonyl group of 2,5-dihydroxy-1,4-benzenediacetic acid stretching. In contrast with normal Raman spectra in bulk, SERS spectrum of  $\text{Cs}_4 [\text{W}_{16}\text{S}_{16}\text{O}_{16}(\text{OH})_{16}(\text{H}_2\text{O})_4(\text{C}_{10}\text{H}_8\text{O}_6)_2] \cdot 14\text{H}_2\text{O}$  in aqueous solution (Figure 4.3c) with the addition of silver colloid also shows two strong peaks at  $957.31 \text{ cm}^{-1}$  and  $417.61 \text{ cm}^{-1}$  indicating the intact structure is maintained as shown in crystallography, except that the intensity of peak at  $957.31 \text{ cm}^{-1}$  becomes weaker and the intensity of peak at  $417.61 \text{ cm}^{-1}$  becomes stronger which is due to the random molecular orientation in solution.

#### 4.3.4 NMR Spectra

The  $^1\text{H}$  NMR spectrum of  $\text{Cs}_4 [\text{W}_{16}\text{S}_{16}\text{O}_{16}(\text{OH})_{16}(\text{H}_2\text{O})_4(\text{C}_{10}\text{H}_8\text{O}_6)_2] \cdot 14\text{H}_2\text{O}$  in  $\text{D}_2\text{O}$  (around 1mM) is shown in Figure 4.4. Peaks at 8.70 ppm and 3.47 ppm are assigned to free 2,5-dihydroxy-1,4-benzenediacetic acid. Peaks at 5.30 ppm and 0.51~1.58 ppm were assigned to coordinated 2,5-dihydroxy-1,4-benzenediacetic acid based on the integration. Ethanol peaks are also shown in the spectrum as impurities. From the spectrum, an up-field shift is observed for the coordinated 2,5-dihydroxy-1,4-benzenediacetic acid compared to the free one indicating the interactions between the polyoxometalate and the hydroquinone. Also the multiple split peaks in the range of 0.51~1.58 ppm suggest an asymmetric environment that the  $-\text{CH}_2-$  groups have experienced. Detailed assignment of the peaks in this region is not yet complete. The  $^1\text{H}$  NMR at different temperatures may clean up the spectra as shown from a previous study which will help to explain or assign these multiple peaks. The coexistence of two sets of 2,5-dihydroxy-1,4-benzenediacetic acid peaks may suggest an equilibrium between hydroquinone and its complex; the use of  $^1\text{H}$  NMR at various temperatures should further confirm this observation.

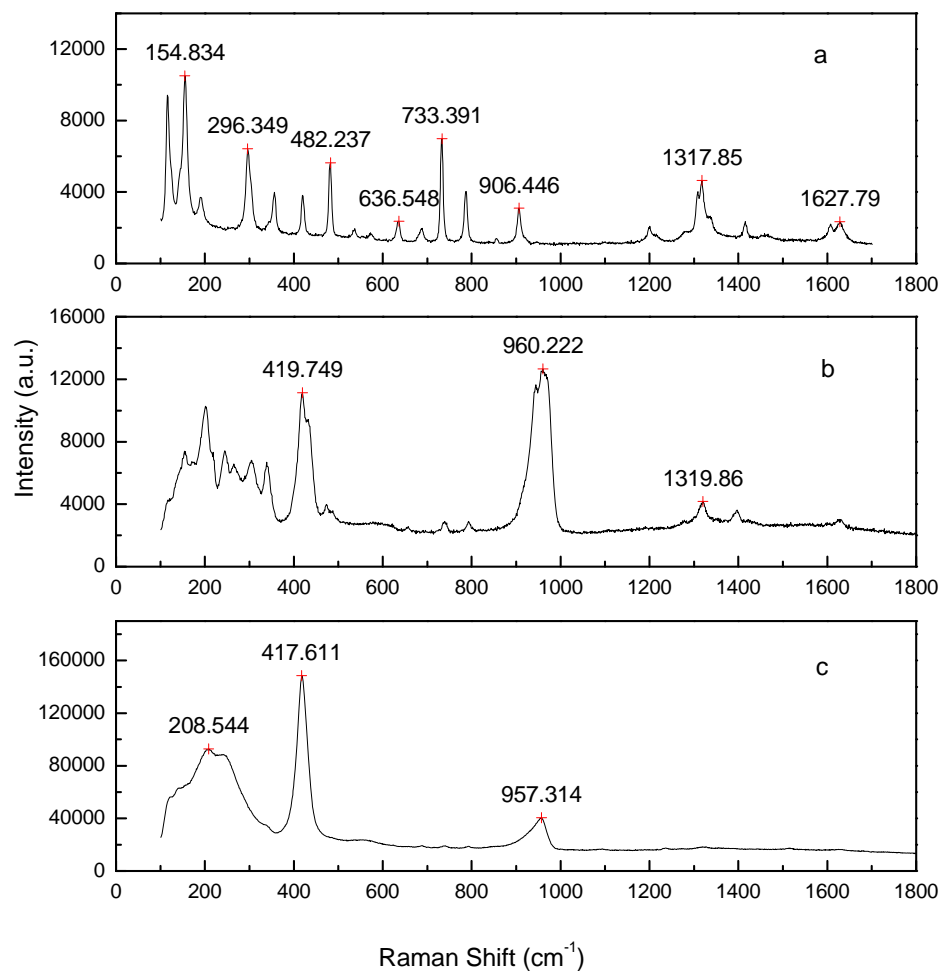


**Figure 4.3** Raman spectrum of (a) 2,5-dihydroxy-1,4-benzenediacetic acid crystal (b) Cs<sub>4</sub> [W<sub>16</sub>S<sub>16</sub>O<sub>16</sub>(OH)<sub>16</sub>(H<sub>2</sub>O)<sub>4</sub>(C<sub>10</sub>H<sub>8</sub>O<sub>6</sub>)<sub>2</sub>]·14H<sub>2</sub>O crystal and SERS of (c) Cs<sub>4</sub> [W<sub>16</sub>S<sub>16</sub>O<sub>16</sub>(OH)<sub>16</sub>(H<sub>2</sub>O)<sub>4</sub>(C<sub>10</sub>H<sub>8</sub>O<sub>6</sub>)<sub>2</sub>]·14H<sub>2</sub>O aqueous solution with silver nanoparticles

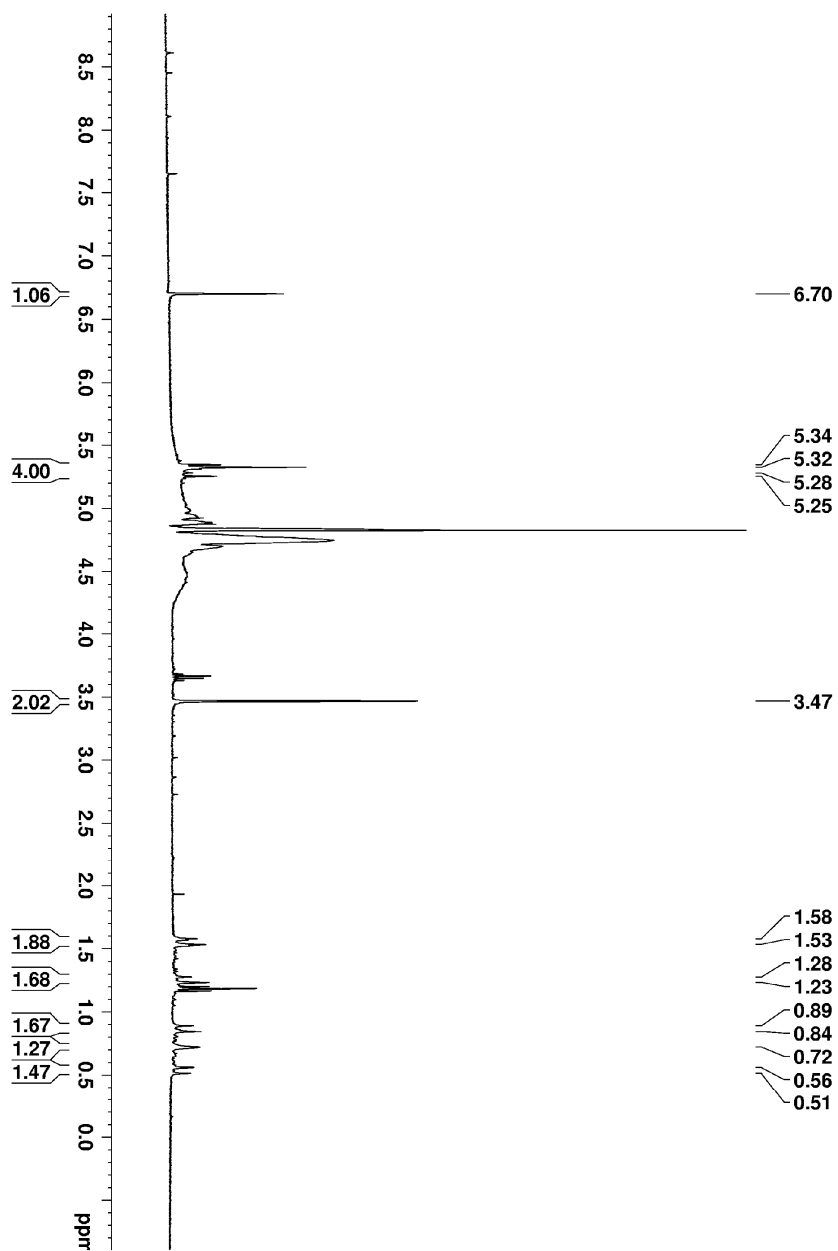


**Figure 4.4**  $^1\text{H}$  NMR spectrum of  $\text{Cs}_4[\text{W}_{16}\text{S}_{16}\text{O}_{16}(\text{OH})_{16}(\text{H}_2\text{O})_4(\text{C}_{10}\text{H}_8\text{O}_6)_2] \cdot 14\text{H}_2\text{O}$  in  $\text{D}_2\text{O}$

### 4.3.5 Electrochemistry Study

#### 4.3.5.1 Electrochemistry of 2,5-dihydroxy-1,4-benzenediacetic acid

The electrochemistry of 2,5-dihydroxy-1,4-benzenediacetic acid follows the typical behavior of the quinone compound. Due to the diacetic acid substitute, its half potential will be different from that of 1,4-benzoquinone. A previous study by Peover<sup>26</sup> indicated the following results as for the substituent effect on the potential of 1,4-benzoquinone: (1) Electron-releasing substituent (methyl, t-butyl) increases the energy of the lowest unoccupied orbital and results in more negative half potentials with an increasing number of substituents. (2) Electronegative substituents (halogen, cyanide) can decrease this energy, leading to more positive half potentials, and the potentials are also affected by the number of substituents. (3) Both type substituents exist, inductive far prevail over conjugative effects. Based on these, the diacetic substitutions will make the half potential more negative than that of 1,4-benzoquinone. This is further confirmed by the published  $E^{\circ}$  of both species. The published  $E^{\circ}$  of 2,5-dihydroxy-1,4-benzenediacetic acid is 0.306V vs. SCE in 0.1 sulfuric acid<sup>52</sup> and the  $E^{\circ}$  of 1,4-benzoquinone is 0.433V vs. SCE in PH=0 aqueous solution<sup>26,53</sup>. Considering 60mV shift per PH, these values are consistent with Peover's observation. The cyclic voltammetry of 2,5-dihydroxy-1,4-benzenediacetic acid in PH 5 acetic buffer solution is shown in Figure 4.5. The  $E_{1/2}$  is around 0.149 V vs. Ag | AgCl | KCl (sat). This value is also comparable with the published value.

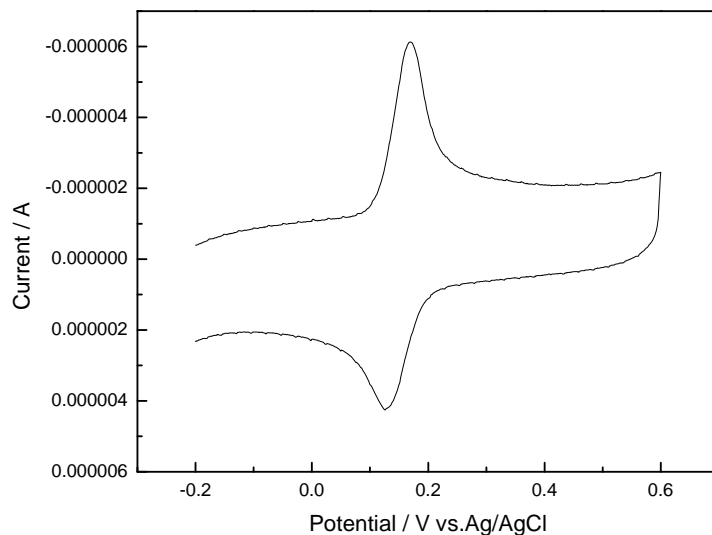


**Figure 4.5** Cyclic Voltammetry of 2,5-dihydroxy-1,4-benzenediacetic acid in pH 5 acetic buffer solution

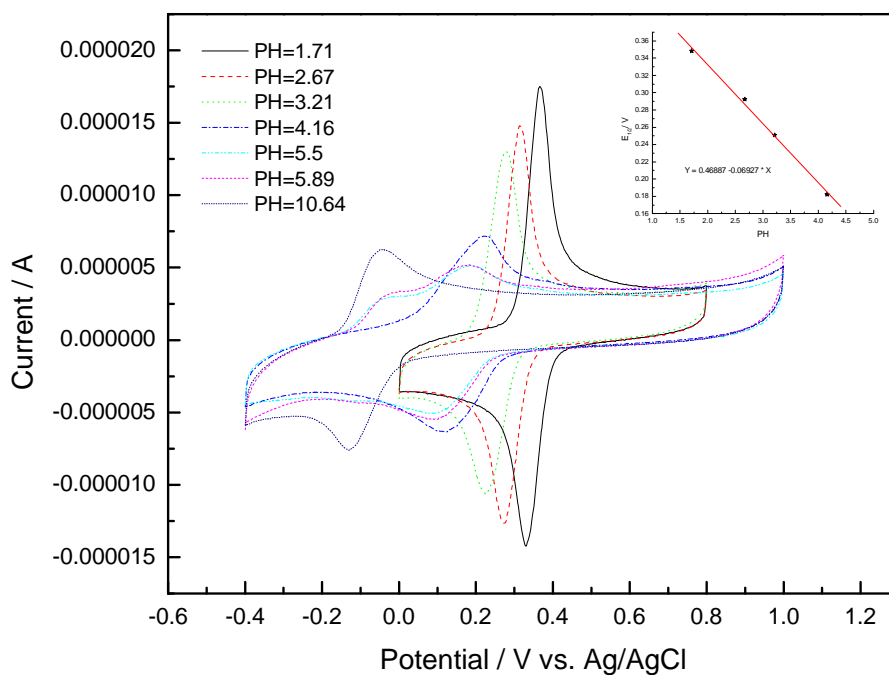


**Figure 4.6** Cyclic Voltammetry of 2,5-dihydroxy-1,4-benzenediacetic acid in  $\text{NaClO}_4$  at different pH, pH was adjusted by titrating  $\text{HClO}_4$  or  $\text{NaOH}$  to the solution. Scan rate is 100 mV/s.



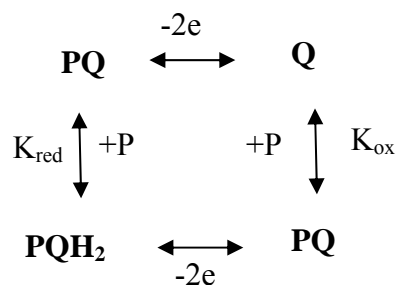
A cyclic voltammetry measurement was also conducted in unbuffered solution at a different pH. The results are shown in Figure 4.6. When base is added, the half potential continuously shifts to the negative potential with increasing pH. When acid is added, the half potential continuously shifts to the positive potential with decreasing pH. At a pH around 5.5~6, another oxidation peak at more positive potential appears. A scan rate dependent study at this pH shows that at a low scan rate there are two reduction peaks corresponding to the two oxidation peaks respectively; however at a high scan rate (100 mV/s) only one reduction peak corresponding to the oxidation peak at more positive potential appears. This may be due to the local pH effect and kinetic effect on glassy carbon electrode.

#### **4.3.5.2 Electrochemistry of POM-Hydroquinone Complex**

Taking the possibilities of acetic acid exchanges with the encapsulated hydroquinone into consideration, the electrochemistry was conducted in 0.1 M NaClO<sub>4</sub> (pH is around 5) unbuffered solution instead of the acetic buffer solution. The cyclic voltammetry of the POM- hydroquinone complex is shown in Figure 4.7. The initial scan started from 0 mV and extended to 400 mV; one redox peak showed up. With continuous scan of the more positive potentials (600mV, 800mV, 1000mV), another peak appeared. In order to give precise assignments to these peaks, NMR was run to analyze the components in the solution before and after electrical oxidation; the result was that when the scan happened between 0 and 400 mV, an intact structure of POM complex was maintained while further scans in a more positive direction resulting in the decomposition of the POM. In addition, that the NMR spectra was showing two sets of peaks (free and bonded hydroquinone) indicates that initially the redox peaks between 0 and 400 mV

were attributed to both species. The irreversible peak around 800 mV was assigned to the oxidation of sulfur and consequently led to the decomposition of the POM complex. Another interesting observation is that with each additional scan in the more positive direction, that is, when more free hydroquinone was released to the system, the oxidation potential of the assigned free and bonded hydroquinone peak kept shifting to the right and the peaks become more reversible as well. Since the total concentration of hydroquinone including both the free and bonded ones is a constant, the redox potential shift can not be due to the local effective pH in which the half wave potential was determined by the concentration of hydroquinone in unbuffered solution, except that the decomposition of POM complex can decrease the pH of the solution. The former was proved by a control experiment in which cyclic voltammetry was run on a fixed amount of hydroquinone, and the results are shown in Figure 4.8. Compared to what is shown in Figure 4.7, the redox potential of hydroquinone was not affected by scanning to a more positive potential. However, it is difficult to prove the latter possibility. Another better explanation to the potential shift is the redox dependent receptor-substrate binding scheme shown in Scheme 4.3., where  $\text{QH}_2$  is 2,5-dihydroxy-1,4-benzenediacetic acid and Q is its oxidized form; P is semi sphere POM backbone, since each hydroquinone molecule was symmetrically bonded to half of the POM backbone;  $\text{P}(\text{QH}_2)$  is the reduced form of POM-hydroquinone complex and  $\text{PQ}$  is its corresponding oxidized form; and  $K_{\text{red}}$  and  $K_{\text{ox}}$  are the bonding constants of reduced form and oxidized form respectively. Basically two equilibriums coexist in the solution, one is the equilibrium between the reduced species and the other is the equilibrium among the oxidized species. Due to the difference between the binding constants  $K_{\text{red}}$  and  $K_{\text{ox}}$ , a  $\Delta E$  was observed. In this case, the

stronger bonding of POM substrate to the oxidized hydroquinone is probably due to the well-delocalized electrons of the oxidized form resulting in the reduction of hydroquinone becoming more difficult. Thus a negative shift of the redox potential of hydroquinone was observed. Consistent with the established titration method in which a certain amount of substrate was continuously added into the acceptor solution and  $\Delta E$  was measured accordingly, the concentration of substrate P in our case kept decreasing with successive scan and the potential measured was shifting towards the standard potential of free 2,5-dihydroxy-1,4-benzenediacetic acid.



**Scheme 4.3** P-Q binding equilibrium scheme

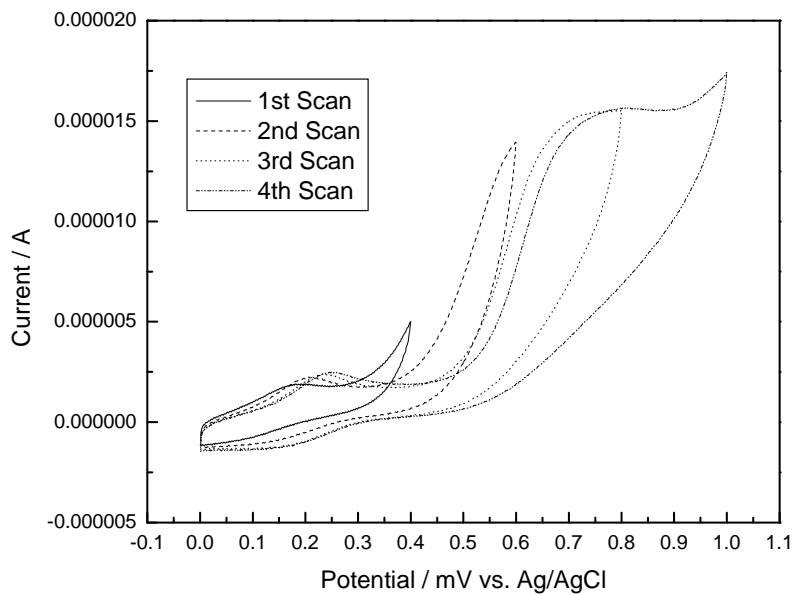


**Figure 4.7** Cyclic voltammetry of  $\text{Cs}_4 [\text{W}_{16}\text{S}_{16}\text{O}_{16}(\text{OH})_{16}(\text{H}_2\text{O})_4(\text{C}_{10}\text{H}_8\text{O}_6)_2] \cdot 14\text{H}_2\text{O}$  in  $0.1\text{M NaClO}_4$

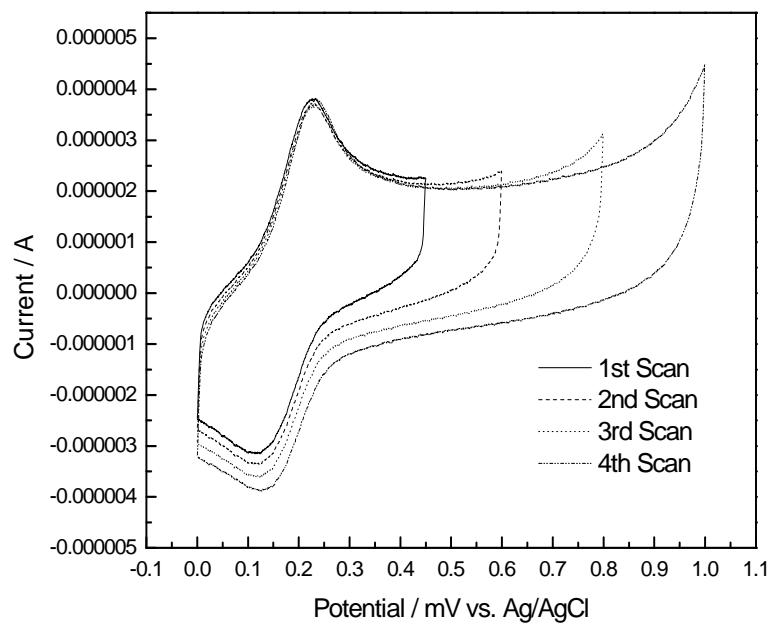


**Figure 4.8** Cyclic voltammetry of 2,5-dihydroxy-1,4-benzenediacetic acid in  $0.1\text{M NaClO}_4$

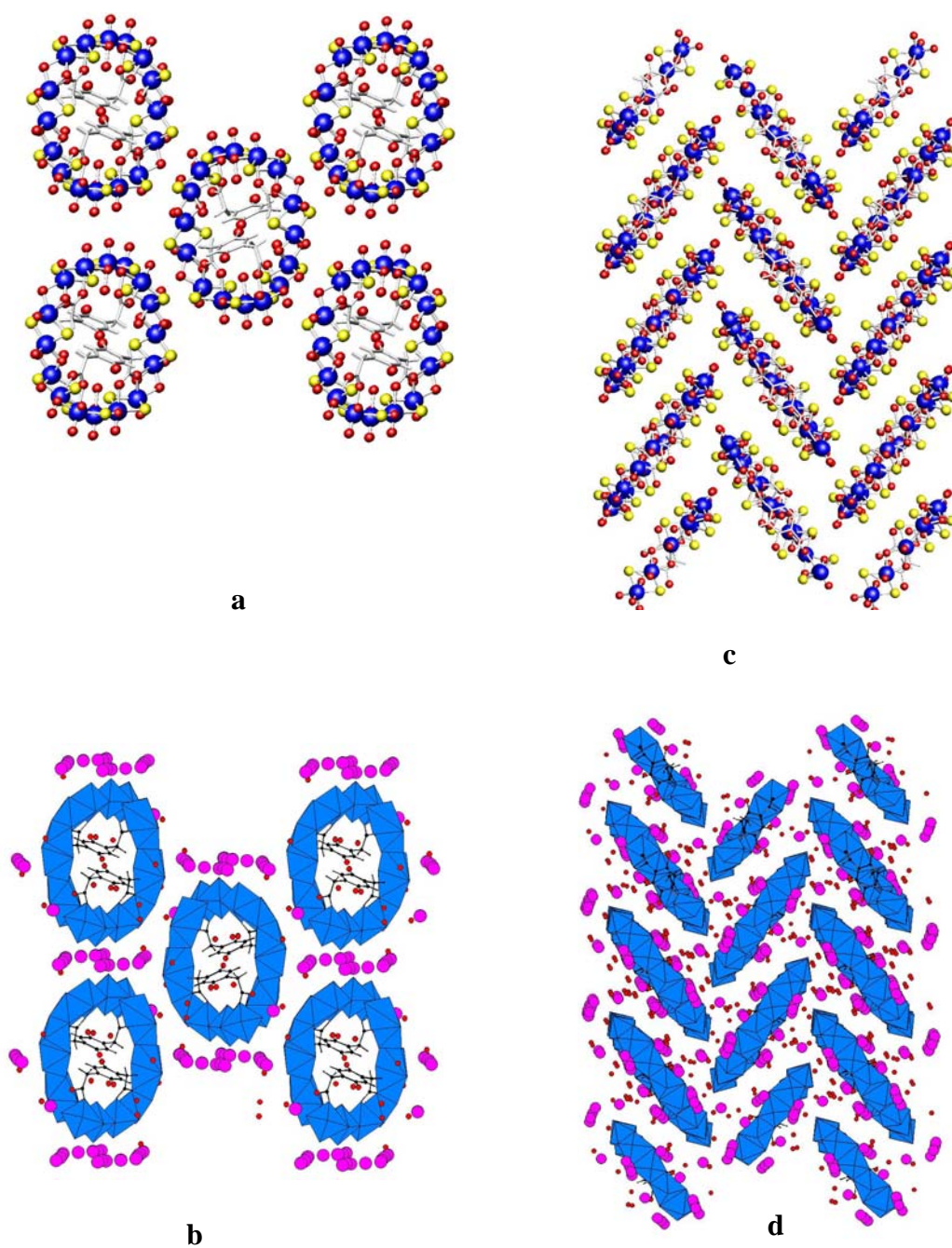


**Figure 4.9** Extended structure of  $\text{Cs}_4[\text{W}_{16}\text{S}_{16}\text{O}_{16}(\text{OH})_{16}(\text{H}_2\text{O})_4(\text{C}_{10}\text{H}_8\text{O}_6)_2] \cdot 14\text{H}_2\text{O}$ , (a) view along with a-axis (b) view along a-axis with cesium counter ions (c) zigzag diagram along an alternative axis (d) zigzag diagram with cesium counter ions

### 4.3.6 Extended Structure

The extended 3D structure of POM-hydroquinone complex was shown in Figure 4.9. The cyclic molecule was linked by the counter ions or the water through hydrogen bonding. The counter ions  $\text{Li}^+$ ,  $\text{Na}^+$ ,  $\text{K}^+$  sometimes can help forming orderly packing such as sodium pillards in  $\text{Na}_4[(\text{HPO}_4)_2\text{Mo}_{12}\text{S}_{12}\text{O}_{12}(\text{OH})_{12}](\text{H}_2\text{O})_2 \cdot 27\text{H}_2\text{O}$  and potassium planes in  $\text{K}_3[\text{ClMo}_{10}\text{S}_{10}\text{O}_{10}(\text{OH})_{12}(\text{H}_2\text{O})_3] \cdot 14\text{H}_2\text{O}$ <sup>54</sup>. But for cesium, it is difficult to form such orderly packing probably due to its large radius.

### 4.4 Future Work

Our preliminary work on the  $\text{Cs}_4 [\text{W}_{16}\text{S}_{16}\text{O}_{16}(\text{OH})_{16}(\text{H}_2\text{O})_4(\text{C}_{10}\text{H}_8\text{O}_6)_2] \cdot 14\text{H}_2\text{O}$  complex including its synthesis, characterization, and electrochemistry revealed an interesting new research area. However, our knowledge of the compound is still very limited and mainly due to the restricted amount of crystals we can work with. In addition, we faced some purifying issues, in which the 2,5-dihydroxy-1,4-benzenediacetic acid seemed a little sticky on the crystal surface and was difficult to get rid of. Therefore some work needs to be done involving the improvement of synthetic conditions and purification. Also  $^1\text{H}$  NMR at variant temperatures will be a great help toward understanding the thermodynamic of the complex in solution. As for the electrochemistry study, cyclic voltammetry in aprotic solvent may provide some hint to better understanding the electrochemical behavior. Since the cesium complex doesn't dissolve in any aprotic solvents, an ion exchange with  $\text{Li}^+$  is required. The last thoughts, cesium is substituted with  $\text{Li}^+$ ,  $\text{Na}^+$  or  $\text{K}^+$  using ion exchange method to develop 3D counter ion framework which can serve as ion transport carrier or highly conductive materials.

## 4.5 Conclusions

A POM-encapsulated hydroquinone system was prepared by coordinating 2,5-dihydroxy-1,4-benzenediacetic acid to the cyclic neutral oxothiocompound  $W_{16}S_{16}O_{16}(OH)_{16}$ . The complex was formed by acido-basic condensation of eight  $[W_2S_2O_2]^{2+}$  building blocks while 2,5-dihydroxy-1,4-benzenediacetic acid acted as a template. Crystals were grown through slow evaporation and single crystal XRD shows two 2,5-dihydroxy-1,4-benzenediacetic acid molecules were encapsulated into the cavity of  $W_{16}S_{16}O_{16}(OH)_{16}$ . Due to the steric constraints induced by the presence of 2,5-dihydroxy-1,4-benzenediacetic acid in the cavity, four tungsten atoms show pyramidal geometry. The NMR spectrum of the complex in  $D_2O$  shows both free and coordinated 2,5-dihydroxy-1,4-benzenediacetic acid suggesting an equilibrium between the two species. The cyclic voltammetry of the complex shows one redox couple which was assigned to both free and coordinated hydroquinone in the range of 0-400 mV. Further scans to more positive potential would cause the decomposition of the complex. The potential shift shown in the decomposition process can be explained by the redox dependent theory. This will be the first example in such a system in which redox dependent behavior was observed.

## 4.6 Reference

1. Secheresse, F.; Dolbecq, A.; Mialane, P.; Cadot, E., *C. R. Chim.* **2005**, 8, (11-12), 1927-1938.
2. Müller, A.; Beckmann, E.; Bogge, H.; Schmidtman, M.; Dress, A., *Angew. Chem., Int. Ed.* **2002**, 41, (7), 1162-1167.
3. Mitchell, P. C. H., *Nature* **1990**, 348, (6296), 15-16.

4. Müller, A., *Nature* **1991**, 352, (6331), 115-115.
5. Day, V. W.; Klemperer, W. G.; Yaghi, O. M., *Nature* **1991**, 352, (6331), 115-116.
6. Pope, M. T., *Nature* **1992**, 355, (6355), 27-27.
7. Müller, A.; Reuter, H.; Dillinger, S., *Angew. Chem., Int. Ed.* **1995**, 34, (21), 2328-2361.
8. Cadot, E.; Salignac, B.; Halut, S.; Secheresse, F., *Angew. Chem., Int. Ed.* **1998**, 37, (5), 611-612.
9. Floquet, S.; Marrot, J.; Cadot, E., *C. R. Chim.* **2005**, 8, (6-7), 1067-1075.
10. Salignac, B.; Riedel, S.; Dolbecq, A.; Secheresse, F.; Cadot, E., *J. Am. Chem. Soc.* **2000**, 122, (42), 10381-10389.
11. Du Peloux, C.; Dolbecq, A.; Cadot, E.; Marrot, J.; Secheresse, F., *J. Mol. Struct.* **2003**, 656, (1-3), 37-44.
12. Dolbecq, A.; Cadot, E.; Secheresse, F., *Comptes Rendus de l'Academie des Sciences, Serie IIC: Chimie* **2000**, 3, (3), 193-197.
13. Cadot, E.; Pouet, M.-J.; Robert-Labarre, C.; Du Peloux, C.; Marrot, J.; Secheresse, F., *J. Am. Chem. Soc.* **2004**, 126, (29), 9127-9134.
14. Cadot, E.; Salignac, B.; Loiseau, T.; Dolbecq, A.; Secheresse, F., *Chem.--Eur. J.* **1999**, 5, (11), 3390-3398.
15. Cadot, E.; Dolbecq, A.; Salignac, B.; Secheresse, F., *Chem.--Eur. J.* **1999**, 5, (8), 2396-2403.
16. Cadot, E.; Salignac, B.; Marrot, J.; Dolbecq, A.; Secheresse, F., *Chem. Commun. (Cambridge)* **2000**, (4), 261-262.



17. Cadot, E.; Marrot, J.; Secheresse, F., *Angew. Chem., Int. Ed.* **2001**, 40, (4), 774-777.
18. Cadot, E.; Marrot, J.; Secheresse, F., *J. Cluster Sci.* **2002**, 13, (3), 303-312.
19. Vetter, K. J., *Electrochemical Kinetics*. Academic Press: New York, 1967.
20. Chambers, J. Q., *The Chemistry of the Quinonoid Compounds*. Wiley: New York, 1974; Vol. I, Chapter 14, p 737-791.
21. Kolthoff, I. M.; Lingane, J. J., *Polarography*. Interscience: New York, 1952; Vol. I, Chapter XIV and XV.
22. Kolthoff, I. M.; Lingane, J. J., *Polarography*. 2nd ed.; Interscience: New York, 1952; Vol. II, Chapter XL.
23. Chambers, J. Q., *The Chemistry of the Quinonoid Compounds*. Wiley: New York, 1988; Vol. II, Chapter 12, p 719-757.
24. Bailey, S. I.; Ritchie, I. M., *Electrochim. Acta* **1985**, 30, 3-12.
25. Peover, M. E., *In Electroanalytical Chemistry*. Dekker: New York, 1967; p 1-51.
26. Peover, M. E., *J. Chem. Soc.* **1962**, 4540-4549.
27. Wilford, J. H.; Archer, M. D., *J. Electroanal. Chem.* **1985**, 190, 271-277.
28. Jaworski, J. S.; Lesniewska, E.; Kolinowski, M. K., *J. Electroanal. Chem.* **1979**, 105, 329.
29. Russel, C.; Jaenicke, J., *J. Electroanal. Chem.* **1986**, 199, 139-151.
30. Peover, M. E.; Davis, J. D., *J. Electroanal. Chem.* **1963**, 6, 46-53.
31. Nagaoka, T.; Okazaki, S.; Fujinaga, T., *J. Electroanal. Chem.* **1982**, 133, 89.
32. Eggins, B. R., *Chem. Commun. (Cambridge)* **1969**, 1267-1268.
33. Gupta, N.; Linschitz, H., *J. Am. Chem. Soc.* **1997**, 119, 6384-6391.

34. Eiggins, B. R.; Robertson, P. K. J., *J. Chem. Soc., Faraday Trans.* **1994**, 90, 2249.
35. Robertson, R. T.; Pendley, B. D., *J. Electroanal. Chem.* **1994**, 374, 173.
36. Abbott, J. C.; Collat, J. W., *Anal. Chem.* **1963**, 35, 859.
37. Tang, Y.; Wu, Y.; Wang, Z., *J. Electrochem. Soc.* **2001**, 148, (4), E133-E-138.
38. Ge, Y.; Smith, D. K., *Anal. Chem.* **2000**, 72, (8), 1860-1865.
39. Lilienthal, N. D.; Alsafar, H.; Conerty, J.; Fernandez, R.; Kong, C.; Smith Diane, K., *Anal. Chem.* **2003**, 75, (14), 3322-8.
40. Connors, K. A., *Binding Constants*. John Wiley: New York, 1987; p 348-351.
41. Beer, P. D., *Adv. Inorg. Chem.* **1992**, 39, 79.
42. Beer, P. D., *Acc. Chem. Res.* **1998**, 31, 71-80.
43. Tucker, J. H. R., Collinson, S. R., *Chem. Soc. Rev.* **2002**, 31, 147-156.
44. Wood, J. H.; Cox, L., *Org. Synth.* **1946**, 26, 24.
45. Wood, J. H.; Colburn, C. S.; Cox, L.; Garland, H. C., *J. Am. Chem. Soc.* **1944**, 66, (9), 1540-1542.
46. Wood, J. H.; Cox, L., *Organic syntheses. Coll. Vol.* **1955**, 3, 286.
47. Bereau, V.; Cadot, E.; Boegge, H.; Mueller, A.; Secheresse, F., *Inorg. Chem.* **1999**, 38, (25), 5803-5808.
48. Sheldrick, G. M., *Acta Crystallogr. A* **1995**, 51, 33.
49. Sheldrick, G. M. *SHELXTL PC, An Integrated System for SolVing, Refining, and Displaying Crystal Structures from Diffraction Data*, 6.12; Siemens Analytical X-Ray Instruments, Inc.: Madison, WI, 2001.
50. Miller, K. F.; Bruce, A. E.; Corbin, J. L.; Wherland, S.; Stiefel, E. I., *J. Am. Chem. Soc.* **1980**, 102, (15), 5102-5104.

51. Coucouvanis, D.; Toupadakis, A.; Hadjikyriacou, A., *Inorg. Chem.* **1988**, 27, (19), 3272-3273.
52. No, D. M.; Corkery, K. K.; Gonzalez, E.; Marantos, K. A.; Estrada, K. E., *J. Chem. Eng. Data* **1994**, 39, 813-816.
53. Clark, W. M., *Oxidation-reduction potentials of organic systems*. 2 Editions ed.; Baltimore, Williams & Wilkins: 1960.
54. Cadot, E.; Secheresse, F., *Chem. Commun. (Cambridge, U. K.)* **2002**, (19), 2189-2197.

**CHAPTER FIVE**  
**LBL ASSEMBLY OF GOLD NANOPARTICLES AND**  
**POLYOXOMETALATE FOR OXYGEN REDUCTION**

**5.1 Introduction**

Driven by the current global energy crisis, the development of alternative energy sources has become crucial for economies worldwide. One of the most promising of these alternatives, fuel cells show great promise as a useful power source and have attracted a great deal of attention due to their compactness, light weight, and reliability. Among the various fuel cell systems being considered, hydrogen fuel cells, or PEMs (Proton Exchange Membranes), are an important option. Figure 5.1 shows a diagram of the operating principles of hydrogen fuel cells.

The hydrogen fuel cell operates in a similar way to a battery, with two electrodes, an anode and a cathode, separated by a membrane. Hydrogen and oxygen pass over the anode and cathode, respectively. The hydrogen reacts to a catalyst on the anode and is converted into negatively charged electrons ( $e^-$ ) and positively charged ions ( $H^+$ ). The electrons generated during the oxidation process then flow out of the cell as electrical energy. The hydrogen ions migrate through the electrolyte membrane to the cathode, where they combine with oxygen and electrons to produce water. The most commonly

used membrane is DuPont's Nafion™, which transports protons based on liquid water humidification of the membrane.

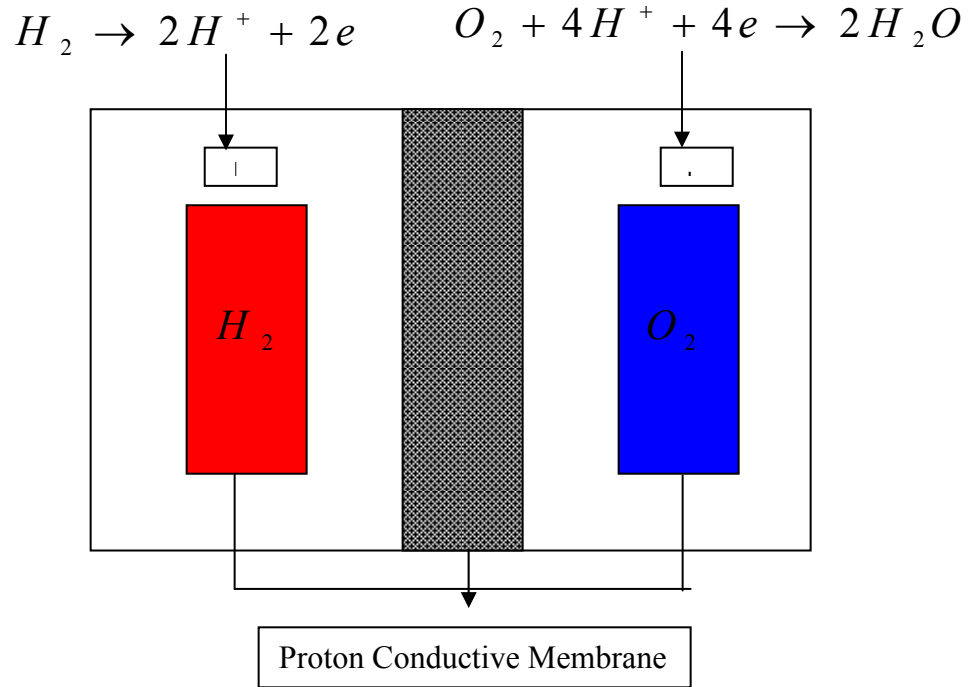


**Figure 5.1** Principles of hydrogen fuel cell operation

At present, PEM fuel cells can generate power in the range of 100W to 500kW. For Nafion™ membranes, the working temperature is from 50° C to 120° C The reported electrical efficiency for the cell alone is 50~70%, and 30~50% for the overall system. Some commercial PEM fuel cells are now commercially available, but many issues need to be resolved in order to compete effectively with other options. A major challenge is the high cost involved as a result of the use of Pt as the catalyst. Considerable effort has been devoted to research into alternative catalysts that are significantly less expensive but capable of maintaining the same catalytic performance. For oxygen reduction, for example, several research directions have been explored, the two most promising of

which are: (1) A reduction in the amount of platinum needed, with a Pt monolayer being supported by metal, metal alloy, non-noble metal-noble metal core-shell and oxide nanoparticles. In this strategy, not only is the Pt content greatly reduced, but the catalytic activity also improves. The fabrication of the Pt monolayer in the electrocatalytic system is achieved by either spontaneous Pt deposition or displacement of an adsorbed Cu monolayer<sup>1-8</sup>. A significant feature of this approach is that introducing another metal, such as Co or Ru, to the system leads to the formation of a bimetallic catalyst<sup>9</sup> that has been shown to improve the stability<sup>8</sup>, enhance the catalytic performance and reduce CO poisoning to the Pt<sup>10</sup>. (2) The development of cheaper electrocatalysts to replace Pt, such as Pd alloy<sup>1, 4, 11, 12</sup> polyoxometalate, or porphyrin<sup>13-18,19-23</sup>. The second of these two approaches, the development of a Pt free, noble metal free or even metal free catalyst, was chosen for the work reported in this chapter.

Our research group has conducted extensive research into the catalytic activity of polyoxometalates for oxygen reduction.<sup>24</sup> Polyoxometalates (POMs) are nanometer scale metal oxygen clusters that have been widely used as catalysts owing to their ability to mediate electron, proton and oxygen atom transfer reactions.<sup>25-28</sup>. Previous work has examined the influence of a series of transition-metal-substituted Wells-Dawson ( $P_2W_{17}M_nO_{62}^{(12-n)-}$ ;  $M = W^{VI}, Fe^{II}, Co^{II}, Ru^{II}$ ) and Keggin ( $PW_{12}O_{40}^{3-}$  and  $PCoW_{11}O_{39}^{5-}$ ) anions on the oxygen reduction reaction (ORR) at Au, Pd, and Pt electrodes. This focus originated from the belief that transition metal-substituted POMs adsorbed on the surface of an electrode that is catalytically active for the reduction of adsorbed O atoms (i.e., Au, Pd, Pt) should function in much the same way as a typical bimetallic ORR catalyst. It was found that Wells-Dawson POMs adsorbed on Au lead to large positive shifts of the ORR

potential, which suggested that substituting the bulk gold with gold nanoparticles might produce interesting results. Due to the high surface to volume ratio of nanoparticles, the amount of gold needed is greatly reduced and high catalytic specificity is also expected. There are several strategies reported in the literature for building a composite containing POMs and gold nanoparticles. For example, the POMs can be used as both reducing agents and stabilizing agents to synthesize gold nanoparticles<sup>29-31</sup>, although the disadvantage of this method is that the POMs may block the active catalytic sites on the nanoparticles. Another possibility is to adopt a layer-by-layer (LBL) method, alternately depositing POMs and gold nanoparticles on the substrate. The blocking effect should be reduced compared to the first strategy, and the nature of LBL enables the quantification of the catalytic activity. Although the concept of specific activity has been established for a Pt system in which catalysts are immobilized in Nafion™ film, the equivalent gold system has not yet been characterized. In this chapter, therefore, a study of the specific activity to oxygen reduction of an LBL assembly of Cobalt monosubstituted Wells Dawson and PDDA stabilized nanoparticles is reported. A comparison of this LBL system with other published results is included.

## **5.2 Experimental**

### ***5.2.1 Chemicals and reagents***

Poly (diallyldimethylammonium chloride), PDDA (35wt% in water), and HAuCl<sub>4</sub> (99.99% trace metals basis, 30 wt. % in dilute HCl) were purchased from Sigma-Aldrich. NaBH<sub>4</sub> (98% powder) were purchased from Acros Organics. Ru(NH<sub>3</sub>)<sub>6</sub>Cl<sub>3</sub> (Ru 32.69%), NaClO<sub>4</sub>·H<sub>2</sub>O (85%-90%) was purchased from Alfa Aesar. NaOH and HClO<sub>4</sub> (70%) were purchased from Fisher Scientific. All reagents were used as received without further

purification. Cobalt substituted Wells-Dawson (Co-Dawson) and Ruthenium substituted Wells-Dawson (Ru-Dawson) were synthesized according to the procedures given in the literature<sup>32, 33</sup>. The water used was purified through a Barnstead™ Nanopure system.

### **5.2.2 Apparatus**

*Electrochemistry Measurements:* All the measurements were performed in aqueous solution containing 0.1M HClO<sub>4</sub> (oxygen reduction) or 0.1 M NaClO<sub>4</sub> (electroactive probe measurement) as electrolyte. A standard three-electrode, one-compartment cell was employed. The working electrode was a 3 mm diameter glassy carbon electrode (BASi) modified with the LBL assembly or a 6 mm diameter glassy carbon rotating disk electrode (PINE instrument) modified with the LBL assembly. The reference and counter electrodes were Ag/AgCl and Platinum gauge, respectively. An Epsilon Potentiostat from BASi was employed. For the oxygen reduction experiment, the HClO<sub>4</sub> solution was bubbled with oxygen (ultra high purity, Airgas) for at least 10 minutes before each measurement.

*UV-vis Measurements:* UV-vis spectra were collected on a Shimadzu UV-3600 UV-vis-near infrared (UV-vis-NIR) spectrophotometer.

*TEM measurements:* Samples were imaged with a Zeiss EM10 transmission electron microscope (Carl Zeiss SMT, Inc, Germany) operated at an accelerating voltage of 60 kV. The sample for TEM characterization was prepared by placing a drop of colloidal solution on formvar-carbon coated copper 400 mesh grid and dried at room temperature.

### **5.2.3 Procedures**

*Preparation of gold nanoparticle:* In a typical experiment, 250 µl PDDA (4 wt% in water), 5 ml water, 150 µl 0.5 M NaOH and 15µl HAuCl<sub>4</sub> (10 mg/ml) were placed in a



beaker. After thoroughly mixing for 2 min, 100  $\mu\text{l}$   $\text{NaBH}_4$  (4.8M) was added to the mixture. The peak of the UV–vis spectrum was found to be located at about 516 nm. The nanoparticles obtained were estimated to be about 10 nm in diameter by TEM.

*Preparation of LBL assembly on glassy carbon electrode:* The glassy carbon electrode was polished with 0.05  $\mu\text{m}$   $\text{Al}_2\text{O}_3$  slurry followed by washing and sonicating in deionized water. The electrode was then rinsed with methanol and wiped dry. The cleaned electrode was activated at 1.25 V (Ag/AgCl) for 5 min in 1.0 M sodium hydroxide, then thoroughly washed with deionized water and dried with  $\text{N}_2$ . The prepared electrode was dipped into a solution containing PDDA stabilized gold nanoparticles (PDDA- $\text{Au}_{\text{NP}}$ ) for an hour, washed with deionized water, and dried with a gentle stream of nitrogen. A negatively charged polyoxometalate layer was subsequently deposited onto the positively charged substrate using the same washing and drying procedure as described above. This process was repeated as necessary, with 20 min immersion time for the deposition of each layer. The outermost layer of the GC multilayer film fabricated was a Co-Dawson POM for oxygen reduction measurements and PDDA- $\text{Au}_{\text{NP}}$  for electroactive probe measurements (Figure 5.2).

*Preparation of LBL assembly on glass slides:* A glass microscope slide (2cm by 0.5cm) was sonicated in M90 for one hour, and then rinsed with deionized water. The glass slide was then sonicated in 60% ethanol + 39% water + 1% NaOH at 50°C for 30 minutes, followed by rinsing with deionized water and drying under  $\text{N}_2$ . The prepared glass slide was then dipped into PDDA- $\text{Au}_{\text{NP}}$  solution and POM solution alternately, with washing and drying in between, to form a (PDDA- $\text{Au}_{\text{NP}}$ /Co-Dawson) $_n$  assembly. The outmost layer of the multilayer film fabricated on the glass slide was a PDDA- $\text{Au}_{\text{NP}}$  layer.

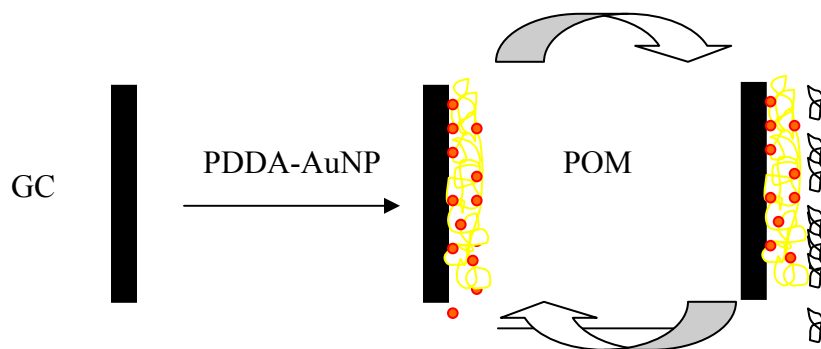


**Figure 5.2** LBL formation of GC/(PDDA-AuNP/POM)<sub>n</sub>

## 5.3 Results and discussion

### 5.3.1 Gold nanoparticle preparation and characterization

The synthesis of gold nanoparticles followed the procedure of Chen<sup>34</sup>, where the reduction of HAuCl<sub>4</sub> to gold nanoparticles occurred in the presence of PDDA under heating. During this reaction, PDDA functionalized as both a stabilizer and a reducing agent. The structure of PDDA is shown in Figure 5.3. However, although this method works well for preparing low concentrations of gold colloid, it is not very efficient for preparing high concentrations. As the LBL assembly process requires concentrated dipping solution<sup>35</sup>, NaBH<sub>4</sub> is used to improve the formation of gold colloid at high concentrations of HAuCl<sub>4</sub>; using NaBH<sub>4</sub> not only shortens the reaction time but also reduces the size of the gold nanoparticles produced. The UV absorption spectrum obtained for the gold nanoparticle solution is shown in Figure 5.4. The strong absorption peak at 516nm is attributed to the plasma resonance of gold nanoparticles. The TEM image of PDDA-Au<sub>NP</sub> and its size distribution diagram are shown in Figure 5.5. The

mean diameter of the gold nanoparticles formed using this procedure was around  $10.58 \pm 2.96$  nm.

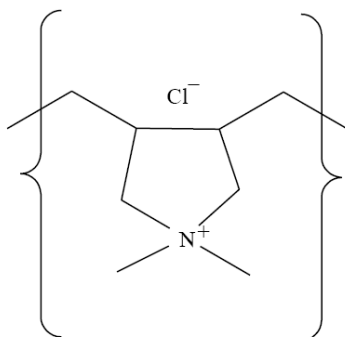


**Figure 5.3.** The molecular structure of PDDA.

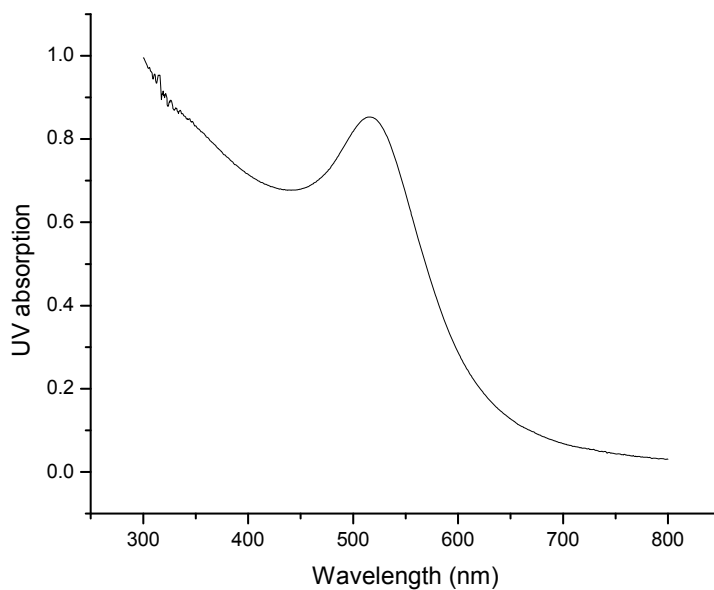
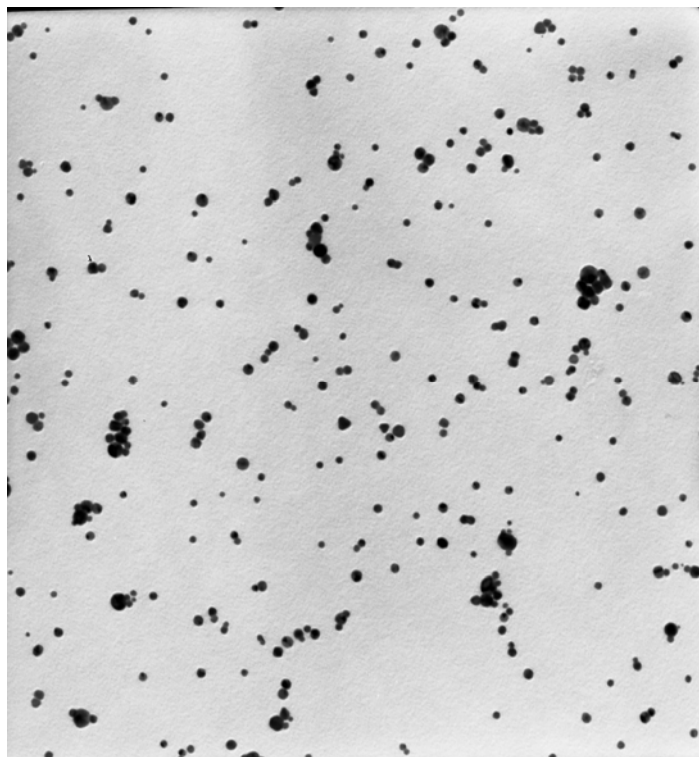
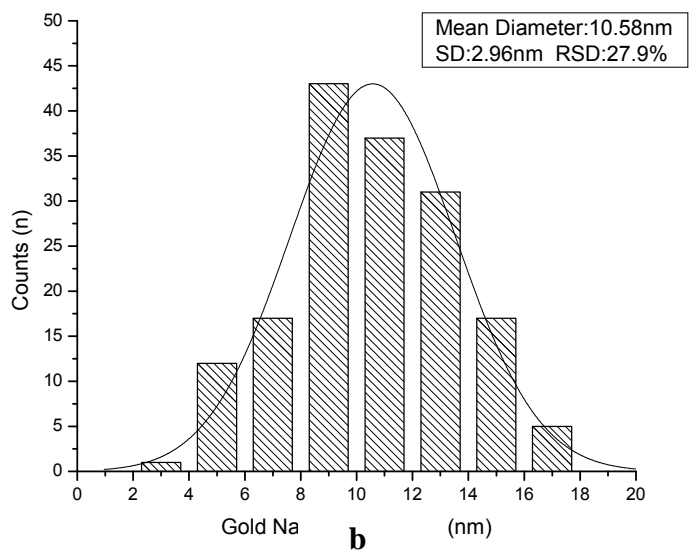


**Figure 5.4** UV-vis absorption spectrum of an aqueous solution of PDDA-protected AuNPs



**a**



**b**

**Figure 5.5** TEM images of PDDA-Au<sub>NP</sub> and its size distribution diagram

### 5.3.2 Characterization of LBL assembly by cyclic voltammetry

The cyclic voltammetry of Cobalt (II)-monosubstituted Dawson-type tungstodiphosphate anion in 0.1 M HClO<sub>4</sub> is shown in Figure 5.6. Two predominant redox couples are observed due to reversible two-electron tungsten (VI—V) reduction<sup>36</sup>. During the cathodic sweep, the peaks occur at C1= -0.15V and C2=-0.44V; during the anodic sweep, the peaks occur at A1=-0.11V; A2=-0.35V corresponding to the two cathodic peaks, respectively. In contrast, the cyclic voltammetry of the LBL assembly with POM as the outmost layer on glassy carbon electrode (Figure 5.7) also shows two sets of redox peaks with reduction peak potential at C1'=-0.14V, C2'=-0.24V and oxidation peak potential at A1'=-0.12V, A2'=-0.22V. The first reduction peak potential of the film is almost the same as that in the solution, while the second reduction peak exhibits a potential shift of about 200 mV to the positive direction. Since there is no evidence in the literature for a 200 mV positive shift of the second 2 electron wave, it is more reasonable to think the two cathodic peaks were due to the splitting from the first cathodic peak in solution voltammetry. The assumption was proofed by integrating the two surface cathodic peaks and each reduction process involves in one electron transfer respectively. The splitting may result from a different local PH Co-POM experienced. In addition, the peak shape in Fig 5.7 is quite symmetrical, with the difference between the reduction and oxidation peak potential for each redox couple A1'/C1', A2'/C2' being around 20mV, the typical redox behavior of the species immobilized on the surface. A calibration curve plotting the first reduction peak currents in Figure 5.7 verses number of (PDDA-Au<sub>NP</sub>/Co-Dawson)<sub>n</sub> bilayers n is shown in Figure 5.8. This shows a linear growth of the POM on the surface with increasing number of bilayers. Although the best fit line

for the six points plotted does not pass through the origin, the best fit line for the first four points does. The slight upturn in the calibration curve is due to the relatively high currents measured at 13 and 17 bilayers, which is probably due to an increase in the surface roughness once a certain amount of gold nanoparticles have been loaded onto the surface.

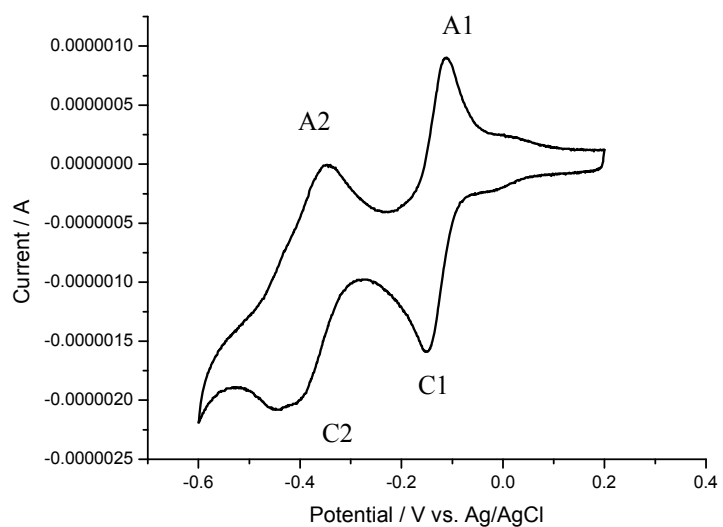


**Figure 5.6** CV of cobalt (II)-monosubstituted Dawson-type tungstodiphosphate anions in 0.1 M HClO<sub>4</sub>. The scan rate is 10mV/s.

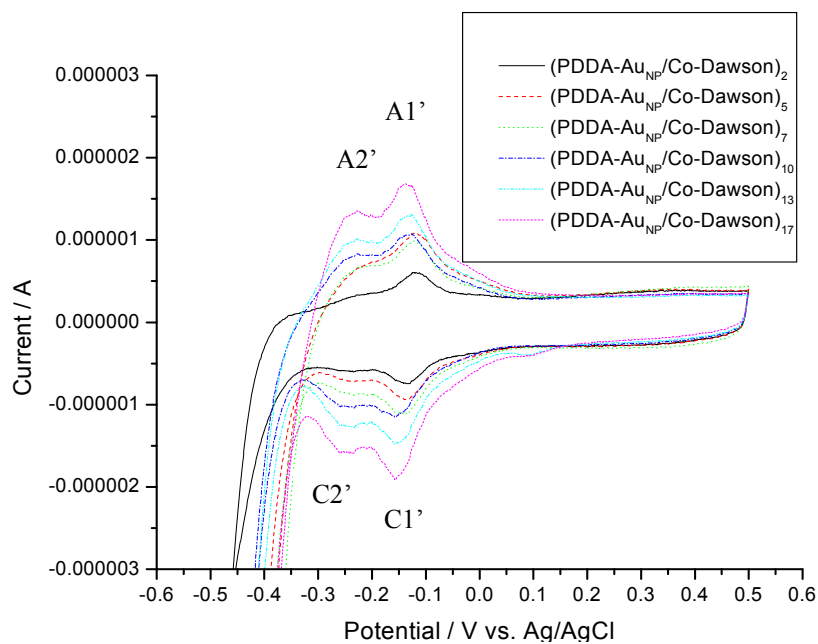


**Figure 5.7** The CVs of GC modified with  $(\text{PDDA-Au}_{\text{NP}}/\text{Co-Dawson})_n$ . From inner to outer trace,  $n=2, 5, 7, 10, 13$ , and  $17$ . The POM layer is the outmost layer.

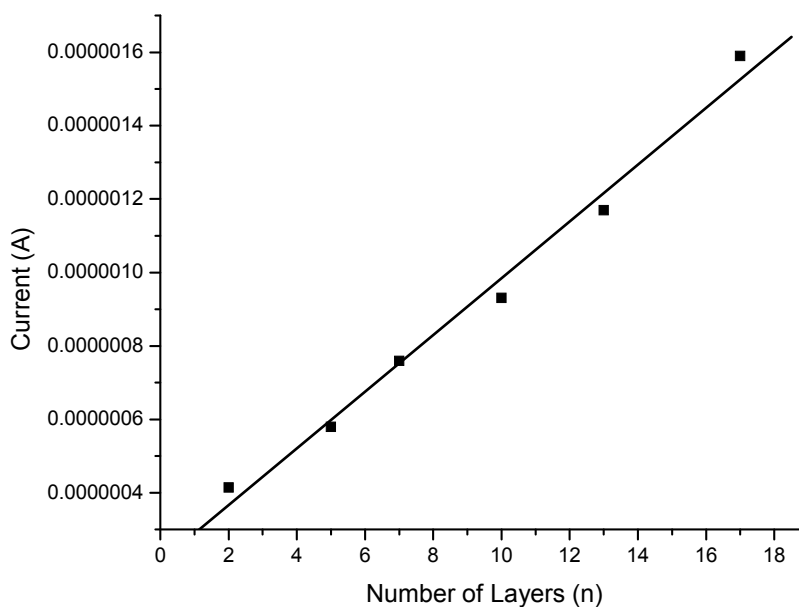


**Figure 5.8** Calibration curve for the first reduction peak current vs. the number of layers

The surface coverage of CoPOM can be calculated using equation 5.1<sup>37</sup>, where  $i_p$  is the first reduction peak current (in Amperes),  $R$  is  $8.314 \text{ J}\cdot\text{K}^{-1}\cdot\text{mol}^{-1}$ ,  $T$  is  $298\text{K}$ ,  $n$  is the number of electrons transferred (1 in this case),  $v$  is the scan rate ( $20\text{mV/s}$ ),  $A$  is the geometric area of the electrode ( $\text{cm}^2$ ), and  $F$  is Faraday's constant  $96485 \text{ C}\cdot\text{mol}^{-1}$ . The number of moles per square cm per layer for the first two layers agrees very well with independent measurements of  $\text{P}_2\text{W}_{18}$  ( $1.5\text{e-}10\text{mol/cm}^2$ ) and it decreases as the number of layers transferred increases. After reaching seven bilayers, the coverage/layer stays at around  $7\text{E-}11 \text{ mol/cm}^2$ . The overall average coverage per layer for POM deposition calculated using this equation was  $8.88\times 10^{-11} \text{ mol/cm}^2$ . The calculations are summarized in Table 5.1.

$$\Gamma = \frac{4i_p RT}{n^2 F^2 vA} \quad \text{Eq. 5.1}$$

**Table 5.1** Summary of POM Surface Coverage

n	$i_p$	coverage ( $\text{mol/cm}^2$ )	coverage/layer ( $\text{mol/cm}^2$ )
2	4.14E-07	3.11525E-10	1.55762E-10
5	5.79E-07	4.35683E-10	8.71366E-11
7	7.59E-07	5.71129E-10	8.15898E-11
10	9.31E-07	7.00554E-10	7.00554E-11
13	1.17E-06	8.80396E-10	6.77228E-11
17	1.59E-06	1.19644E-9	7.03786E-11
average coverage/layer ( $\text{mol/cm}^2$ )			8.87743E-11

### 5.3.3 Characterization of LBL assembly by UV-Vis Absorption

To monitor the growth of gold nanoparticles on the surface, glass slides were used as the substrates for LBL assemblies with PDDA-Au<sub>NP</sub> as the outermost layer. The UV



spectra revealed a strong absorption at 542nm. Compared with the UV absorption spectrum of gold colloid solution, which has a significant absorption at 516nm, the absorption peak of the film was shifted to higher wave numbers, indicating the aggregation of gold nanoparticles on the surface. This was not unexpected, as it is always the case for the condensed phase. Since different glass slides tend to have different absorption background levels, parallel experiments with different numbers of layers of assembly on different glass slides without proper subtraction of the background for each will show no linear correlation between the number of bilayers and their corresponding UV absorptions. However, if the spectrum is recorded for the same substrate as the number of layers increases, the UV absorption exhibits a linear increase, as shown in Figure 5.9. The calibration curve for UV absorption at 542nm versus the number of bilayers, with PDDA-Au<sub>NP</sub> as the outermost layer, is shown in Figure 5.10. As with the results for POM growth, the calibration curve exhibits an upturn after a certain point. Experimentally, the growth of the first several layers proceeds very uniformly; for the same film it shows almost the same spectrum no matter which spot on the glass the UV light passes through. However, this is no longer the case after a certain point, as the growth of PDDA-Au<sub>NP</sub> increases more rapidly due to the increasing surface roughness of the underlying film. Accurate measurements must therefore be achieved by ensuring the UV light passes through the same spot on the glass each time.

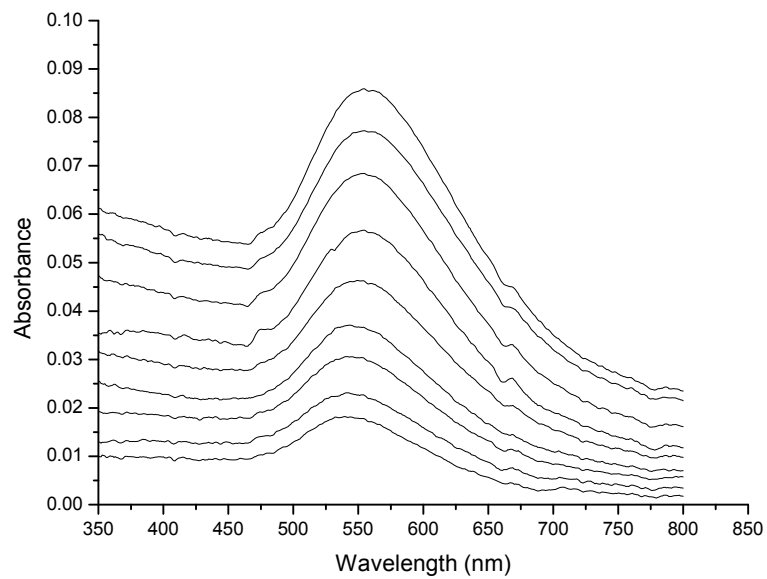


**Figure 5.9** The UV absorption of glass slide modified with (PDDA-Au<sub>NP</sub>/Co-Dawson)<sub>n</sub>. From bottom to top, n= 3,4,5,6,7,8,9,10 and 11. PDDA-Au<sub>NP</sub> is the outermost layer.

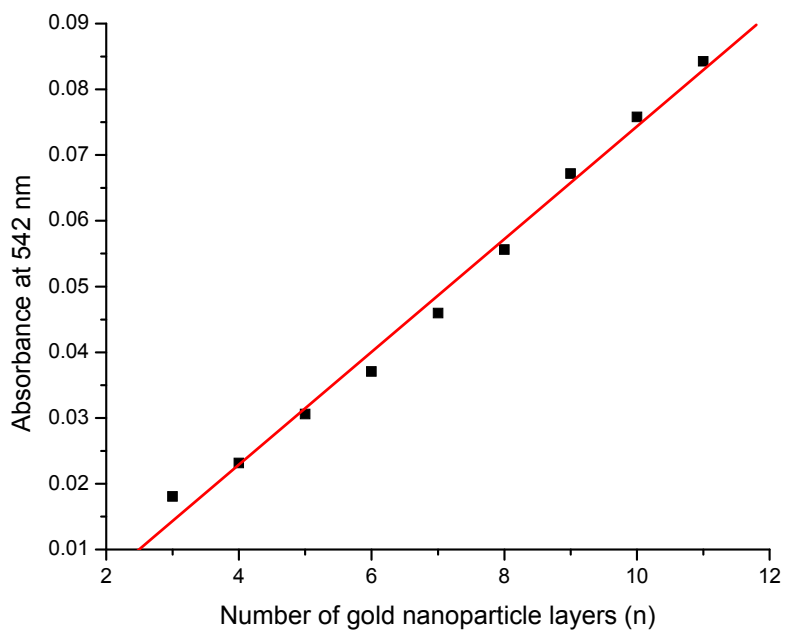


**Figure 5.10** Calibration curve for the absorption at 542nm vs. the number of layers

### 5.3.4 Quantification of Gold Nanoparticles

#### (1) Gold oxide stripping method

In order to quantify the effective surface areas of the gold nanoparticles, the gold oxide stripping peak was measured and analyzed. It has previously been found that when a gold electrode is electrochemically oxidized, it forms a layer of Au oxide film that can be stripped off during the cathodic scan. Based on the coulombs passed through during the process, which can be measured by integrating the area under the stripping peak, the effective gold surface area can be calculated. A theoretical estimate of the surface concentration of Au atoms on a polycrystalline metal depends on the composition of the exposed crystalline planes. A simple geometric calculation shows that a (111) plane exhibits a 60% higher surface concentration of atoms than a (110) plane. Without speculating about the nature of the main plane exposed, an average calculation based on density ( $19.3\text{ g cm}^{-3}$ ) and atomic weight can be utilized. The mean surface concentration of gold atoms calculated using these values is about  $2.5\text{E-}9\text{ mol cm}^{-2}$  for metallic Au, with a mean thickness of  $2.6\text{Å}$  for the top layer. In order to form a single layer coverage ( $\theta=1$ ) of absorbed divalent oxygen, a charge transfer of  $482\mu\text{C/cm}^2$  is needed. For the complete oxidation of the top layer Au to  $\text{Au}_2\text{O}_3$ , a charge transfer of  $723\mu\text{C/cm}^2$  is therefore necessary.<sup>38</sup> Based on the oxidation potential at the point where  $\text{Au}_2\text{O}_3$  was formed, the following equation can be used to calculate the gold surface area.<sup>39</sup>

$$A = \frac{\text{Au oxide reduction charge } (\mu\text{C})}{723(\mu\text{C/cm}^2)} \quad \text{Eq. 5.2}$$

The CV of the LBL assembly modified GC in 0.1 M  $\text{HClO}_4$  is represented by the solid line in Figure 5.11. The oxidation peak is not very obvious, but a reduction peak

shows up at the same potential for the bulk gold electrode (dashed line). The switching potential of 1300mV versus the Ag | AgCl reference electrode was selected based on a consideration of the minimum potential where a complete gold oxide layer can form but PDDA is not damaged. At this potential, the oxidation process completes and is followed by the evolution of oxygen. By using the charge involved in the reduction, the effective surface area of Au<sub>NP</sub> can be calculated based on the above equation. A calibration curve of measured Au<sub>NP</sub> areas versus the number of layers is shown in Figure 5.12. The Au<sub>NP</sub> areas measured are based on a geometric area of 0.071cm<sup>2</sup> (glassy carbon electrode with diameter 3mm). Due to the low concentration of gold nanoparticles on the surface, a glassy carbon electrode with a diameter of 6 mm was used to collect data for samples with 5 and 10 bilayers. Since the growth of the LBL assembly on GC is very uniform, the density of the film is almost the same for the two glassy carbon electrodes. Therefore, according to the ratio of the geometric area of the two electrodes, the area of gold nanoparticles can be converted to one another. Figure 5.12 confirms that the gold loading is increases linearly with the number of bilayers, which is consistent with the results reported in the previous section for UV-vis measurement on glass slides.

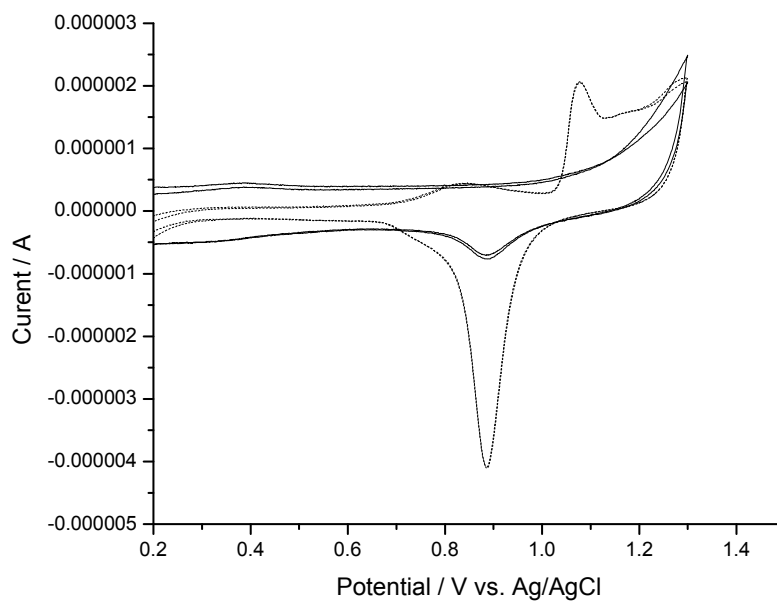


**Figure 5.11** CVs of bulk gold electrode (dashed line) and GC modified with 13 bilayers (solid line) in 0.1 M HClO<sub>4</sub> solution

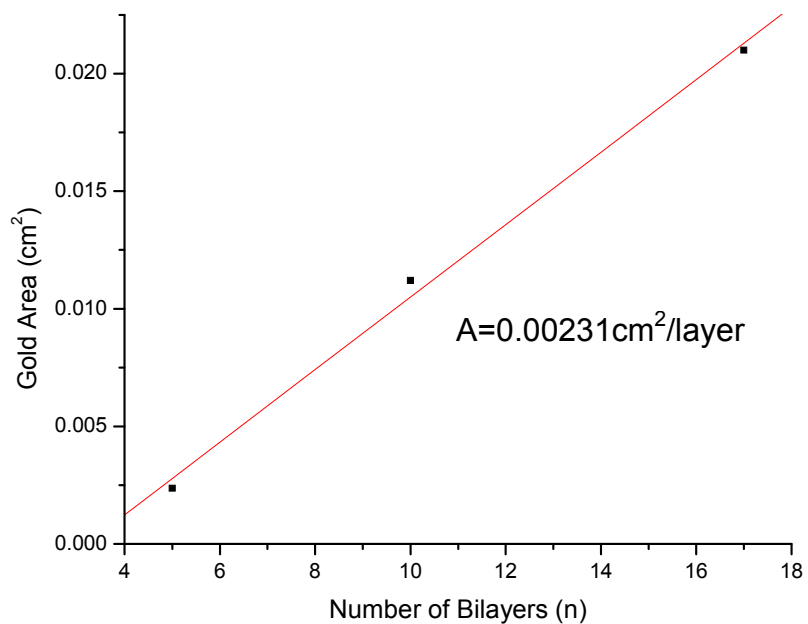


**Figure 5.12** Calibration curve for gold nanoparticle area with increasing number of gold nanoparticle layers

### 5.3.5 Electroactive Probe Measurement

A stable LBL assembly was formed on a glassy carbon electrode based on the above characterization and quantification results. The question that arose regarding how these modified electrodes would behave in the presence of electroactive probes such as  $\text{Ru}(\text{NH}_3)_6\text{Cl}_3$  or  $\text{K}_3\text{Fe}(\text{CN})_6$ . A typical CV for the modified electrode in  $\text{Ru}(\text{NH}_3)_6\text{Cl}_3$  is shown in Figure 5.13, and is characterized by anodic and cathodic waves with an  $E^\circ$  of approximately  $-0.2\text{V}$  and a peak splitting of about  $60\text{mV}$ , consistent with the reversible one electron reduction/oxidation of  $\text{Ru}(\text{NH}_3)_6^{3+}$ . Similar voltammetric behavior has been observed in other systems consisting of metal nanoparticles stabilized by large organic molecules, such as supported DEN monolayers. It should be noted that the shape of the voltammetric waves observed were distorted somewhat near the cathodic limit of the scan, consistent with a change in the double layer capacitance as the potential swept in a negative direction. Similar effects have been seen, for example, in the electrodeposition of metals such as Cu and Cd on Au surfaces, and this is not unexpected given that the  $\text{Ru}(\text{NH}_3)_6^{3+}$  is positively charged.

Interestingly, the peak voltammetric current is not a linear function of the number of LBL layers deposited,  $n$ , as might have been expected (Figure 5.14). Indeed, the first few LBL monolayers deposited significantly reduce the peak current compared to that observed for bare GC. After about 8 LBL bilayers have been deposited, however, the peak current increases approximately linearly with increasing  $n$ . This behavior suggests that the overall electrochemical response of the  $\text{GC}/\{\text{Au-NP}/\text{POM}\}_n$  is made up of two components: one arising from the electroactive GC substrate and the second due to the supported Au-NPs. It is possible to model the attenuation of the electrochemical current

observed at the GC substrate due to the presence of the non-conducting components within the LBL monolayers using an equation of the  $a \cdot \exp(-b \cdot n)$  form where the  $a$  term is the peak current observed at the naked GC electrode,  $b$  is an attenuation factor and  $n$  is the number of LBL layers. In this model, the contribution of the Au-NPs to the total observed faradaic current is assumed to be proportional to the number of LBL layers and therefore has the form  $c \cdot n$ , where  $c$  is a constant of proportionality. The total peak current is described by equation 5.3.

$$i_p = a \cdot \exp(-b \cdot n) + c \cdot n \quad \text{Eq. 5.3}$$

The solid line in Figure 5.14 corresponds to a fit of the experimental data based on this simple model. Initially, owing to the relatively low density of NP in a single PDDA polyelectrolyte layer, the films act to partially block access of the  $\text{Ru}(\text{NH}_3)_6^{3+}$  redox probe to the GC substrate. After a sufficient number of layers have been deposited, however, the voltammetric signal is dominated by contributions from the Au NP, and therefore increases linearly with  $n$  as expected. These experiments demonstrate that the redox probe molecules have access both to the electroactive GC substrate as well as the Au-NPs.

To gain further insight into the behavior of redox-active molecules within these GC/ $\{\text{Au-NP/POM}\}_n$  films, a combination of a rotating disk voltammetry (RDV) and chronoamperometry was used to measure the diffusion coefficient of the  $\text{Ru}(\text{NH}_3)_6^{3+}$  probe molecule in the films. First, the chronoamperometric response of the thin film electrode was measured in a quiescent solution; a plot of  $i_p$  as a function of  $t^{-1/2}$  yielded a value for the Cottrell slope,  $m_{\text{cottrell}}$ . Next, RDV measurements were carried out using the

same solution, and a plot of  $i_p^{-1}$  versus  $\omega^{-1/2}$  yielded the Koutecky-Levich slope,  $m_{K-L}$ . Finally, the diffusion coefficient was calculated from the product of Koutecky-Levich slope to the Cottrell slope, as shown in Equations 5.4 through 5.7.

$$m_{K-L} = \frac{1}{0.62nFAD_o^{2/3}v^{-1/6}C_o^*} \quad \text{Eq. 5.4}$$

$$m_{cottrell} = \frac{nFAD_o^{1/2}C_o^*}{\pi^{1/2}} \quad \text{Eq. 5.5}$$

$$P = m_{K-L} \times m_{cottrell} = \frac{1}{0.62D_o^{1/6}v^{-1/6}\pi^{1/2}} \quad \text{Eq. 5.6}$$

$$D_o = \left( \frac{v^{1/6}}{0.62P\pi^{1/2}} \right)^6 \quad \text{Eq. 5.7}$$

The advantage of this approach is that no independent information regarding the electrochemically active surface area of the Au NPs is required to calculate  $D_o$ . The experimental data are summarized in Table 5.2. In general, the diffusion coefficient decreases monotonically as a function of  $n$ .

**Table 5.2** Diffusion Coefficients of  $\text{Ru}(\text{NH}_3)_6\text{Cl}_3$  at bare GC and LBL modified GC

layers	Cottrell slope	K-L Slope	Diffusion Coefficient ( $\text{cm}^2/\text{s}$ )
bare	2.57E-05	127971.6927	4.543E-06
3layers	2.94E-05	1.18E+05	3.328E-06
7layers	3.28E-05	111207.642	2.42E-06
13layers	3.94E-05	125330.2026	3.941E-07
20layers	3.28E-05	125448.3035	1.182E-06



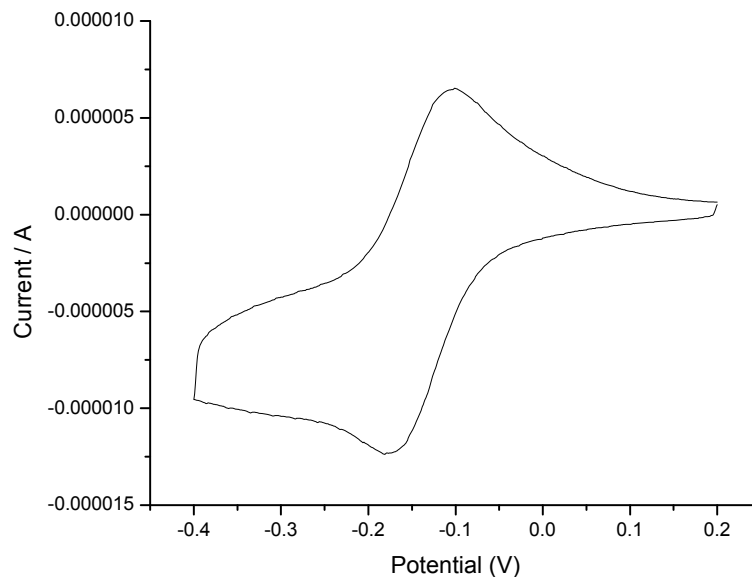


**Figure 5.13** Cyclic Voltammetry of GC/(PDDA-AuNP/Co-Dawson)<sub>13</sub> electrode in 1mM Ru(NH<sub>3</sub>)<sub>6</sub><sup>3+</sup> solution and 0.1 M NaClO<sub>4</sub>. The scan rate is 10 mV/s.

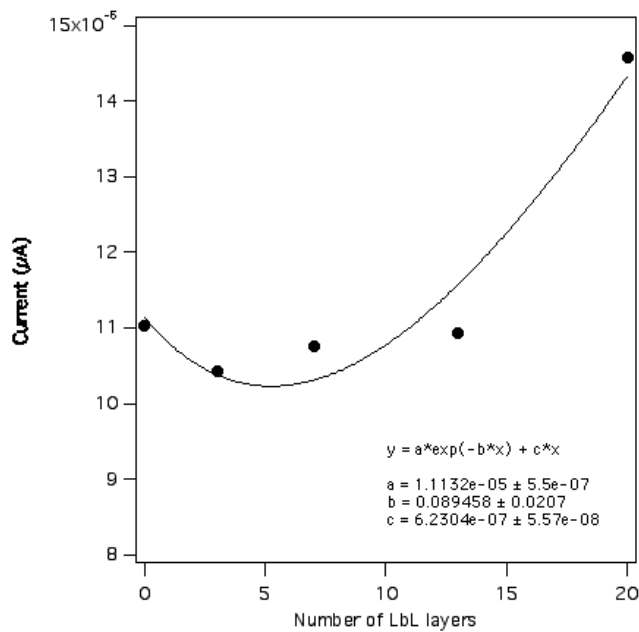


**Figure 5.14** Cathodic peak current of GC/(PDDA-AuNP/Co-Dawson)<sub>n</sub> electrode in 1mM Ru(NH<sub>3</sub>)<sub>6</sub><sup>3+</sup> solution and 0.1 M NaClO<sub>4</sub> at different *n*. Scan rate is 10mV/s

### 5.3.6 Oxygen Reduction of GC Modified LBL Assembly

The oxygen reduction of the prepared LBL assembly for different numbers of bilayers is shown in Figure 5.15. Interestingly, as the number of bilayers increases, the half-wave potential of the oxygen reduction keeps shifting to the right, reaching the limiting potential at 13 bilayers. Above this point, for instance at 17 bilayers, the oxygen reduction potential remains in the same location, although the peak current continues to increase. Another interesting feature is the way the current shape changes for different numbers of bilayers. For bare GC, (PDDA-Au<sub>NP</sub>/Co-Dawson)<sub>n</sub> when n=7, 13, and 17, the oxygen reduction shows the typical irreversible peak shape of a cyclic voltammogram, however for (PDDA-Au<sub>NP</sub>/Co-Dawson)<sub>n</sub> when n = 3, and 5, no peak is observed. Control experiments using either Wells-Dawson POM or Ru-Dawson POM instead of Co-Dawson are shown in Figure 5.16. For the Wells-Dawson POM GC, the limiting current is almost the same as for the (PDDA-Au<sub>NP</sub>/Co-Dawson)<sub>13</sub> electrode, although the half-wave potential has shifted to the negative direction by about 50mV; for the Ru-Dawson POM modified GC, the onset potential of oxygen reduction starts earlier but the kinetics are sluggish, suggesting a different mechanism is involved; the mechanism for oxygen reduction with Ru-Dawson POM dissolved in solution is known to involve a two-two electron transfer process. Therefore these results are in good agreement with our previous study<sup>24</sup>

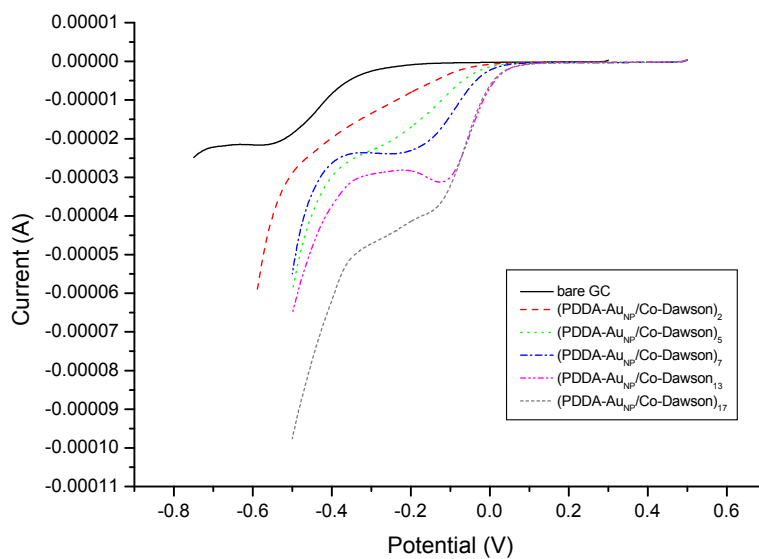


**Figure 5.15** Oxygen reduction in 0.1M HClO<sub>4</sub> at GC electrode modified with different numbers of bilayer film. The outermost layer is POM. The potential scan rate is 20mV/s.

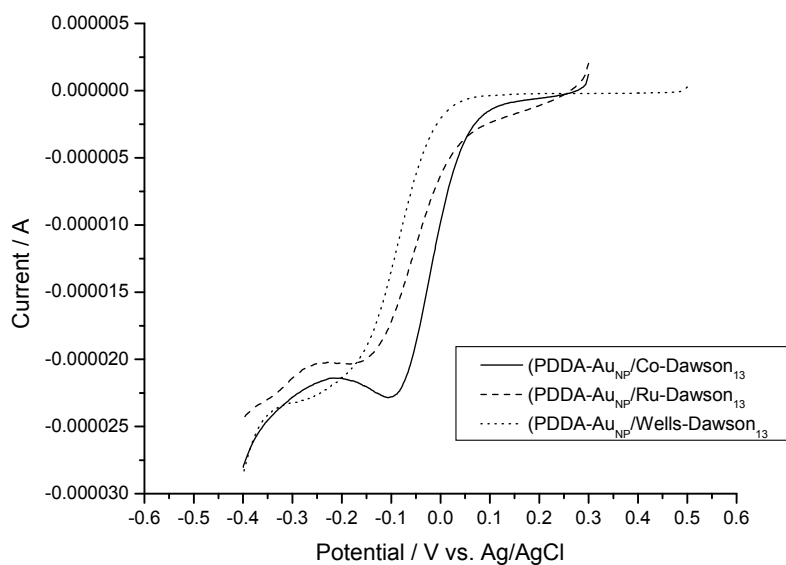


**Fig 5.16** Oxygen reduction in 0.1M HClO<sub>4</sub> at GC electrode modified with different POM LBL assemblies. The outermost layer is POM. The potential scan rate is 10mV/s.

In order to identify the mechanism for the electrocatalytic reduction of oxygen at (PDDA-Au<sub>NP</sub>/Co-Dawson)<sub>n</sub> modified electrodes, electrochemical measurements were carried out using rotated disk voltammetry. At a rotated disk electrode (RDE), the mass transfer limited current ( $i_L$ ) depends only on the angular rotational velocity ( $\omega$ ) and the bulk concentration of oxygen in solution (mol/cm<sup>3</sup>), which is expressed as the Levich equation 5.8:

$$i_L = 0.62 n F A D^{2/3} C_{O_2}^b \nu^{-1/6} \omega^{1/2} \quad \text{Eq. 5.8}$$

Where  $n$  is the number of electrons transferred,  $F$  is Faraday's constant,  $A$  is the electrode area,  $\nu$  is the kinematic viscosity, and  $D$  is the diffusion coefficient. For all calculations, the angular velocity is taken as  $\text{rad}\cdot\text{s}^{-1} = (2\pi/60)\cdot f$ , where  $f$  is the frequency of rotation in rpm, the value for  $\nu$  is  $0.01\text{cm}^2\text{s}^{-1}$ ,  $D$  is  $1.8\text{E}-5\text{cm}^2\text{s}^{-1}$  and  $C_{O_2}^b$  is  $1.13\text{E}-6\text{mol}\cdot\text{cm}^{-3}$ .<sup>40</sup> A linear plot of  $i_L$  vs.  $\omega^{1/2}$  (a Levich Plot) implies that the electrocatalytic reaction is faster than the rate of substrate delivery to the electrode, so that the current is determined only by how fast the substrate is transported to the surface.

Figure 5.17 shows the RDE linear sweep voltammetry of oxygen reduction at a (PDDA-Au<sub>NP</sub>/Co-Dawson)<sub>13</sub> modified electrode. At lower rotation rates, the current begins at zero and then rises sharply at the reduction potential of oxygen before peaking and finally diminishing to a stable plateau value followed by an increase in the current due to hydrogen evolution. At higher rotation rates, the effective concentration of oxygen at the electrode surface increases so the limiting current rises as well, although the plateau becomes less obvious. Interestingly, both higher rotation rates and a lower number of bilayers lead to greater deviations from the idealized response, which is

illustrated in the Levich Plots shown in Figure 5.18. Under strictly diffusion controlled conditions, these plots are linear and pass through the origin. Here, however, the electrocatalysis cannot keep up with the increased flux of oxygen at either high rotation rates or small amounts of gold loading so the currents level off.

For a reaction mediated by a surface-bound species (in this case mainly gold nanoparticles), the kinetically controlled current ( $i_k$ ) is given by the following equation:

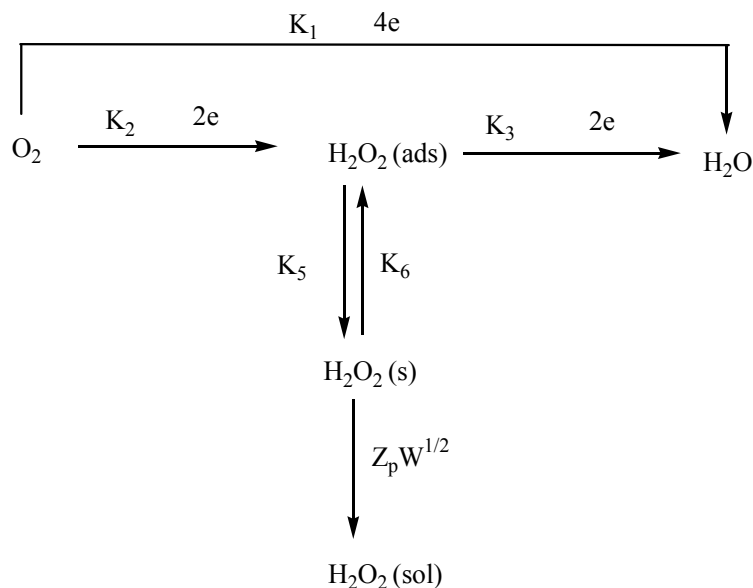
$$i_k = nFAC_{O_2}^b \Gamma k_{obs} \quad \text{Eq. 5.9}$$

Where  $\Gamma$  is the surface coverage of the catalyst bound to the electrode surface, and  $k_{obs}$  is the pseudo second order rate constant. Combining equations 5.8 and 5.9 leads to the Koutecky-Levich expression 5.10, which describes the overall RDE plateau current for the electrocatalytic reaction:

$$\frac{1}{i_{lim}} = \frac{1}{i_L} + \frac{1}{i_k} = \frac{1}{0.62nFAD^{2/3}C_{O_2}^b\nu^{-1/6}\omega^{1/2}} + \frac{1}{nFAC_{O_2}^b\Gamma k_{obs}} \quad \text{Eq. 5.10}$$

According to this expression, a plot of  $i_{lim}$  vs.  $\omega^{-1/2}$  should yield a straight line whose slope is related to the number of electrons transferred ( $n$ ) and whose intercept gives the product  $\Gamma \cdot k_{obs}$ . Because both POM and gold surface concentrations can be quantified electrochemically,  $k_{obs}$  can be directly calculated using RDE voltammetry. Figure 5.19 shows Koutecky-Levich plots for the electrocatalytic reduction of saturated oxygen at different numbers of bilayers (PDDA-Au<sub>NP</sub>/Co-Dawson)<sub>n</sub>, with  $n=3$  and  $n=13$ . The measurements on these two electrodes yield a straight line that is almost parallel to the theoretical curve drawn for  $n = 4$ , but with decreasing intercepts as the number of bilayers increases. The actual determined electron transfer number of the (PDDA-Au<sub>NP</sub>/Co-Dawson)<sub>13</sub> electrode is around 3.7 taking the average of calculated numbers

from a series of Koutecky-Levich plots at various potentials (-0.18V~-0.35V). From the resolved electron transfer number, the pathways for oxygen electrochemical reduction can be determined based on the Wroblowa<sup>41</sup> scheme shown in Scheme 5.1. The oxygen reduction reaction can proceed either through a direct four-electron pathway with  $k_1$  or two sequential two-electron steps via the formation of adsorbed  $H_2O_2$  ( $k_2$ ), which can undergo several reactions: (i) catalytic decomposition ( $k_4$ ), (ii) desorption ( $k_5$ ) and diffusion away from the surface into the bulk solution, and (iii) electrochemical reduction ( $k_3$ ). More complex mechanistic schemes with a larger number of intermediates have been discussed by Adzic<sup>42</sup>. The results here clearly suggest that the electrochemical reduction of oxygen on  $(PDDA-Au_{NP}/CoDawson)_n$  undergoes the  $k_1$  four-electron pathway mechanism. The detailed mechanism for  $(PDDA-Au_{NP}/Wells-Dawson)_n$  is not completely addressed here as it is beyond the scope of the current study.



**Scheme 5.1** Reaction scheme for oxygen electroreduction according to Wroblowa et al.<sup>41</sup>

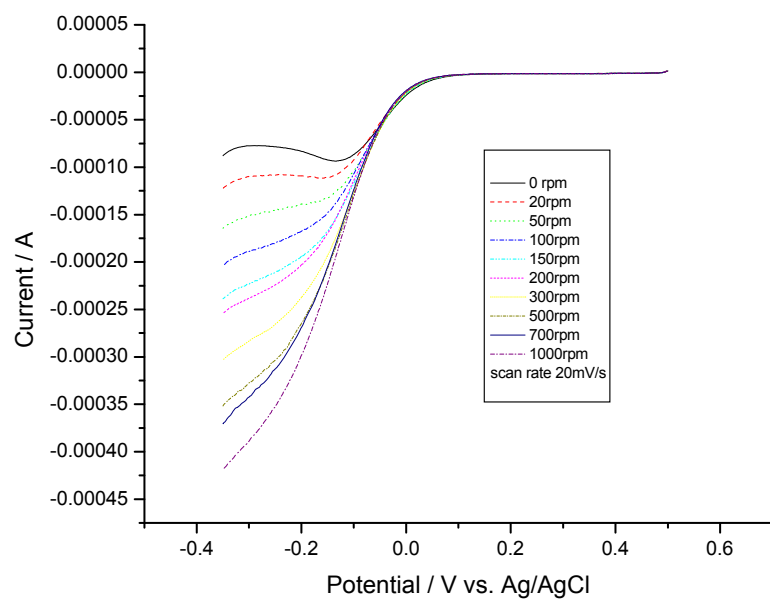


**Figure 5.17** Reduction of  $O_2$  at a rotating GC disk electrode coated with 13 bilayers.

Current-potential curves in  $O_2$ -saturated 0.1 M  $HClO_4$ , scan rate =  $20 \text{ mV s}^{-1}$ .

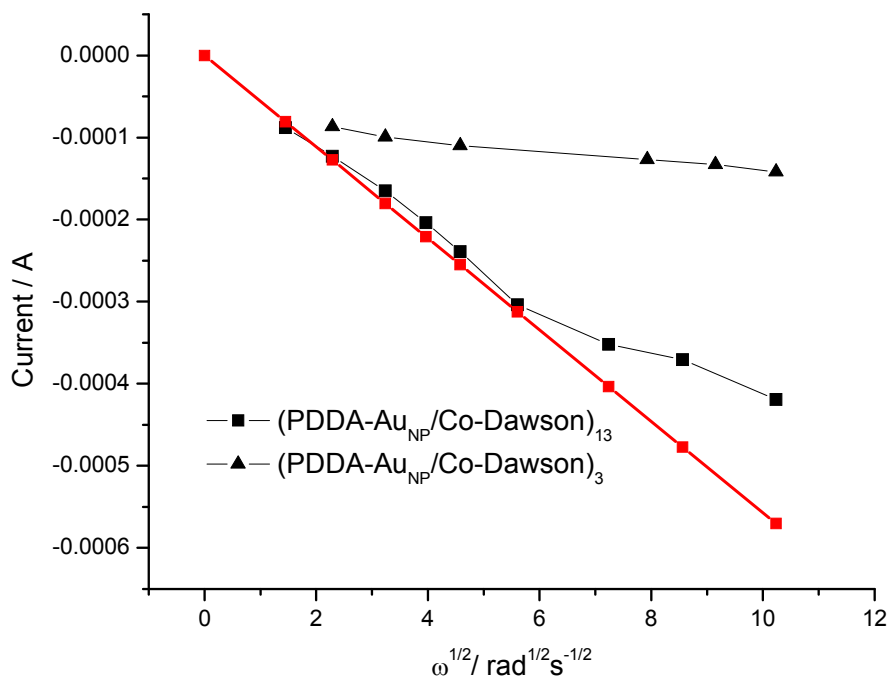


**Figure 5.18** Levich plot of RDE measurement with  $(PDDA-Au_{NP}/Co-Dawson)_n$ ,  $n=3$  and

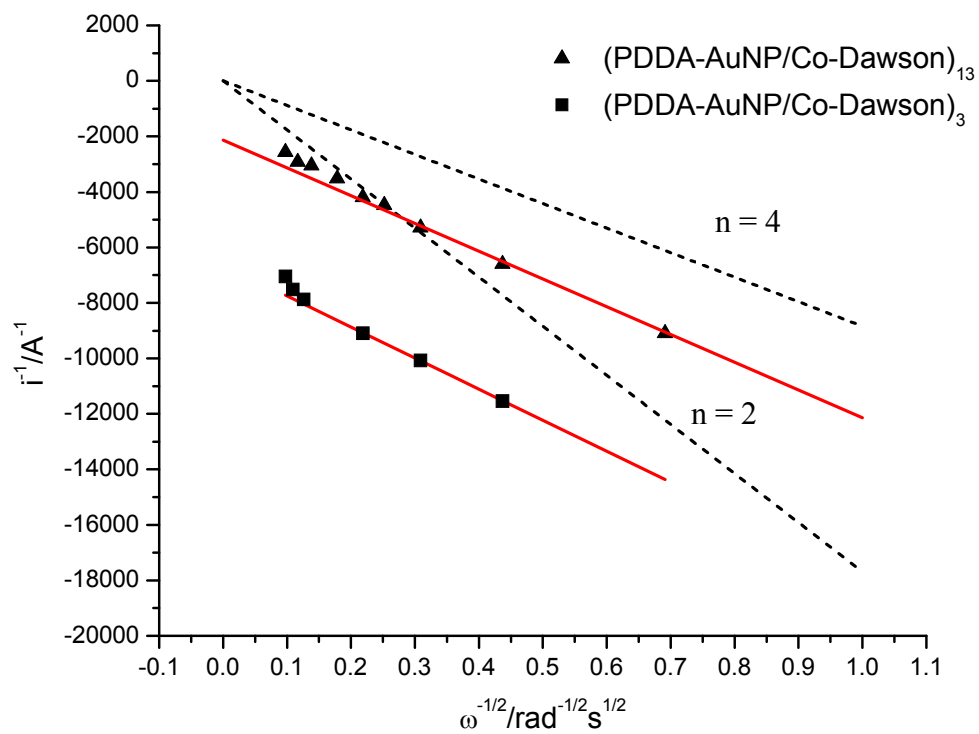


**Figure 5.19** Koutecky-Levich plot of RDE measurements with (PDDA-Au<sub>NP</sub>/Co-Dawson)<sub>n</sub>, n=3 and 13



Another important value that can be obtained from the Koutecky-Levich plot is the kinetic current  $i_k$ . Based on  $i_k$ , a Tafel plot can be constructed and the specific activity calculated. It is interesting to note that as the number of layers increases the intercepts of the Koutecky –Levich plot become smaller, which means the kinetic currents become larger. This differs from the results observed for the electroactive probe measurement, where the intercepts obtained for different numbers of bilayers almost overlapped. This is due to the same kinetics as in the  $\text{Ru}(\text{NH}_3)_6\text{Cl}_3$  reduction on a GC and gold surface, although here the kinetics of oxygen reduction on gold are faster than on GC. Therefore, as the number of bilayers increases, the amount of gold loading increases and the oxygen reduction on gold becomes more dominant.

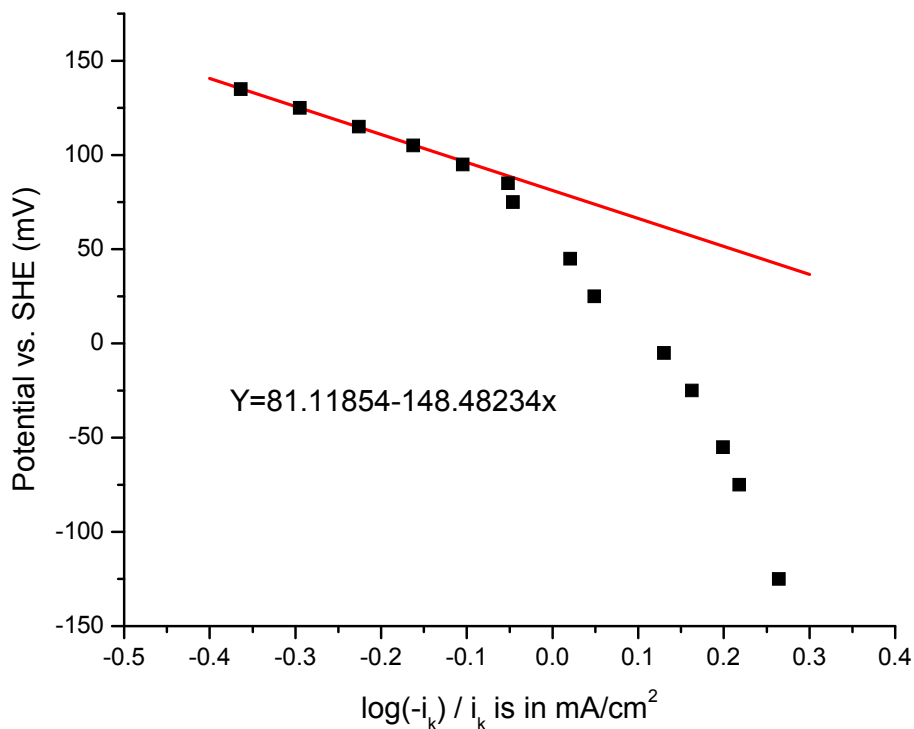


**Figure 5.20** Tafel plot of RDE measurements with  $(\text{PDDA-Au}_{\text{NP}}/\text{CoDawson})_{13}$

The Tafel plot of (PDDA-Au<sub>NP</sub>/CoDawson)<sub>13</sub> is shown in Figure 5.20 and has a slope of  $-148 \text{ mV} \cdot \text{dec}^{-1}$ . This value is in good agreement with values that have been published in the literature of  $130 \text{ mV} \cdot \text{dec}^{-1}$  and  $110 \text{ mV} \cdot \text{dec}^{-1}$  for an Au(Cu)/GC electrode and a bulk Au electrode respectively.<sup>43-45</sup> This indicates that the overall mechanism of oxygen reduction for (PDDA-Au<sub>NP</sub>/CoDawson)<sub>13</sub> is similar to that for bulk gold, although there is no retardation of oxygen reduction kinetic currents.

The specific activities (SAs) of the (PDDA-Au<sub>NP</sub>/POM)<sub>n</sub> are summarized in Table 5.3. For an accurate analysis of thin-film RDE measurements, three criteria must be satisfied based on Mayrhofer's work.<sup>46</sup> "First, the theoretical diffusion limited current density needs to be measured, secondly the catalytic activity has to be normalized that is independent of the catalyst loading, and thirdly the currents approximately half that of the diffusion limited current should be used to calculate the catalytic activity" Although these criteria are based on a Pt-Nafion<sup>TM</sup> membrane, they provide useful guidelines for other comparable systems. In this case, the LBL assembly process was applied to form a film that is very thin, uniform and stable. Under such conditions, criteria one and two can be easily satisfied. For the last criteria, the kinetic current at  $-0.1 \text{ V}$  vs Ag | AgCl was used to calculate catalytic activity (SA value). Although the half-wave potential was around  $-0.05$ , the currents could not be used at this potential due to excessive noise. In addition, all the literature values for gold systems are based on measurements below  $-0.1 \text{ V}$ . In order to compare our results with those reported in the literature, the use of a current at  $-0.1 \text{ V}$  was considered to be the best choice. As this potential deviates significantly from the equilibrium potential, the catalytic activity is generally described as the specific current

density (specific activity) at a certain potential in the kinetic region, rather than the exchange current density at zero overpotential.

**Table 5.3** Summary of Kinetic Currents ( $i_k$ ) and Specific Activities (SAs) for Bulk Au and (PDDA-AuNP/CoDawson)<sub>13</sub> /GC at -0.1V

Catalyst	$i_k$ (mA)	at -0.1V /Ag   AgCl	
		Effective Area(cm <sup>2</sup> )*	SA(mA/cm <sup>2</sup> )
(PDDA-Au <sub>NP</sub> /CoDawson) <sub>13</sub>	0.143	0.0339	4.22
(PDDA-Au <sub>NP</sub> /CoDawson) <sub>3</sub>	6.57E-03	0.0078	0.84
(PDDA-Au <sub>NP</sub> /WellsDawson) <sub>13</sub>	0.121	0.0339	3.57
bulk gold <sup>47</sup>	0.0955	0.0964	0.99
Au nanoparticles-deposited electrode <sup>47</sup>	0.14454	0.0961	1.50
bulk gold <sup>43</sup>			1.58

\* The effective areas were determined using Cu UPD and Au oxide stripping.

Table 5.3 shows that the specific activities of (PDDA-Au<sub>NP</sub>/POM)<sub>13</sub> were 4 times greater than that of a bulk gold electrode. This increase can partly be attributed to the nano-sized nature of the gold nanoparticles<sup>47-51</sup>. Although bulk Au is known not to adsorb molecular oxygen at room temperature<sup>52</sup>, recent experimental and theoretical studies have indicated that both Au nanoparticles and very thin Au films exhibit extraordinary catalytic properties that are linked to increased molecular (or even dissociative) oxygen adsorption.<sup>53-57</sup> This behavior is further enhanced in the presence of CoDawson POM due to the fact that POM performs well for absorbed O<sub>2</sub> bond scission while Au does not. A control experiment using gold nanoparticle and Wells Dawson compound was also conducted and the SA value was calculated. Interestingly, the

specific activity of the CoDawson composite shows an improvement of a factor of 1.2 over that of the Wells Dawson composite, which is consistent with the increase of a factor of 1.3 in the oxygen reduction current at -0.1V (13 bilayers) observed in the cyclic voltammetry measurements. These results are also in good agreement with our previously published study of POM/Au interactions.<sup>24</sup>

#### 5.4 Conclusions

An LBL assembly was fabricated using PDDA stabilized gold nanoparticles and Cobalt monosubstituted Wells Dawson compound on a glassy carbon electrode. The thin film was characterized with UV and cyclic voltammetry, revealing a linear growth of film with increasing number of layers. The modified glassy carbon electrode showed good catalytic ability towards oxygen reduction. With increasing number of layers, the oxygen reduction potential shifted steadily to the positive direction until at about thirteen layers, the electrode reached the limiting potential. The (PDDA-Au<sub>NP</sub>/Co-POM)<sub>13</sub> electrode is therefore a good candidate for oxygen reduction applications and is well able to compete with the bulk gold electrode, exhibiting improved kinetics. In contrast, the electrode fabricated from gold nanoparticles and Wells-Dawson POM or Ru-Dawson showed relatively slow kinetics. These results indicate that cobalt substituted Dawson plays an important role in the oxygen reduction process.

#### 5.5 References

1. Lima, F. H. B.; Zhang, J.; Shao, M. H.; Sasaki, K.; Vukmirovic, M. B.; Ticianelli, E. A.; Adzic, R. R., *J. Solid State Electrochem.* **2008**, 12, (4), 399-407.
2. Lima, F. H. B.; Zhang, J.; Shao, M. H.; Sasaki, K.; Vukmirovic, M. B.; Ticianelli, E. A.; Adzic, R. R., *J. Phys. Chem. C* **2007**, 111, (1), 404-410.

3. Sasaki, K.; Zhang, L.; Adzic, R. R., *Physical chemistry chemical physics : PCCP* **2008**, 10, (1), 159-67.
4. Shao, M. H.; Sasaki, K.; Liu, P.; Adzic, R. R., *Z. Phys. Chem. (Muenchen, Ger.)* **2007**, 221, (9-10), 1175-1190.
5. Vukmirovic, M. B.; Zhang, J.; Sasaki, K.; Xu, Y.; Nilekar, A. U.; Mavrikakis, M.; Uribe, F.; Adzic, R. R., *Proc. - Electrochem. Soc.* **2006**, 2005-11, (Electrocatalysis), 188-199.
6. Zhang, J.; Lima, F. H. B.; Shao, M. H.; Sasaki, K.; Wang, J. X.; Hanson, J.; Adzic, R. R., *J. Phys. Chem. B* **2005**, 109, (48), 22701-22704.
7. Zhang, J.; Vukmirovic, M. B.; Sasaki, K.; Uribe, F.; Adzic, R. R., *J. Serb. Chem. Soc.* **2005**, 70, (3), 513-525.
8. Zhang, J.; Sasaki, K.; Sutter, E.; Adzic, R. R., *Science* **2007**, 315, (5809), 220-222.
9. Markovic, N. M. R., V.; Ross, P. N., Jr., *Catalysis and Electrocatalysis at Nanoparticle Surfaces* **2003**, 2003, 311-342.
10. Alayoglu, S. N., Anand U.; Mavrikakis, Manos; Eichhorn, Bryan., *Nat. Mater.* **2008**, 7, (4), 333-338.
11. Sasaki, K.; Mo, Y.; Wang, J. X.; Balasubramanian, M.; Uribe, F.; McBreen, J.; Adzic, R. R., *Electrochim. Acta* **2003**, 48, (25-26), 3841-3849.
12. Shao, M. H.; Huang, T.; Liu, P.; Zhang, J.; Sasaki, K.; Vukmirovic, M. B.; Adzic, R. R., *Langmuir* **2006**, 22, (25), 10409-10415.
13. Kowalewska, B.; Skunik, M.; Karnicka, K.; Miecznikowski, K.; Chojak, M.; Ginalska, G.; Belcarz, A.; Kulesza, P. J., *Electrochim. Acta* **2008**, 53, (5), 2408-2415.

14. Tributsch, H.; Koslowski, U. I.; Dorbandt, I., *Electrochim. Acta* **2008**, 53, (5), 2198-2209.
15. Xie, X.-Y.; Ma, Z.-F.; Ma, X.-X.; Ren, Q.; Schmidt, V. M.; Huang, L., *J. Electrochem. Soc.* **2007**, 154, (8), B733-B738.
16. Grigoriu, M. A.; Villers, D.; Jaouen, F.; Dodele, J. P., *Proc. - Electrochem. Soc.* **2006**, 2005-11, (Electrocatalysis), 242-253.
17. Yuasa, M.; Oyaizu, K.; Yamaguchi, A.; Imai, T.; Kitao, M., *Kobunshi Ronbunshu* **2006**, 63, (3), 182-188.
18. Artyushkova, K.; Olson, T.; Fulghum, J.; Atanassov, P., *Prepr. Symp. - Am. Chem. Soc., Div. Fuel Chem.* **2006**, 51, (1), 320-321.
19. Oyaizu, K.; Yuasa, M., *Maku* **2005**, 30, (5), 254-259.
20. Yuasa, M.; Yamaguchi, A.; Oyaizu, K.; Fujito, Y.; Kitao, M.; Sato, T., *Polym. Adv. Technol.* **2005**, 16, (9), 702-705.
21. Birss, V. I.; Sirk, A. H. C.; Campbell, S. A., *Proc. - Electrochem. Soc.* **2005**, 2002-31, (Proton Conducting Membrane Fuel Cells III), 89-98.
22. Fuerte, A.; Corma, A.; Iglesias, M.; Morales, E.; Sanchez, F., *Catal. Lett.* **2005**, 101, (1-2), 99-103.
23. Khorasani-Motlagh, M.; Noroozifar, M.; Ghaemi, A.; Safari, N., *J. Electroanal. Chem.* **2004**, 565, (1), 115-120.
24. Sankarraj Anand, V.; Ramakrishnan, S.; Shannon, C., *Langmuir* **2008**, 24, (3), 632-634.
25. Vernon, D. R.; Meng, F.; Dec, S. F.; Williamson, D. L.; Turner, J. A.; Herring, A. M., *J. Power Sources* **2005**, 139, 141-151.

26. Khenkin, A. M.; Weiner, L.; Wang, Y.; Neumann, R. J., *J. Am. Chem. Soc.* **2001**, 123, 8531-8542.
27. Keita, B.; Nadjo, L., *J. Electroanal. Chem.* **1987**, 217, 287-304.
28. Kuhn, A.; Anson, F. C., *Langmuir* **1996**, 12, 5481-5488.
29. Ernst, A. Z.; Zoladek, S.; Wiaderek, K.; Cox, J. A.; Kolary-Zurowska, A.; Miecznikowski, K.; Kulesza, P. J., *Electrochim. Acta* **2008**, 53, 3924-3931.
30. Ernst, A. Z.; Sun, L.; Wiaderek, K.; Kolary, A.; Zoladek, S.; Kulesza, P. J.; Cox, J. A., *Electroanalysis* **2007**, 19, 2103 – 2109.
31. Troupis, A.; Hiskia, A.; Papaconstantinou, E., *Angew. Chem. Int. Ed.* **2002**, 41, (11), 1911-1914.
32. Kharat, A. N. P., P.; Badalyan, A.; Abedini, M.; Amini, M. M., *J. Mol. Catal. A: Chem.* **2001**, 175, 277-283.
33. Liu, H.; Yue, B.; Sun, W.; Chen, Z.; Jin, S.; Deng, J.; Xie, G., *Transition Metal Chemistry* **1997**, 22, 321-323.
34. Chen, H.; Wang, Y.; Wang, Y.; Dong, S.; Wang, E., *Polymer* **2006**, 47, 763-766.
35. Decher, G., *Science* **1997**, 277, 1232-1237.
36. Samonte, J. L.; Pope, M. T., *Can. J. Chem.* **2001**, 79, 802-808.
37. Wang, B.; Vyas, R. N.; Shaik, S., *Langmuir* **2007**, 23, 11120-11126.
38. Urs Oesch, J. J., *Electrochim. Acta* **1983**, 28, (9), 1237-1246
39. Zou, S. K. a. S., *J. Phys. Chem. B* **2005**, 109, 15707-15713.
40. Alexeyeva, N.; Lasksonen, T.; Kontturi, K.; Mirkhalaf, F.; Schiffrin, D. J.; Tammeveski, K., *Electrochem. Commun.* **2006**, 8, 1475-1480.
41. Wroblowa, H. S.; Pan, Y. C.; Razumney, G., *J. Electroanal. Chem.* **1976**, 69, 195.

42. Vesovic, V.; Anastasijevic, N.; Adzic, R. R., *J. Electroanal. Chem. Interfacial Electrochem.* **1987**, 218, (1-2), 53-63.
43. Tegou, A.; Papadimitriou, S.; Pavlidou, E.; Kokkinidis, G.; Sotiropoulos, S., *J. Electroanal. Chem.* **2007**, 608, 67-77.
44. Hoare, J. P., *Electrochim. Acta* **1966**, 203, 311.
45. Damjanovic, A.; Brusic, V., *Electrochim. Acta.* **1967**, 12, 1171.
46. Mayrhofer, K. J. J.; Strmcnik, D.; Blizanac, B. B.; Stamenkovic, V.; Arenz, M.; Markovic, N. M., *Electrochim. Acta* **2008**, 53, 3181-3188.
47. El-Deab, M. S.; Ohsaka, T., *Electrochim. Acta* **2002**, 47, 4255-4261.
48. El-Deab, M. S.; Ohsaka, T., *Electrochim. Acta.* **2007**, 52, 2166.
49. El-Deab, M. S.; Ohsaka, T., *Electrochem. Commun.* **2005**, 7, 888.
50. Sarapuu, A.; Tammeveski, K.; Tenno, T. T.; Sammelselg, V.; Kontturi, K.; Schiffrin, D. J., *Electrochem. Commun.* **2005**, 7, 888.
51. Guerin, S.; Hayden, B. E.; Pletcher, D.; Rendall, M. E.; Suchsland, J.-P., *J. Combust.Chem.* **2006**, 8, 679.
52. Chester, M. A.; Somorjai, G. A., *Surf. Sci.* **1975**, 52, 21.
53. Haruta, M.; Tsubota, S.; Kobayashi, T.; Kageyama, H.; Genet, M. J.; Delmon, B., *J. Catal.* **1993**, 144, 175.
54. M. Valden, X. L., D.W. Goodman, *Science* **1998**, 281, (1647).
55. Franceschetti, A.; Pennycook, S. J.; Pantelides, S. T., *Chem. Phys. Lett.* **2003**, 374, 471.
56. Sun, Q.; Jena, P.; Kim, Y. D.; Fischer, M.; Gantefor, G., *J. Chem. Phys.* **2004**, 120, (14), 6510.



57. Heiz, U.; Sanchez, A.; Abbet, S.; Schneider, W.-D., *Chem. Phys.* **2000**, 262, 189.

## CHAPTER SIX

### SUMMARY AND CONCLUSIONS

A comprehensive literature review of recent advances in Supramolecular Assembly was provided in Chapter 1. Special attentions were given to transition metal-directed assembly and polyoxometalate based superamolecular assemblies. The latter was further addressed as wheel/sphere shaped assembly and layer by layer (LbL) assembly.

In Chapter 2, a series of Ruthenium (II) based molecular squares with a general formula  $\{[\text{RuCl}_2(\text{dppb})](\mu\text{-N-N})\}_n$  were synthesized, where  $\mu\text{-N-N}$  ligands include pyrazine(PZ), 4,4'-bipyridine(BP), 4,4'-Azodipyridine(AZP), 4,4'-(1,3-butadiyne-1,4-diyl)bis-Pyridine(DPB) and 3,6-di-4-pyridinyl-1,2,4,5-Tetrazine(dipyTz). The AZP, DPB, dipyTz complexes have not been reported before and their physical and chemical properties are of our interest in this study. These molecular squares have been characterized using UV-Vis, Raman,  $^1\text{H-NMR}$ ,  $^{31}\text{P}$  NMR, Diffusion NMR, and Electrochemistry including Cyclic Voltammetry, Controlled Potential Electrolysis and Potential Step. Interestingly, for DPB and dipyTz complex, square-triangle equilibrium was observed in the solution phase. The equilibrium exhibit concentration dependence suggested by  $^1\text{H-NMR}$  spectra. For DPB complex, the triangle species dominate at low concentration and square species dominate at high concentration; in contrast, dipyTz

complex has triangle species as abundant species in the whole range of concentration studied. This is the first time equilibrium behavior was reported for Ruthenium based assemblies.

In Chapter 3, membrane separation involving the above characterized molecular squares has been explored. Permeation tests in both solution phase and gas phase were carried out, and preliminary results were obtained. In the solution phase, thin films with PZ, BP and AZP complex were prepared by drop coating molecular squares onto a glassy carbon working electrode, and then their cyclic voltammygrams were recorded in redox probes ( $\text{Ru}(\text{NH}_3)_6^{3+}$ ,  $\text{Co}(\text{bpy})_3^{3+}$ ) solution. In the gas phase, thin films of PZ, BP complex supported on Alumina were tested with a home built glass cell that coupled to a Gas Chromatography analyzer. The study shows that the BP complex with smaller porosities can give rise to better separations. In addition to size effect, affinity also takes part in the separation process.

In Chapter 4, POM-encapsulated hydroquinone system was prepared by coordinating 2,5-dihydroxy-1,4-benzenediacetic acid to the cyclic neutral oxothio compound  $\text{W}_{16}\text{S}_{16}\text{O}_{16}(\text{OH})_{16}$ . The complex was formed by acido-basic condensation of eight  $[\text{W}_2\text{S}_2\text{O}_2]^{2+}$  building block while 2,5-dihydroxy-1,4-benzenediacetic acid acted as a template. Crystals were grown through slow evaporation and single crystal XRD shows two 2,5-dihydroxy-1,4-benzenediacetic acid molecules were encapsulated into the cavity of  $\text{W}_{16}\text{S}_{16}\text{O}_{16}(\text{OH})_{16}$ . Due to the steric constraints induced by the presence of 2,5-dihydroxy-1,4-benzenediacetic acid in the cavity, four tungsten atoms show pyramidal geometry. Besides, the NMR spectrum of the complex in  $\text{D}_2\text{O}$  shows peak shifts in comparison with free 2,5-dihydroxy-1,4-benzenediacetic acid further indicating the

coordination of hydroquinone with POMs. The electrochemistry of the complex shows one reversible redox couple in the range of 0-400mV. Further scan to the positive direction will cause the decomposition of the Complex. Interesting, the positive shift of the potential attributed to the combination of hydroquinone and hydroquinone-POM with successive further positive scan suggests a potential redox-dependant behavior.

In Chapter 5, PDDA stabilized Au nanoparticles and polyoxometalates (Cobalt monosubstituted wells Dawson) were used to form hybrid thin films on glassy carbon substrates using layer-by-layer (LbL) assembly. The modified electrodes were employed as cathodes for the oxygen reduction reaction (ORR) and showed good catalytic ability towards oxygen reduction with a Specific Activity (SA) as high as 7.33 mA/cm<sup>2</sup>. The improved SA was attributed to both the special nature of gold nanoparticles and cobalt substituted wells-dawson compound which can efficiently break the absorbed O<sub>2</sub> bond during the oxygen reduction process.

In summary, we have synthesized three types of supramolecular assemblies which are fully characterized with UV-Vis, NMR, Raman and Electrochemistry. These assemblies showed promising applications in membrane separation, sensing and oxygen reduction catalysis. The ease to synthesis, flexible to design and wide applications makes them continually to be the current research interest. Also as revealed in this study, some points are not completely understood such as the square-triangle equilibrium for transition metal directed assembly and whether all the layers or just the outmost layer play the role during catalysis process in LbL assembly. New techniques and new strategies are required for the further study.